

Unraveling the Potential of Graphene for Hydrogen Storage: Insights from Molecular Dynamics Simulations

Ph.D. Thesis

By

**NITIN LUHADIYA
(Roll Number: 1901103004)**



**DISCIPLINE OF MECHANICAL ENGINEERING
INDIAN INSTITUTE OF TECHNOLOGY INDORE**

March 2024

Unraveling the Potential of Graphene for Hydrogen Storage: Insights from Molecular Dynamics Simulations

A THESIS

*Submitted in partial fulfillment of the
requirements for the award of the degree
of*

DOCTOR OF PHILOSOPHY

by

NITIN LUHADIYA

(Roll Number: 1901103004)



**DISCIPLINE OF MECHANICAL ENGINEERING
INDIAN INSTITUTE OF TECHNOLOGY INDORE**

March 2024



INDIAN INSTITUTE OF TECHNOLOGY INDORE

CANDIDATE'S DECLARATION

I hereby certify that the work which is being presented in the thesis entitled **Unraveling the Potential of Graphene for Hydrogen Storage: Insights from Molecular Dynamics Simulations** in the partial fulfillment of the requirements for the award of the degree of **DOCTOR OF PHILOSOPHY** and submitted in the **Department of Mechanical Engineering, Indian Institute of Technology Indore**, is an authentic record of my own work carried out during the time period from July 2019 to March 2024 under the supervision of **Dr. Shailesh I. Kundalwal, Associate Professor, Indian Institute of Technology Indore, and Prof. S.K. Sahu, Professor, Indian Institute of Technology Indore.**

The matter presented in this thesis has not been submitted by me for the award of any other degree of this or any other institute.

Signature of the student with date

Mar 22, 2024

(NITIN LUHADIYA)

This is to certify that the above statement made by the candidate is correct to the best of my/our knowledge.

Signature of Thesis Supervisor #1 with date

Mar 22, 2024

(Dr. SHAILESH I. KUNDALWAL)

Signature of Thesis Supervisor #2 with date

March 22, 2024

(Prof. S.K. SAHU)

Nitin Luhadiya has successfully given his Ph.D. Oral Examination held on _____

Signature of Thesis Supervisor #1 with date

(Dr. SHAILESH I. KUNDALWAL)

Signature of Thesis Supervisor #2 with date

(Prof. S.K. SAHU)

Acknowledgements

It is a great pleasure for me to acknowledge all the people who have helped and supported me to complete this Thesis. First and foremost, I would like to express my sincere gratitude to my advisor **Dr. Shailesh Ishwarlal Kundalwal** for the continuous support of my Ph.D. study and related research, for his patience, motivation, academic support and immense knowledge. His guidance helped me in all the time of research and writing this thesis. I could not have imagined having a better advisor and mentor for my Ph.D. study. This has not only enriched me academically but has also nourished my inner self and changed my perspective and attitude a lot. It is through this association with him that I have been able to acquire, develop and sharpen the skills and the scientific methodologies which are invaluable for good independent research. His immense knowledge, guidance, observations and comments helped me a lot to establish the overall direction of the research and to move forward with investigation in depth. For all this, I will remain indebted and grateful to him for my entire life.

Besides my advisor, I would like to express my gratitude towards my co-supervisor **Prof. Santosh Kumar Sahu**, Department of Mechanical Engineering, and PSPC members **Prof. Devendra Deshmukh**, Department of Mechanical Engineering and **Prof. Manish Kumar Goyal**, Department of Civil Engineering, Indian Institute of Technology Indore for their insightful comments and encouragement, but also for the hard question which incentivised me to widen my research from various perspectives. I am grateful to **Head, DPGC Convener**, all the faculty members and staff of Department of Mechanical Engineering, **IIT Indore** for providing encouraging environment to carry out research effectively.

I would like to acknowledge **Prof. Suhas Joshi, Director, IIT Indore** for providing a conducive environment for research and opportunity to explore my research capabilities at IIT Indore. I am also thankful to **The Dean of Academic Affairs, The Dean of Research and Development and The Dean of Student Affairs, IIT Indore**.

A sincere thanks also goes to **Dr. Vijay Choyal, Dr. Vijay Kumar Choyal, Dr. Dharmendra Panjariya, and Dr. Bhupendra Singh More** who always encouraged my research work during my M. Tech and Ph.D. study.

I take this opportunity to thank each and every one of my friends. There have been so many of you – it is impossible to name all of you. I am indebted to my seniors, lab mates and colleague researchers especially **Dr. Madhur Gupta, Dr. Anas Ullah Khan, Dr. Subhash Nevhal, and Mr. Saurabh Mishra** for their cooperation and stay so as to make my PhD journey joyful and with whom I have spent so much time discussing both technical and non-technical stuff.

It is impossible to imagine a life without family. I would like to acknowledge my Father **Mr. Sunil Luhadiya** and Mother **Mrs. Kavita Luhadiya** for their continuous inspiration during the entire period of my stay at IIT Indore and for appreciating my work with great patience and understanding. I salute you both for the selfless love, care, pain and sacrifice you did to shape my life. Although you hardly understood what I researched on, you were willing to support any decision I made. It gives me immense pleasure and satisfaction to express my respect and gratitude to my younger brother **Mr. Ujjawal Luhadiya** for their constant inspiration and unconditional moral support. Also, a special thanks to my uncles and all in-laws for their continuous inspiration. Last but not the least, I would like to thank my wife **Mrs. Isha Luhadiya** for her love, motivations, valuable prayers and support which provided me strength and for coming as good luck in my life during my PhD journey.

Finally, I am thankful to all who directly or indirectly contributed, helped and supported me.

-Nitin Luhadiya

Indian Institute of Technology Indore

Date: **22-03-2024**

Dedicated To

My Beloved Family

“Nanotechnology has given us the tools to play with the ultimate toy box of nature – atoms and molecules. The possibilities to create new things appear limitless.”

(Prof. Kim Eric Drexler)

Abstract

This thesis investigates the enhancement of hydrogen storage capabilities of graphene and its derivatives through various modifications, utilizing molecular dynamics simulations (MDS) to analyze the effects of temperature, pressure, strain, vacancy defects, and atomic-level modifications on hydrogen adsorption and desorption behaviors. The research introduces a novel method for potential energy distribution (PED) estimation to explore the gravimetric density of hydrogen adsorption, providing a comprehensive simulation framework for studying these phenomena under diverse conditions. The initial part of the study focuses on the hydrogen adsorption behavior on monolayer graphene, revealing that low temperatures and high pressures are optimal for achieving high gravimetric densities. The introduction of strain and vacancy defects in graphene nanosheets (GNS) shows significant increases in hydrogen storage capacity, with specific defects and strains identified as particularly effective for enhancing adsorption. Furthermore, the thesis delves into the potential of titanium-decorated polycrystalline graphene (Ti-PGs) and examines the influence of grain boundaries and Ti atom concentration, finding that these factors substantially augment hydrogen adsorption. Additionally, nitrogen doping and titanium adatom implantation on graphene sheets with vacancy defects (D-G) are explored as methods to further increase hydrogen storage efficiency. The study demonstrates that these atomic-level modifications can lead to notable improvements in hydrogen storage capacities, with certain configurations achieving significantly higher adsorption rates and capacities compared to pristine graphene sheets. Overall, this research provides valuable insights into the mechanisms of hydrogen adsorption by graphene and its derivatives, highlighting the potential of structural and compositional modifications for optimizing graphene-based materials for efficient and reversible hydrogen storage. The findings contribute to the development of novel materials and methodologies for hydrogen storage, addressing one of the critical challenges in the utilization of hydrogen as a sustainable and clean energy carrier.

Keywords: Atomistic modeling; Graphene defects; Graphene doping; Hydrogen storage; Molecular dynamics simulation; Polycrystalline graphene.

Table of contents

List of figures	v-vii
List of tables	viii
List of symbols	ix-x
List of abbreviations	xi
1. Introduction and literature review	1-19
1.1 Hydrogen storage: challenges and targets	2
1.2 Nanoengineering and nanotechnology	3
1.3 Hydrogen storage: methods	4
1.4 Graphene	6
1.5 Hydrogen adsorption capacity of pristine graphene sheets	8
1.6 Hydrogen adsorption capacity of functionalized graphene sheets	10
1.7 Scope and objectives of the present research	16
1.8 Organization of the thesis	18
2. Classical molecular dynamics	20-37
2.1 Atomistic modelling	20
2.2 Molecular dynamics (MD) simulations	21
2.2.1 Introduction	21
2.2.2 Equations of motion	22
2.2.3 Integration algorithms	23
2.2.4 Temperature control	25
2.2.5 Pressure control	27
2.2.6 Statistical ensembles	28
2.2.7 Potential fields	29
2.2.8 Tersoff potential force field	31
2.2.9 Molecular dynamics parameters	33
2.2.10 MD simulator	35
3. Simulation framework and adsorption behavior analysis of GNS	38-55
3.1 Introduction	38
3.2 MD modeling of GNS	40

3.3	Adsorption isotherms	44
3.3.1	Langmuir isotherm	44
3.3.2	Freundlich isotherm	44
3.3.3	Sips (Langmuir–Freundlich) isotherm	44
3.3.4	Toth isotherm	45
3.3.5	Fritz–Schlunder isotherm	45
3.4	Error functions	45
3.4.1	The sum of the squares of the errors	46
3.4.2	The hybrid fractional error function	46
3.4.3	The average relative error function	46
3.4.4	The marquardt’s percent standard deviation	47
3.4.5	The sum of the absolute errors function.	47
3.5	Accuracy of the fit	47
3.6	Results and discussion	48
3.7	Conclusions	55
4.	Hydrogen storage capacity of GNS: The role of strain and vacancy defects	56-67
4.1	Introduction	56
4.2	MD modeling of defected GNS	57
4.2.1	Providing strain:	59
4.2.2	Introducing defects in GNS:	59
4.3	Results and discussions	60
4.3.1	Effect of strain on H ₂ adsorption	60
4.3.2	Effect of defects on H ₂ adsorption	61
4.4	Conclusion	67
5.	Enhanced hydrogen storage in titanium decorated polycrystalline graphene	68-84
5.1	Introduction	68
5.2	Methodology	70
5.2.1	Modeling of Ti decorated PGs	70
5.2.2	GCMC technique	73
5.2.3	Isosteric enthalpy	75
5.3	Results and discussion	75

5.4	Conclusion	83
6.	Hydrogen Storage in Graphene: Nitrogen Doping and Titanium Implantation	85-99
6.1	Introduction	85
6.2	Methodology	87
6.2.1	Modeling of atomic structures	87
6.2.2	Interatomic potentials	88
6.2.3	Titanium implantation on N-/D-Gs using MD simulations	89
6.2.4	MD simulation of hydrogen adsorption on functionalized Ti-/N-/D-G sheets	90
6.3	Results and Discussion	91
6.3.1	Effect of Ti adatoms on hydrogen uptake of D-G sheets	92
6.3.2	Effect of Ti adatoms on hydrogen uptake of N-D-G sheets	95
6.4	Conclusions	99
7.	Conclusions and future scope	100-103
7.1	Major Conclusions	100
7.2	Limitations of the Study	102
7.3	Scope for future work	103
	References	104-119
	List of publications and patents	120-121
	Curriculum Vitae	122-123

List of figures

Fig. no.	Caption of figure	Page no.
1.1	The comparison of size of nanoscale objects.	4
1.2	Various hydrogen storage techniques.	4
1.3	Structure of pristine graphene sheets.	7
	A schematic description of atomistic modelling strategies with representative length and time scales for computational simulations.	
2.1	Some typical nanostructures such as BN nanotube, nanosheet, and nanocomposite are shown as illustrative examples for different length and time scales.	21
2.2	Variation in the positions and velocities of atoms with the time.	24
2.3	Graphical representation of the microcanonical (NVE) ensemble, the canonical (NVT) ensemble and the isothermal-isobaric (NPT) ensemble (Gale et al., 2012).	29
2.4	Interatomic relative motions in molecular mechanics.	30
2.5	Graphical representation of the PBCs of the middlebox. The arrows indicate the directions of the velocities of atoms. The atoms in the middlebox can interact with atoms in the neighbouring boxes without having any boundary effects.	34
2.6	The overview of LAMMPS input script	35
3.1	System configuration of graphene sheet and H ₂ molecules: (a) Initial system configuration with relaxed graphene sheet, (b) system at simulation time 1 ns, and (c) adsorbed H ₂ molecules around graphene.	41
3.2	(a) Time evolution of the system at 77 K and 1 MPa, respectively, and (b) variation of potential energy of the system and adsorption of H ₂ molecules with the time.	49
3.3	(a) Potential Energy Distribution (PED) of hydrogen molecules, and (b) front and top views of H ₂ molecules at 77 K and 1 MPa.	50
3.4	(a) Variation of adsorption energy with pressure, and (b) adsorption isotherms at 77 K, 100 K, 200 K, and 300 K.	51
3.5	(a) Non-linear fitting, and (b) error residuals of the isotherm from MDS at 77 K.	53
4.1	Different point defects	59
4.2	Variation of wt.% of hydrogen adsorption on graphene with strain at 77 K and 10 bar.	61

4.3	(a) Adsorption isotherm and (b) average adsorption energy vs pressure for pristine graphene.	61
4.4	Comparison of MV-GNS hydrogen adsorption isotherms with P-GNS at 77 K and 300 K.	62
4.5	Comparison of (a) SW-GNS (b) 5-8-5 DV-GNS hydrogen adsorption isotherms with P-GNS 77 K and 300 K.	63
4.6	Comparison of (a) 555-777 DV-GNS (b) 5555-6-7777 DV-GNS hydrogen adsorption isotherms with P-GNS 77 K and 300 K.	64
4.7	Variation of D-GNS hydrogen adsorption isotherms at (a) 77 K and (b) 300 K.	65
4.8	Strain vs stress curve of D-GNS at 300 K.	66
5.1	(a) Polycrystalline graphene sheet [red lines indicate the GBs], and (b) polycrystalline graphene sheet decorated with randomly distributed titanium atoms. [Yellow Ti atoms; and gray C atoms].	70
5.2	System configuration of titanium-decorated polycrystalline graphene sheets: (a) isometric view and (b) side view. [Blue hydrogen atoms; yellow Ti atoms; and gray C atoms].	72
5.3	Flow diagram of MC simulations.	74
5.4	(a) Uniaxial tensile test of PGs for different grain sizes and (b) hydrogen adsorption capacity of PGs with varying grain sizes at different temperatures and pressures.	76
5.5	The stress–strain curves of titanium-decorated PGs (1 nm grain size) for different titanium concentrations.	77
5.6	Fracture of (a) polycrystalline graphene and (b) Ti-decorated polycrystalline graphene. Color coding shows the intensity of the stress. [Magenta Ti atoms].	78
5.7	Hydrogen adsorption and desorption capacity of Ti-PGs with 1 nm grain size at varying titanium concentrations at various pressures: (a) 77 K, and (b) 300 K temperatures.	79
5.8	Hydrogen adsorption isotherms of Ti-PGs with 1% Ti concentration at (a) low temperatures (77 K and 97 K), and (b) high temperatures (280 K and 300 K). MDS data points are fitted with Toth isotherm model.	81
5.9	Plot of logarithmic pressure against wt.% obtained from the isotherms of Ti-PGs at (a) low temperatures (77 K and 97 K) and (b) high temperatures (280 K and 300 K). Dashed lines are isosteric lines, and square markers are isosteric logarithmic pressures at different wt.%	81
5.10	Isosteric enthalpy of adsorption of H ₂ for Ti-PGs (a) 77 K and, (b) 300 K.	82

6.1	(a) Graphene sheet with various types of common defects encountered during synthesis, (b) Graphene sheet containing defects doped with pyridinic nitrogen atoms; black lines are graphene lattice, defects are outlined in magenta, N atoms are in blue	87
6.2	(a) Relaxed graphene sheet containing MV defects with titanium adatoms; (b) system configuration with adsorbed hydrogen molecules surrounding Ti-DGs at 1 ns simulation time. The black lines are graphene lattice, N atoms are in blue, Ti atoms are in yellow, and H atoms are in grey.	90
6.3	Variation in adsorption capacity of Ti-MV-G with increasing Ti concentrations at various pressures and temperatures, (a) 77 K and (b) 300 K.	93
6.4	Variation in adsorption capacity of Ti-DV(III)-G with increasing Ti concentrations at various pressures and temperatures, (a) 77 K and (b) 300 K.	95
6.5	Variation in adsorption capacity of Ti-N-MV-G with increasing Ti concentrations at various pressures and temperatures, (a) 77 K and (b) 300 K.	96
6.6	Variation in adsorption capacity of Ti-N-DV(III)-G with increasing Ti concentrations at various pressures and temperatures, (a) 77 K and (b) 300 K.	97

List of Tables

Table no.	Caption of table	Page no.
2.1	Parameters used in Tersoff potentials for B-B, N-N, B-N, C-C, C-N and C-B interactions.	33
3.1	LJ interaction parameters for carbon atoms and hydrogen molecules.	42
3.2	The influence of sheet edge length on hydrogen adsorption at 77 K and 1 MPa.	51
3.3	A comparison of the sum of normalized errors (SNE), standard error (SE) and coefficient of determination (R ²)	53
3.4	The parameters obtained from Toth isotherm models at different temperatures using the HYBRID error function	54
4.1	Comparison of critical strain and stress of pristine graphene predicted by different methods.	66
5.1	LJ interaction parameters for different atomic interactions.	71
6.1	Comparison of gravimetric density of graphene sheets containing SW, DV(I), DV(II) defects with 10.5% Ti adatom concentration.	94

List of symbols

1D	One dimensional
2D	Two dimensional
3D	Three dimensional
E	Total energy
E_i	Site energy
V_{ij}	Bond energy
r_{ij}	Distance between atom i and j
b_{ij}	Bond angle
f_R	Repulsive potential
f_A	Attractive pair potentials
f_C	Cut-off function
R and D	Model specific parameters
u_{ij}	Pairwise interaction energy between atom i and j
ε_{ij}	Well depth energy between atom i and j
σ_{ij}	The distance at which pair interaction energy goes to zero
wt. %	The gravimetric density
q	Amount of adsorbate
K	The affinity constant
q_m	The maximum adsorption capacity at a particular temperature
T	Temperature
P	Pressure
n_T	The heterogeneity factor
R^2	Correlation index
SE	Standard Error
E_a	Adsorption energy
E	Strain
l_k	Length of the sheet in at timestep k
ρ	Concentration in % (defects, dopants, decoration etc.)
σ	Average virial stress

ΔH_{ads}	The isosteric enthalpy of adsorption
P	Density (Kg/m ³)
q_i	Charge of i th atom
Θ	Angle (degree or radian)
μ	Poisson's ratio
D_i	The diameter of the i th atom
m_i	The mass of the i th atom
π	Approximately 3.1416
Σ	Summations

List of abbreviations

AFM	Atomic force microscopy
AIREBO	Adaptive intermolecular reactive empirical bond order
BNNT	Boron nitride nanotube
CNT	Carbon nanotube
CNF	Carbon nanofibers
CVD	Chemical vapor deposition
DFT	Density functional theory
DGs	Graphene sheets containing defects
DV	Double vacancy defect
EBR	Electron beam irradiation
GCMC	Grand canonical Monte Carlo
GNS	Graphene nanosheets
LAMMPS	Large-scale molecular massively parallel simulator
LJ	Lennard-Jones
MD	Molecular dynamics
MV	Mono vacancy defect
NEMS	Nanoelectromechanical systems
PE	Potential energy
PGs	Polycrystalline graphene sheets
SE	Strain energy
SSA	Specific surface area
SW	Stone Wales defect
TEM	Transmission electron microscopy
VASP	Vienna ab initio package
VMD	Visual molecular dynamics
VESTA	Visualization for electronic and structural analysis

Chapter 1

Introduction and literature review

In this chapter, a brief introduction to the graphene nanosheets (GNS) and review of literature on the adsorption properties of pristine and functionalized GNS are covered. Based on the review of literature, the scope of work for this thesis is identified, and the objectives of dissertation are presented. Organization of the chapters is delineated at the end of this chapter.

The limited supply of conventional fossil fuels cannot cope with the ever growing energy demands. More than 85% of energy consumption comes from non-renewable sources, which will be depleted in the next 50 years if their consumption continues at the current rate (BP Statistical Review of World Energy, 2018). The combustion of conventional fuels with air releasing gases like CO, CO₂, SO₂, etc. (Churchill, 1997) cause severe damage to the environment and human health. Significant efforts are being placed to reduce fossil fuel dependency and find an alternative energy source (Chahine and Bénard, 1998).

The history of fuel development shows a trend towards higher hydrogen concentrations, from coal to petroleum to natural gas. Eventually, this progression will ultimately lead to hydrogen as the clean fuel of the future. Hydrogen attracts a lot of attention due to its sustainability, high efficiency, environmental friendliness, and heating values three times greater than carbon-based fuels. It is the lightest substance in the universe; at the same time, it is one of the abundant sources of energy and has the highest energy density per unit mass (between 120 MJ/kg and 142 MJ/kg) and can provide high on-demand power (Dante et al., 2002; Kumar et al., 2012; Stalker et al., 2019). The application scope of hydrogen fuel cells (HFCs) is vast, particularly in transportation (like cars, buses, and forklift trucks) (Crabtree et al., 2004; Léon, 2008; Mazloomi and Gomes, 2012; Schlapbach, 2009; Schlapbach and Züttel, 2001) and HFC-based backup power

(Barrett, 2005; Chang, 2017; Houf et al., 2013); the space industry is widely using hydrogen as a fuel in rocket propulsion systems.

1.1 Hydrogen storage: challenges and targets

The recent interest in hydrogen as an alternative fuel has sparked a lot of research into the technological aspects of its production, storage, and distribution (Berry and Aceves, 1998). For a hydrogen economy, global issues include sustainable energy generation, storage, and consumption (Bénard and Chahine, 2001). Hydrogen production and fuel cell technologies have shown considerable promise in the hunt for non-polluting renewable energy sources. However, storing hydrogen has been regarded as the most challenging difficulty in hydrogen energy as it has an extremely low ambient temperature density. The lack of safe and efficient onboard storage and release systems problems triggered the researchers to find an efficient and economical solution (Ao et al., 2014). An ideal hydrogen storage system should be robust and reliable have high gravimetric density, fast kinetics, and reusability at room temperature (Li et al., 2003). A hydrogen storage system that is compact, portable, safe and cost-efficient could be functional for a sustainable hydrogen economy. For fuel cell vehicles to be effective, it is essential to store hydrogen at high densities. The hydrogen must be kept in a compact space without significantly increasing the vehicle's weight. For light-duty vehicles to be commercially viable, they need to have a driving range of at least 300 miles. This requires the vehicle to carry between 5 to 7 Kg of hydrogen, depending on the efficiency of future fuel cells. However, hydrogen poses a unique challenge compared to other chemical fuels due to its very weak intermolecular forces. Under normal conditions, such as a temperature of 20 °C and pressure of 1 bar, 1 kilogram of hydrogen occupies a volume of 11.9 m³. Therefore, the primary aim of research in hydrogen storage is to reduce this volume effectively while maintaining specific limits for temperature and pressure. The US Department of Energy (DOE) has set an ultimate goal for a storage system that delivers hydrogen at a gravimetric and volumetric capacity of 5.5 wt.% hydrogen and 0.050 Kg hydrogen/L, respectively (“Hydrogen Storage | Department of Energy,” 2020).

1.2 Nanoengineering and nanotechnology

Nanoscience refers to the study, manipulation and engineering of matter, particles and structures at the nanometer scale level (one billionth of a meter, $1/10^9$). The important properties of nanomaterials such as mechanical, electrical, optical and thermal are largely depend on the way molecules and atoms arranged at the nanoscale level into the larger structures. Moreover, in case of nanomaterials, atomic-level properties often change compared to the macroscale because of quantum mechanical effects (Cohen, 2001). Nanomaterials possess larger surface area compared to their parent materials at the microscale level for a given volume (Roco and Williams, 1999). The larger surface area increases the reactivity of nanomaterials and they can be used efficiently in numerous applications.

Nanotechnology is the application of nanoscience and utilization and creation of devices and materials by manipulation of the matter at the scale of nanometers or atomic/molecular scale. The generalized description of nanotechnology is given by the National Nanotechnology Initiative, and according to that, nanotechnology is the manipulation of matter with at least one dimension sized between 1 to 100 nm. Figure 1.1 depicts some sense of how this size scale relates to more familiar, everyday scales. Controlling the features of matter on the scale of nanometer has already made a significant contributions in several disciplines: engineering, physics, material science, chemistry, medicine and biology (Roco and Williams, 1999). The term “nanotechnology” was coined by Richard Feynman in 1959. The research at the nanoscale level accelerated after the discovery of scanning tunneling microscopy (STM) (Binnig et al., 1982) and atomic force microscopy (AFM) (Binnig et al., 1986). The discovery of STM and AFM allowed researchers to study and observe individual atoms and manipulate them. A modification at the nanoscale level eventually allows us to design custom-made materials and products with enhanced properties, including nanoelectronics, smart medicines and sensors, and even interfaces between electronics and biological systems can be tailored (Roco and Williams, 1999).

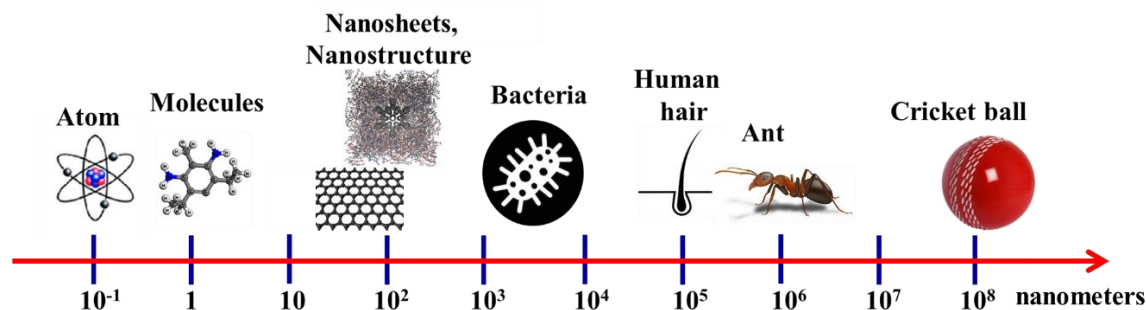


Figure 1.1 The comparison of size of nanoscale objects.(V. Choyal)

The proliferation of nanoscale technology and science has led to the discovery of several interesting nanomaterials. For instance, the ground-breaking discovery of two-dimensional (2D) atomic-thick graphene layer was carried out by Novoselov and Geim in 2004 (A.K.Geim et al., 2007). Its extraordinary mechanical (Huang et al., 2006; Ni et al., 2010; Dewapriya et al., 2014; Javvaji et al., 2018), thermal (Ng et al., 2012; Zhang et al., 2017), and electrical (S I Kundalwal et al., 2017) properties encouraged to study it further for hydrogen storage applications.

1.3 Hydrogen storage: methods

There are two general methods for hydrogen storage: (i) physical storage, and (ii) material storage (Ciancia et al., 1996; Moradi and Groth, 2019; Rivard et al., 2019) as depicted in Figure 1.2.

Physical		Materials-Based	
Compressed Hydrogen (350, 700 bar)	Liquified Hydrogen	Metal Hydrides	
Cryo-Compressed Hydrogen	Slush Hydrogen	Liquid Organic Hydrogen Carriers	Sorbents (MOFs, Zeolites, Carbon Nanostructures)

Figure 1.2 Various hydrogen storage techniques.

Physical Hydrogen Storage:

- *Compressed Hydrogen Gas*: The most common method of hydrogen storage is as a compressed gas in high-pressure tanks. Hydrogen is typically stored at pressures

ranging from 350 to 700 bar (5,000 to 10,000 psi). These tanks are designed to be lightweight and strong, often made from advanced composite materials. The main challenge is the high pressure required, which demands robust tank designs and increases costs.

- *Liquefied Hydrogen:* Hydrogen can be stored as a liquid in cryogenic tanks at temperatures below -252.87°C (-423.17°F). Liquid hydrogen storage has a higher energy density by volume than compressed gas, making it a favorable option for some applications. However, the extremely low temperatures required for liquefaction are energy-intensive and require sophisticated insulation systems to minimize boil-off.

Material-Based Hydrogen Storage:

- *Metal Hydrides:* These are materials that can absorb hydrogen to form metal hydrides. They offer safe and compact storage, with lower risks of leakage. The hydrogen is released from the hydride by heating the material, which can be integrated into the fuel cell system. However, the weight of these systems and the energy required to release hydrogen are current challenges.
- *Chemical Hydrogen Storage:* This method involves hydrogen being stored in chemical compounds, which release hydrogen upon certain chemical reactions. Examples include ammonia and liquid organic hydrogen carriers (LOHCs). These methods often offer high hydrogen storage densities but require complex chemical processes for hydrogen release and capture.
- *Carbon-based Materials:* Research is ongoing into using carbon-based materials like carbon nanotubes and graphene for hydrogen storage. These materials potentially offer high storage capacities at lower pressures than compressed gas storage but are still in the experimental stage and face challenges in terms of cost and scalability.

Hydrogen storage systems are characterized by high volumetric density, which can be achieved by either compressing the gas at high pressures of up to 700 bar or by liquifying the hydrogen at temperatures of 20–25 K. Whereas, in material-based storage i.e. solid-state storage, the hydrogen molecules are bonded to the material by physical and chemical bonds (Jorgensen, 2011). To improve the hydrogen storage capacity lightweight

and porous materials with a high specific surface area are preferred. These materials adsorb hydrogen through different mechanisms, either by physical bonds (physisorption) or by chemical bonds (chemisorption). Adsorption through chemisorption is undesirable for hydrogen storage as it leads to chemical dissociation of the hydrogen molecule and firm binding of hydrogen, which cannot be released during the desorption process. Metal hydrides and complex hydrides store hydrogen with high gravimetric efficiency at ambient temperatures, but due to the strong binding of hydrogen, they have low reversibility, slow reaction kinetics, and a high dehydrogenation temperature (Boateng and Chen, 2020; Rusman and Dahari, 2016). Binding energy higher than 0.6 eV/H₂ leads to chemical dissociation of the hydrogen molecule, which reduces the amount of usable hydrogen. Physical storage and chemisorption have several disadvantages, like energy losses in refrigeration, boiloff effect, and required high thermal energy for desorption (Chae et al., 2004). Physisorption is the result of weak van der Waals force of attractions due to fluctuating dipole moments on the interacting adsorbate and adsorbent. For transportation purposes, hydrogen storage by material-based physisorption is an attractive method as there is no chemical dissociation of molecules and no fuel contamination (Barghi et al., 2014). On the other hand, it provides faster kinetics for discharging and refueling than reactive hydrogen storage. (Bastos-Neto et al., 2012). For high gravimetric density and fast kinetics, the non-dissociative binding energy ranges between 0.1 and 0.6 eV/H₂ (Chan et al., 2017). In physisorption, the hydrogen gas in molecular form adsorbs on the surface via van der Waals forces of attraction that arises due to mutually induced dipole moments in the substrate and hydrogen molecules. Once the H₂ gas molecules cover the adsorbent's entire surface, the adsorption saturates (Ströbel et al., 2006a). Physisorption is genuinely reversible, safe, portable, and more viable for solid state hydrogen storage (Iñiguez, 2008). When it comes to achieving the goal of a large amount of hydrogen storage, using nanostructures with a high specific area is a logical option.

1.4 Graphene

Graphene (Novoselov et al., 2004) is a two-dimensional material, which is essentially a single layer of graphite, and represents the basic building block for graphitic materials of all other dimensionalities. As depicted in Figure 1.3, It consists of carbon atoms arranged in a planar hexagonal lattice with a bond length of approximately 1.42

angstroms (\AA). The carbon atoms in graphene are with one 2s orbital and two 2p orbitals that hybridize to form three sp^2 orbitals. These three sp^2 orbitals lie in the plane of the graphene sheet and overlap with the sp^2 orbitals of neighboring carbon atoms to form σ -bonds, which give the lattice its structural integrity and planarity. The remaining 2p orbital, which is oriented perpendicular to the plane, forms a π -bond by overlapping with the 2p orbitals of adjacent atoms. This π -bond is delocalized across the entire sheet of graphene, allowing for the free movement of electrons and giving graphene its extraordinary electrical conductivity (Kan et al., 2011).

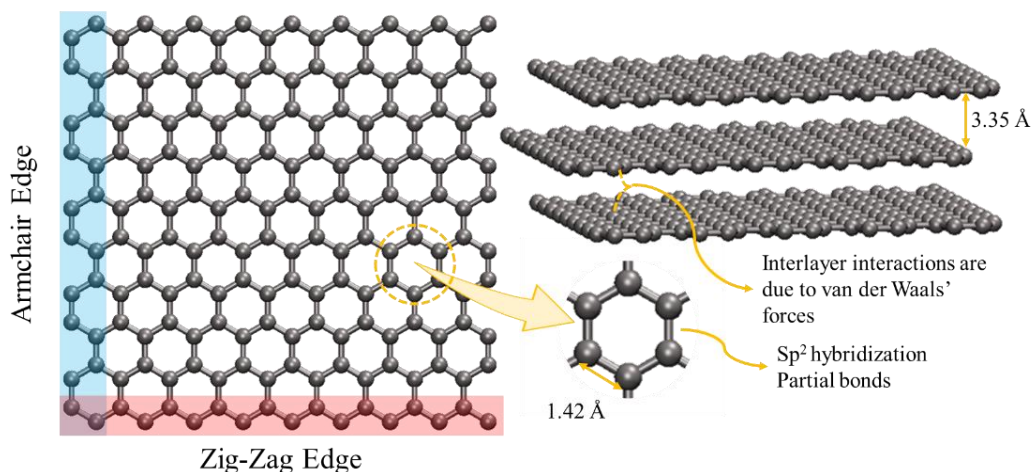


Figure 1.3 Structure of pristine graphene sheets.

In multilayer graphene sheets, the individual graphene layers are held together by weak van der Waals forces, which are intermolecular attractions rather than strong covalent bonds like those within the individual graphene layers (Niilisk et al., 2016; Yelgel, 2016). These interactions are significant because they allow the layers to maintain a relative distance of about 3.35 \AA apart, enabling them to slide over each other, contributing to graphite's lubricating properties. The typical stacking pattern of multilayer graphene follows the AB (Bernal) stacking order, where half of the carbon atoms in one layer lie above the center of the hexagons in the adjacent layer, while the other half lie above empty spaces. This stacking influences the electronic properties of graphite, making it distinct from the properties of a single layer of graphene (Castro et al., 2008). Graphene edges can be of two types: armchair and zigzag, referring to the patterns that the edges make. These edge types are named based on their resemblance to the shape of a zigzag or the armrests

of a chair. These edge configurations can have significant effects on the properties of graphene nanoribbons, with zigzag edges generally displaying metallic behavior due to the presence of localized edge states, whereas armchair edges can be either metallic or semiconducting depending on their width (Castro Neto et al., 2009; Kim et al., 2018). The unique combination of these structural features— sp^2 hybridization, short bond lengths, delocalized electrons, and specific edge geometries—endows graphene with high electrical conductivity, excellent mechanical strength (Alian et al., 2017a; Lee et al., 2008a), thermal stability (Balandin et al., 2008), and possesses a high specific surface area (SSA) of $\sim 2630 \text{ m}^2\text{g}^{-1}$ (Zhu et al., 2010). Graphene is also impermeable to most gases and liquids, which makes it an excellent barrier material. In addition to these remarkable properties, graphene has good reversibility, faster adsorption, and desorption kinetics (Patchkovskii et al., 2005).

The applications of graphene are vast and diverse, spanning multiple industries; including biomedical technology, nanocomposites and nanocoatings (Kumar et al., 2020; Kundalwal et al., 2014; S. I. Kundalwal and Ray, 2014), energy storage and use in batteries, membranes, and sensors (Choi et al., 2010; Sofo et al., 2007), gas barrier (Cui et al., 2016a), and nanoelectromechanical systems (S.I. Kundalwal et al., 2017). Graphene is a promising option for the hydrogen storage application because it has large surface area, excellent thermal stability, high mechanical strength (Kundalwal, 2018; Kundalwal and Ray, 2013), and the ability to readily accept functional groups (Peigney et al., 2001; Ströbel et al., 2006b). In contrast to carbon nanotubes (Kundalwal et al., 2015; Shailesh I. Kundalwal and Ray, 2014), graphene's two surfaces may be actively used to store hydrogen (Ataca et al., 2008), but pristine monolayer graphene has low binding energy, resulting in a low gravimetric density (Ma et al., 2009a).

1.5 Hydrogen adsorption capacity of pristine graphene sheets

For solid-state hydrogen storage, SSA plays a vital role in achieving high gravimetric density for hydrogen storage (Klechikov et al., 2015; Ma et al., 2009a). Several experimental investigations and simulation studies based on density functional theory (DFT) and grand canonical Monte Carlo (GCMC) simulations have been reported for hydrogen storage on graphene sheets (Jain and Kandasubramanian, 2020; Mohan et al., 2019; Nagar et al., 2017a; Pyle et al., 2016; Shevlin and Guo, 2007; Shiraz and Tavakoli,

2017). Wang and Johnson (Wang and Johnson, 1999) performed GCMC simulations on graphitic nanofibers and hydrogen atoms in an attempt to explain the solid-fluid behavior at the nanoscale level as reported by Chambers et al. (Chambers et al., 1998). They concluded that no realistic potential could account for the high hydrogen adsorption reported by Chambers et al. (Chambers et al., 1998). The studies of Jhi (Jhi, 2007) and Torres et al. (Zyzlila Figueroa-Torres et al., 2007) on chemically activated nanostructured carbon to investigate hydrogen storage reveal that hydrogen sorption can be controlled by modifying the structure and chemistry of pores. They reported high adsorption energy of about 0.301 eV and a gravimetric density of 2.7% for nanostructured activated carbon. Ma et al. (Ma et al., 2009a) measured 0.4 wt% and <0.2 wt% hydrogen uptakes of graphene at cryogenic and room temperature, respectively, with a BET surface area of 156 m²g⁻¹. Their investigations suggest that low SSA is responsible for the small gravimetric uptake. Various carbon-based nanomaterials are investigated for the physisorption of hydrogen, and a lot of work has been done so far. Lijie Ci et al. experimentally found that the annealed CNT at the temperature range of 1700-2200 °C can store the hydrogen up to 3.98 wt% (Ci et al., 2002). M. Hirscher and B. Panella experimentally found that the carbon nanostructure has a high SSA and can store hydrogen up to 4.5 wt% at 77K (Hirscher and Panella, 2005). Hangkyo jin et al. experimentally investigate the microporous activated carbons with an SSA of 2800 m²/g and get the maximum hydrogen adsorption of 1 wt% at room temperature (Jin et al., 2007). Subsequently, S.F. Braga et al. studied the carbon nanoscrolls for hydrogen adsorption using the atomistic molecular dynamics simulations. They revealed that at a lower temperature of 77 K, hydrogen molecules are adsorbed, and on increasing the temperature to 300 K, desorption occurs (Braga et al., 2007). M. Armandi et al. experimentally investigated the hydrogen adsorption at porous graphene at different temperatures with maximum uptake of 2 wt% of hydrogen, and pores play a major role in physisorption (Armandi et al., 2008).

Pristine graphene sheets even with a very high SSA cannot bind sufficient hydrogen on their surface at ambient temperature due to low binding energy (Heine et al., 2004; Okamoto and Miyamoto, 2001; Tozzini and Pellegrini, 2011). Therefore, many theoretical and experimental studies have focused on increasing the hydrogen storage capacity of graphene. One of the most widely used methods is the functionalization of the surface of

graphene, which leads to the tailoring of characteristics like the surface area, chemical reactivity, porosity, and interlayer spacing to enhance the adsorption capacity (Gangu et al., 2019; Jain and Kandasubramanian, 2020; Shiraz and Tavakoli, 2017; Szczyński et al., 2017). To improve the adsorption capacity, graphene have been functionalized with a range of metals, including alkali, platinum, and light transition metals (TM) (Chen et al., 2008; Durgun et al., 2006; P. and Ramaprabhu, 2014; Sun et al., 2006). Various chemical reactions can also be used to tune graphene properties and their interlayer spacing (Prabhu et al., 2020), thus enhancing the adsorption properties.

1.6 Hydrogen adsorption capacity of functionalized graphene sheets

López-Corral et al. (López-Corral et al., 2010a) computationally observed hydrogen adsorption on palladium (Pd) decorated graphene sheets using the tight-binding model and reported a strong C-Pd and Pd-H bonds, which promote dissociation of hydrogen molecules and bonding between atomic hydrogen and carbon surface. Huang et al. (C. C. Huang et al., 2011) experimentally investigated graphene samples decorated with Pd and platinum (Pt) for hydrogen storage at 303K temperature and up to a 5.7 MPa pressure. They concluded that the decoration of Pd or Pt metals doubles the adsorption capacity and supports the existence of spillover effect. Recently, a review article (Nagar et al., 2017a) reports the hydrogen storage capabilities of chemically altered graphene composites and discusses the promising techniques to control the binding energy of H₂ molecules like surface chemical modifications and metal catalyst dispersion. They concluded that structural and chemical modifications might introduce new materials that may elevate the current storage capabilities. Shiraz and Tavakoli (Shiraz and Tavakoli, 2017) reviewed the graphene-based nanomaterials for hydrogen storage. They reported that doping of graphene with alkali or transition metals shows an increase in gravimetric hydrogen density and validated this using density functional theory. (Petrushenko and Petrushenko, 2018) Their ab initio study confirmed that hydrogen favours hollow sites and revealed that graphene-like boron nitride heterostructure shows advanced adsorption behavior compared with its counterparts i.e., graphene. Feng et al. (Feng et al., 2019) studied hydrogen adsorption on carbon nanostructures like graphene, multi-walled CNT, and activated carbon with varying SSA at cryogenic temperatures. They reported that graphene sheets have high potential as a hydrogen storage media with isosteric heat of

adsorption about 4.01-5.88 KJ/mol and also revealed that adsorbent with fold structure is more beneficial than pore structure. Yong-Chae Chung et al. studied the boron substituted Li decorated graphene sheet using the density functional theory (DFT) with the *ab initio* package (VASP). Their results reveal that the boron substitution enhances the ability of lithium decorated sheets for hydrogen adsorption and gets the high hydrogen storage capacity much beyond the target value set up by the department of energy (DOE) in 2010 (Park et al., 2010a). Subsequently, Srinivasan et al. experimentally synthesized the graphene powder by the reduction of exfoliated graphite oxide and reported the hydrogen wt% 1.2 and 0.1 at 77 K and 298 K, respectively (Srinivas et al., 2010). Miao Zhou et al. studied the effect of strain on hydrogen storage capability of metal decorated graphene. Their results reveal that strain prevents the metal from clustering and increases the hydrogen uptake (Zhou et al., 2010). Kun Xue and Zhiping Xu studied the effect of biaxial strain up to 10 % using the first principle on graphene. They concluded that the structurally deformed graphene has more potential to store the hydrogen compared to pristine (Xue and Xu, 2010). Chang Ming Li et al. experimentally investigate the Ni-B doped graphene via chemical reduction method and get the maximum hydrogen storage uptake up to 2.81 wt% at 77 K and low pressure (Wang et al., 2011). Valentino R. Cooper et al. studied the hydrogen adsorption on single-layer graphene using the newly developed van der Waal density functional. They concluded that the molecular hydrogen, closer to the surface, has greater interaction with graphene (Cooper et al., 2012). Surya et al. reported that the monolayered graphene sheets become chemically active by physical modification, and the introduction of strain is a non-destructive technique. The study highlights the interplay between the induced strain and the adsorption of chemical species (Surya et al., 2012). Tanveer Hussain et al. investigated the effect of biaxial strain on the lithium doped graphene sheet with first-principles density functional theory. Their results reveal that the strain increases lithium stability and enhances the hydrogen storage capacity (Hussain et al., 2012). X.L. Dong et al. studied the hydrogen adsorption capacity of the graphene sheet generated by the arc discharge method in an atmosphere of hydrogen at lower pressure. Experimentally, their results reveal that the graphene sheet with few layers exhibits the highest capacity of electrochemical hydrogen storage and good cyclic performance (Guo et al., 2013). K. K. Chattopadhyay et al. studied the effect of different types of double

vacancy (DV) defected graphene sheets on hydrogen storage using the DFT calculations and MD Simulations. Their results reveal that the sheet is well suited for hydrogen storage compared to pristine with lower adsorption energy and has excellent stability (Sen et al., 2013a). Yong-Chae Chung et al. studied the lithium decorated defected graphene for hydrogen storage using the density functional theory. Their results reveal that the Stone-Wales (SW) defected graphene attracted more Li atoms, avoided the clustering of adatoms, and showed greater potential to store the hydrogen (Kim et al., 2014). Subsequently, Chandra Veer Singh et al. investigated the effects of different types of vacancy defects on graphene for hydrogen storage using the DFT. Their results reveal that the defected graphene sheet has lower adsorption energy and binds hydrogen with a maximum gravimetric density of 7.02% (Yadav et al., 2014a). M. Mahendran et al. studied the Li decorated double carbon vacancy defect graphene (DVG) for hydrogen storage application using the DFT calculations. Their results reveal that the decoration of lithium atoms is enhanced with defected graphene and can be useful for reversible storage applications with the 7.26 wt% much beyond the target of DOE for 2015 (Seenithurai et al., 2014a). Xiao-Bao Yang et al. investigated the biaxial strain effects on Ti decorated defected graphene with first-principle calculations. Their analysis reveals that the strain modifies the system's d level configuration, which affects the binding energy between H₂ and Ti atoms, enhancing the hydrogen storage ability (Liao et al., 2015). S. A. Meguid et al. studied the influence of grain boundaries (GBs) on mechanical properties of CNTs (a rolled form of graphene sheet) using the MD simulation and reveal that the mechanical performance of CNTs is significantly affected by the orientation of GBs, diameter, and temperature (Alian et al., 2017b). Rupali Nagar and Bhaghavathi P. Vinayan et al. reviewed the H₂ storage capabilities using chemically modified graphene-based materials and concluded that using the combining techniques of structural/surface modifications could create a pathway forward to elevate the H₂ storage capacity (Nagar et al., 2017b). Shikai Deng et al. studied the effect of strain engineering on 2D nanomaterials. They revealed that strain modifies the atomic structure, lattice vibration, chemical activity, thermal conductivity, and mechanical properties (Deng et al., 2018). Prafulla K. Jha et al. studied the hydrogen adsorption on platinum decorated GQDs using the first principle study. Their results reveal that the platinum decorated GQDs efficiently store hydrogen compared to pristine, and their design

and synthesis can store hydrogen (Sharma et al., 2019). Experimental investigations have shown that large-area graphene films are polycrystalline, made up of small crystalline grains of different orientations joined by grain boundaries (GBs) (Yazyev and Chen, 2014). The experimental study performed by Huang et al. (P. Y. Huang et al., 2011) on polycrystalline graphene sheets (PGs) revealed that the presence of GBs reduces mechanical properties but does not alter electrical properties as drastically. Chen et al. (Chen et al., 2015) performed molecular dynamics simulations (MDS) to investigate the effect of the grain size, temperature, and strain rate on PGs. They showed that Young's modulus reduces by 65–82% and fracture strength reduces by 34–40% as the grain size in PGs decreases at room temperature. Alian et al. (Alian et al., 2017c) investigated the mechanical properties and fracture behavior of polycrystalline carbon nanotubes (PCNT) with a variety of GBs morphology using MDS. They first created PCNT by rolling PG and reported that a crack initiates at GBs, and there is a strength reduction by 60% due to the presence of transverse GBs in the PCNT. GBs aligned with the axis of PCNT have the least effect on the mechanical properties compared to all other orientations of GBs. Izadifar et al. (Izadifar et al., 2018, 2017) investigated the mechanical properties of PGs with nanopores doped with boron and nitrogen using MDS. They reported that (i) the ultimate failure strain of PGs increases with decreasing grain size, (ii) the doping of boron or nitrogen reduces the tensile strength of PGs, and (iii) nitrogen doping has a more severe effect compared to boron doping. Guo et al. (Guo et al., 2018) experimentally investigated the adsorption behavior of hydrogen at the interface of PGs and revealed that open edges and domain boundaries provide more active sites for adsorption and lower resistance for charge transfer. Also, the nanoscale features of nanostructured graphene provide excellent adhesion of hydrogen on the PGs. Bhattacharya et al. (Bhattacharya et al., 2009) decorated graphene, h-BN, and BC₄N with titanium (Ti) atoms for high-capacity hydrogen storage using first-principles calculations. They reported a stable high adsorption capacity of hydrogen at room temperature, and that desorption occurs at a temperature of 700–800 K for graphene and h-BN sheets, but desorption for BC₄N occurs at 500–600 K. Park et al. (Park et al., 2010b) doped boron-substituted graphene sheets with lithium atoms to investigate the hydrogen adsorption capacity and reported a high adsorption capacity of 13.2 wt.% without any clustering of adatoms. An ab initio study performed by Wang et al.

(Wang et al., 2013) on boron-substituted graphene uniformly decorated with sodium atoms showed a hydrogen storage capacity of 11.7 wt.% at 300 K. Lee et al. (Lee et al., 2013) doped nitrogen-decorated graphene with lithium for geometric stability and enhancement of hydrogen capacity using density functional theory (DFT) calculations. They observed cluster-free decoration of lithium atoms on nitrogen-doped graphene layers and found binding energy of hydrogen molecules in the range of 0.12–0.20 eV/H₂. The hydrogen adsorption capacity of Ti-doped graphyne under different external electric fields was investigated by Zhang et al. (Zhang et al., 2014) using first principle calculations. They found that the interaction between Ti and H₂ molecules increases with the applied electric field. They also reported the adsorption of four hydrogen molecules on Ti-doped graphyne, and all are stored in molecular form. A DFT study performed by Lebon et al. (Lebon et al., 2015a) on graphene nanoribbons doped with Ti atoms showed non-dissociative adsorption of the hydrogen molecule. They reported that each doped Ti atom can adsorb up to four hydrogen molecules, showing an adsorption capacity beyond 6%. Yuan et al. (Yuan et al., 2018) performed DFT simulations on porous graphene decorated with Ti atoms to calculate the hydrogen adsorption capacity. They reported that hydrogen molecules are adsorbed with a binding energy of -0.457 eV, and the gravimetric hydrogen storage capacity is 6.11 wt.%. Also, their study reported that six hydrogen molecules are adsorbed on both sides of the Ti-porous graphene system at 300 K. An experimental study performed by Goharibajestani et al. (Goharibajestani et al., 2019) for the hydrogen adsorption capacity of reduced graphene oxide decorated with different transition metal oxides revealed that the addition of TiO₂ results in the highest isosteric heat of adsorption of 13 kJ/mol for hydrogen. Rafique et al. (Rafique et al., 2019) calculated the hydrogen adsorption capacity of Ti-doped double vacancy hexagonal boron nitride monolayered sheets using DFT. They found that only three H₂ molecules are attached on a single side of the sheet, whereas five molecules can be attached with high binding energy and thermodynamic stability on both sides of the sheet. Kag et al. (Kag et al., 2021) performed MDS for enhancement of the hydrogen adsorption capacity of graphene sheets via strain and defect engineering. They concluded that strained and defective sheets are more active for hydrogen adsorption and sheets with 1% monovacancy defects at 100 bar pressure achieves 9.3 wt.% and 2.2 wt.% at 77 K and 300 K, respectively. Nuhnen and Janiak (Nuhnen and Janiak, 2020) analyzed

the adsorption of isotherms of CO₂, SO₂, and H₂ gases at two temperatures on MOFs. They discussed multiple methods to calculate the isosteric enthalpy of adsorption at different but close temperature isotherms ≤ 20 K. Corral et al. (López-Corral et al., 2010b) found that the addition of palladium atoms on monolayer graphene and carbon nanotubes (CNTs) results in a higher binding energy for hydrogen at the bridge site of carbon bonds. The theoretical investigation also reveals that functionalized carbon-based materials are inclined to achieve a higher gravimetric density of hydrogen. The adsorption energy per hydrogen molecule is greater in palladium-implanted graphene consisting of double vacancy defects (Sen et al., 2013b). Their initial principal calculation established that the system is stable at 800 K and is suitable for hydrogen storage. According to the results of an experimental investigation on the effect of nitrogen (N) doping on palladium implanted graphene sheets for hydrogen adsorption capacities (Vinayan et al., 2012), the N-doped graphene sheets allow highly dispersed and strongly adhered palladium atoms enhancing the overall adsorption capacity by almost 272% at room temperature and a moderated pressure of 2 MPa. Xiao et al. (Xiao et al., 2016) performed an experimental investigation on the N-doped porous carbon material, and reports a very significant enhancement in specific area of the doped material. At 77 K and 1 bar pressure, the doped material proved to be effective for functionalization and was shown to be capable of adsorbing a greater quantity of hydrogen. Das et al. (Das et al., 2018) investigated the N-doped porous carbon material experimentally using EDTA as a precursor; they discovered that a high number of pores are formed during the material's synthesis. It is desirable to have a high number of holes with a small pore diameter to maximize the hydrogen storage capacity of porous carbon material. Graphene sheets doped with different atoms were analyzed for the storage of hydrogen using DFT (Zhang et al., 2013). It has been shown that doping with metallic atoms changes the material's electronic structure, increasing hydrogen adsorption. It has also been discovered that sheets implanted with Ti atoms had the highest interaction energy of all the dopants tested. Also, according to a study based on density functional theory (DFT) (Liu et al., 2010), the hydrogen adsorption energy of graphene sheets with titanium (Ti) implantation is enhanced to 0.23-0.60 eV and reports a central role of hybridization (between its 3d orbital and the molecular hydrogen) in enhanced binding. Nachimuthu et al. (Nachimuthu et al., 2014) demonstrated that boron-doped graphene implanted with

transition metals can store hydrogen with a lower activation energy, allowing for reversible storage at ambient temperatures. According to a first principle investigation, Li-implanted graphene with DV defects can adsorb a greater amount of hydrogen (Seenithurai et al., 2014b). Both sides of the sheet with lithium adatoms can store up to 7.26 wt.% of hydrogen and desorb it under ambient conditions. Ismail et al. (Ismail et al., 2015) conducted an experimental study on reduced graphene oxide coated with palladium and nickel for hydrogen storage. They synthesized the graphene oxide (GO) using the Hummer technique and discovered that doped reduced graphene oxide (RGO) can hold a greater amount of hydrogen at temperatures of 80 and 300 K and at reasonable pressures. Lebon et al. (Lebon et al., 2015b) conducted DFT calculations on Ti-doped graphene nanoribbons intended for hydrogen storage. They discovered that hydrogen adsorbs with a binding energy well within the limitations of physisorption and that the system may be employed to reversibly store hydrogen at gravimetric densities. Wang et al. (Wang et al., 2017) used DFT to analyze the hydrogen adsorption behavior of porous graphene sheets coated with lithium metal. They discovered that lithium metals are scattered uniformly without aggregating and can hold hydrogen up to 12.11 wt.%. The bandgap shifts have also increased with the rise in lithium content, and the system reflects an increase in hydrogen adsorption capacity under ambient circumstances. A recent DFT study (Yuan et al., 2018) on hydrogen adsorption capacity of porous graphene sheets with Ti adatoms reports that the Ti adatoms prefers adsorb on the hexagon center with a strong binding energy of 3.65 eV and the hydrogen adsorption on the sheet is owed to both the polarization as well as orbital hybridization of the C, Ti, and H₂ atoms. They also revealed that the six hydrogen molecules can be adsorbed on both sides of the sheet and the porous sheet with Ti adatoms is also stable at 300 K and no external pressure. A study of the literature indicates an abundance of experimental and first-principles studies on carbon nanostructures (CNT, graphene, etc.). Molecular dynamics (MD) simulations were employed in past investigations of metal implanted graphene; transition metal implantation have been extensively explored because of their strong interaction with hydrogen molecules and high hydrogen storage capacity.

1.7 Scope and objectives of the present research

The Literature survey suggests numerous experimental and first-principle studies on

carbon nanostructures CNTs, CNFs, graphene, and metal hydrides for hydrogen storage have been performed. Some of the studies were performed on graphene using the MD simulations (Alian et al., 2017c; Ansari et al., 2012; Blanco-Rey et al., 2016; Borodin et al., 2011; Georgakis et al., 2014; Rozada et al., 2015; Sen et al., 2013b; Simon et al., 2010; Sunnardianto et al., 2021). These works of literature lack a detailed computational and analytical study of the effect of temperature, pressure, strain, defects, grain boundaries, and different functionalization's on the hydrogen adsorption capacity of a graphene sheet. To the best of our knowledge, there is no single study that reports the effect of the aforementioned parameters on the hydrogen adsorption on graphene layer using the MD simulations. Therefore, it is of great significance to investigate hydrogen adsorption behavior on graphene to analyze the gravimetric density and their adsorption kinetics.

We can better understand the factors that affect hydrogen adsorption capacity using sophisticated MD Simulations. We investigated hydrogen adsorption behavior of graphene under varied conditions using a novel energy-centered method. Low temperature and high pressures are the extreme optimum conditions where a high gravimetric density can be achieved with a low-cost volumetric setup. We also modified graphene by providing the strain and different structural defects like monovacancy (MV), Stone Wales (SW), and double vacancy (DV), to analyze their H₂ adsorption and desorption capability. We further examined the effects of pressure and temperature on adsorption and desorption phenomena using the MD simulations. Additionally, we widen our research scope beyond this and find the change in mechanical strength when we created different defects in graphene layer as mentioned above. We also focused our attention towards creating a novel pathway to enhance the hydrogen adsorption capability of polycrystalline graphene sheets (PGs) by decorating Ti atoms via large-scale MDS and observe the adsorption and desorption mechanisms. Fracture mechanics analysis of PGs and Ti-PGs is also carried out under uniaxial tensile loadings. The isosteric enthalpy of adsorption for Ti-decorated PGs is also determined to analyze the mechanics of adsorption at different temperature ranges. Subsequently, graphene sheets with various vacancy defects were modeled and then subjected to N atoms and Ti adatoms to enhance their adsorption capacity.

To accomplish this, an innovative framework was developed to improve the conceptual knowledge of graphene adsorption properties. The present work attempts to simulate

hydrogen adsorption on graphene using MDS and introduce a pathway for creating novel materials based on computational techniques that can hold hydrogen at ambient conditions through physisorption. The conducted research is a significant contribution to the scientific community due to the recent shift in advanced nanomaterials with improved hydrogen storage capabilities. As a strikingly novel research goal, it is intended to accomplish the tasks of the following objectives:

- Develop a framework to estimate the hydrogen adsorption capacity of pristine graphene at different temperatures and pressures using MD simulations. (Chapter 3)
- Study the adsorption capacity of graphene sheets through strain and defect engineering via classical MD simulations. (Chapter 4)
- Study the adsorption and desorption behavior of titanium-decorated polycrystalline graphene toward hydrogen storage using MD simulations. (Chapter 5)
- Study the unified impact of Ti adatom and N doping on hydrogen gas adsorption capabilities of defected graphene sheets using MD simulations. (Chapter 6)

1.8 Organization of the thesis

The remaining part of the thesis is organized as follows:

- Chapter 2 deals with the atomistic modelling framework used in current work.
- Chapter 3 presents temperature and pressure effects on hydrogen adsorption in graphene, aiming for high gravimetric density using computational MDS, proposing novel material development.
- Chapter 4 explores the effect of strain and defects on graphene's hydrogen storage behavior under various temperatures and pressures using MD simulation.
- Chapter 5 presents the hydrogen storage in PGs, Ti-decorated PGs using MDS, analyzing adsorption, desorption, fracture mechanics, and isosteric enthalpy under various conditions.
- Chapter 6 explores N doping, Ti adatom effects on hydrogen storage in defective graphene via MD simulations, focusing on dopant concentration, temperature, pressure.

- Chapter 7 summarizes the major conclusions drawn from the research work presented in the thesis and the further scope of research on enhancement of hydrogen storage. The references are alphabetically listed at the end of thesis.

Chapter 2

Classical Molecular Dynamics

In this chapter we outlined the general atomistic modeling framework of current research and basic theoretical methods used in the thesis. Detailed methodology and simulation parameters used for different research problems of the thesis are provided in the concerned chapters.

2.1 Atomistic modelling

A nanomechanics is the new area of mechanics which studies the properties and behavior of nanoscale material and structures in response to different types of loading conditions. A structure with at least one dimension less than 100 nm (10^{-7} m) is considered to be a nanostructure. A thorough understanding of physics of nanomaterials is required to design and development of their structures. This is usually achieved by using nanomechanical experiments or theoretical models. For instance, TEM, SEM, AFM, nano indenter etc. are widely used to characterize nanomaterials experimentally (Feynman et al., 1992). Conducting experiments at the nanoscale-level is very expensive, complicated and time-consuming due to the involvement of atomistic parameters. Therefore, atomistic modelling plays a vital role in nanomechanics.

Over the past three decades, there has been a rapid advancement in research activity on nanostructured materials, with the long-term promise to tailor-design material properties at the nanoscale level. In such noble efforts, computations are playing an important role in complementing experiments. Atomistic modelling-based techniques use modern computing power to include every atom of the system under consideration in its modelling as interacting particles are the foundation of materials science. Virtual computational experiments can significantly reduce the cost and accelerate the time scales of understanding and developing new materials without synthesizing them. A schematic illustration of typical atomistic modelling strategies is shown in Figure 2.1.

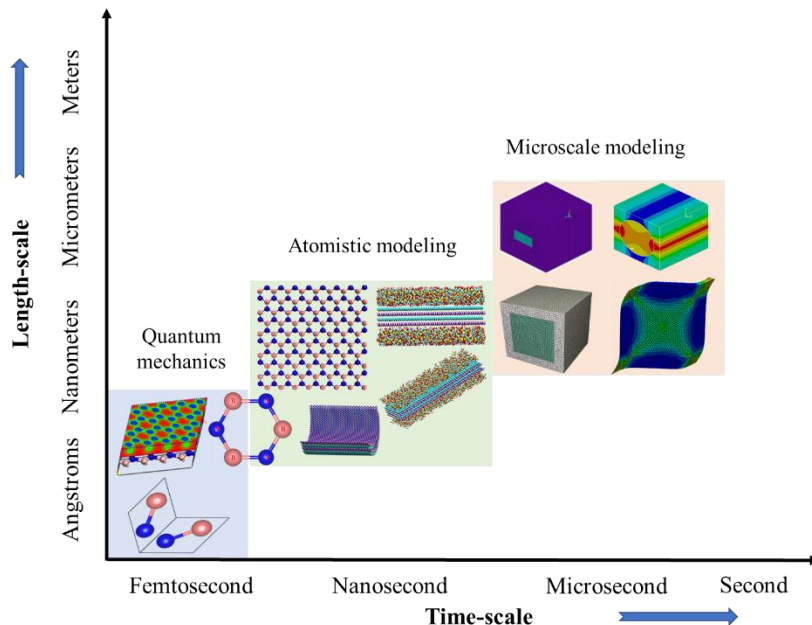


Figure 2.1 A schematic description of atomistic modelling strategies with representative length and time scales for computational simulations. Some typical nanostructures such as BN nanotube, nanosheet, and nanocomposite are shown as illustrative examples for different length and time scales.

2.2 Molecular dynamics (MD) simulations

Molecular dynamics (MD) technique is one of the most efficient and attractive atomistic modelling method (Rapaport, 1996). In MD technique, atom is assumed as an interacting classical particle and the interatomic interactions between the atoms are described using molecular mechanics force fields.

2.2.1 Introduction

MD simulation is one of the most widely used techniques in the study of nanostructures. It is a nanomechanics-based computer simulation technique in which the time evaluation of a set of interatomic interactions of atoms is followed by integrating their equations of motion with time. The time dependent integration is done by solving the classical Newton's equations of motion, numerically. The interatomic interactions between the atoms of nanostructure are described by molecular mechanics potential fields. MD simulations allow to gain insight into nanostructure under the specific condition that is impossible to study experimentally. This serves a complement to conventional experiments with cheaper and faster simulations. MD simulation have an advantage over classical models as it provides a route to dynamical properties of the molecular system such as time-

dependent responses to perturbations, transport coefficients, thermo-mechanical properties, rheological properties and spectra, and many more characteristics of the system. Therefore, the MD simulation were performed in the current study using an open source software, Large-scale Atomic/Molecular Massively Parallel Simulator (LAMMPS) (Plimpton, 1995), and atomic interactions in GNSs were modeled in terms of a three-body Tersoff-type potential force field (Tersoff, 1989, 1988).

2.2.2 Equations of motion

MD simulation is divided into two basic steps. The first step involves the determination of interatomic interacting forces of atoms using molecular mechanics-based potential fields. The second step involves the tracing of trajectories of movements of atoms by integrating the equations of motion. The interatomic forces between the atoms are determined from the gradient of a molecular mechanic's potential field during the simulations, and force acting on an atom α is given by (Rapaport, 1996):

$$\mathbf{F}_{\alpha,\mathbf{x}} = - \frac{\partial E_{\alpha}}{\partial \mathbf{r}_{\alpha,\mathbf{x}}} \quad (2.1)$$

where $\mathbf{F}_{\alpha,\mathbf{x}}$ is the force exerted on the atom, E_{α} is the potential energy and $\mathbf{r}_{\alpha,\mathbf{x}}$ is the position of an atom α in \mathbf{x} direction. The potential energy of atoms is obtained from a molecular mechanic's potential field, a suitable potential field to simulate the GNSs is discussed in section 2.2.8. The force acting on each atom is known and using Newton's second law, the acceleration of each atom can be obtained by:

$$\mathbf{F}_{\alpha,\mathbf{x}} = m_{\alpha} \frac{d^2 \mathbf{r}_{\alpha,\mathbf{x}}}{dt^2} = m_{\alpha} \frac{d\mathbf{v}_{\alpha,\mathbf{x}}}{dt} = m_{\alpha} \mathbf{a}_{\alpha,\mathbf{x}} \quad (2.2)$$

where m_{α} , $\mathbf{v}_{\alpha,\mathbf{x}}$ and $\mathbf{a}_{\alpha,\mathbf{x}}$ are the mass and acceleration of atom α in, \mathbf{x} direction, respectively.

A system of atoms is allowed to move under accelerations for a period called time step. The velocity of atom α after each time step can be obtained and using it, the position of atom α can be calculated. Therefore, to calculate the trajectory of atoms, only the initial positions of atoms, initial distribution of velocities and accelerations are required, and these are obtained by the gradient of potential energy function. The initial distribution of velocities of the atoms of the system is usually determined from a random distribution with

the magnitudes conforming to the required temperature and corrected so there is no overall momentum in the atoms of the systems, i.e.,

$$\mathbf{P}_\alpha = \sum_{\alpha=1}^N m_\alpha \mathbf{v}_\alpha = 0 \quad (2.3)$$

The velocities \mathbf{v}_α are often chosen randomly from a gaussian distribution at a given temperature, a velocity \mathbf{v}_x in the \mathbf{x} direction at a temperature T

$$\mathbf{v}_{\alpha,x} = \left(\frac{K_B T}{m_\alpha}\right)^{1/2} \times \text{Gaussian}(0,1) \quad (2.4)$$

The temperature in terms of the sum of the squares of the momenta of particles in a system, which is related to the kinetic energy approach

$$T = \frac{2}{3NK_B} \sum_{\alpha=1}^N \frac{\mathbf{P}_\alpha^2}{2m_\alpha} \quad (2.5)$$

where N is the number of atoms in the system and k_B is Boltzmann's constant. This method is particularly useful in computational physics and molecular dynamics simulations, where momenta are often more readily computed or tracked than velocities.

2.2.3 Integration algorithms

The potential energy of interatomic interactions of atoms is the function of their positions in the system. Numerous numerical algorithms such as leap-frog algorithm (Hockney et al., 1970), velocity Verlet algorithm (Swope et al., 1982) etc. have been developed for integrating the equations of motion. MD is usually applied to a large-scale atomistic model and the energy evaluation is time-consuming as well as memory requirement is also large. To generate the correct statistical ensembles, energy conservation is required.

Thus, the basic criteria for the right integrator for simulations are as follows:

- It should be fast, ideally requiring only one energy evaluation per time-step.
- It should require less computer memory.
- It should permit the use of a relatively long time-step.
- It must show functional conservation of energy.

In all the integration algorithms, the positions, velocities and accelerations of atoms can be approximated by a Taylor series expansion (Rapaport, 2011).

$$\mathbf{r}(t_0 + \delta t) = \mathbf{r}(t_0) + \mathbf{v}(t_0)\delta t + \frac{1}{2}\mathbf{a}(t_0)\delta t^2 + \dots \quad (2.6)$$

$$\mathbf{v}(t_0 + \delta t) = \mathbf{v}(t_0) + \mathbf{a}(t_0)\delta t + \frac{1}{2}\mathbf{b}(t_0)\delta t^2 + \dots \quad (2.7)$$

$$\mathbf{a}(t_0 + \delta t) = \mathbf{a}(t_0) + \mathbf{b}(t_0)\delta t + \dots \quad (2.8)$$

where \mathbf{r} , \mathbf{v} , and \mathbf{a} are the positions, velocity and acceleration of an atom, respectively, t_0 is the initial time, and δt is the time step. The change in \mathbf{r} and \mathbf{v} with δt are graphically represented in Figure 2.2.

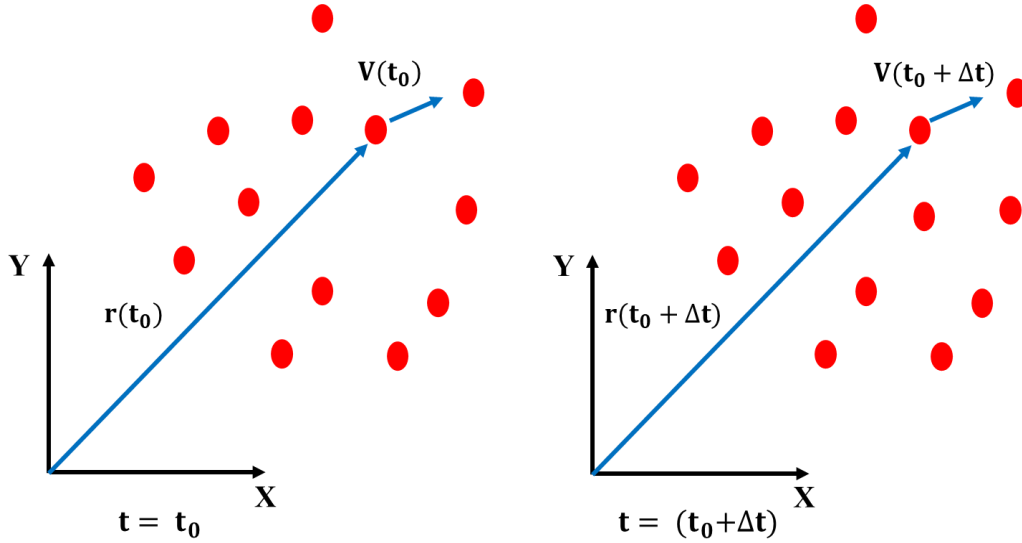


Figure 2.2 Variation in the positions and velocities of atoms with the time.

The following numerous numerical algorithms have been developed for integrating the equations of motion in the literature:

The Leap-Frog Algorithm (Rapaport, 1996): The velocities are first calculated at the time $t + \frac{1}{2}\delta t$ and using this velocities position r obtained at time $t + \delta t$. The advantage of this algorithm is that the velocities are explicitly calculated; however, the disadvantage is that they are not calculated at the same time as the positions.

$$\mathbf{r}(t_0 + \delta t) = \mathbf{r}(t_0) + \mathbf{v}\left(t_0 + \frac{1}{2}\delta t\right)\delta t \quad (2.9)$$

$$\mathbf{v}\left(t_0 + \frac{1}{2}\delta t\right) = \mathbf{v}\left(t_0 - \frac{1}{2}\delta t\right) + \mathbf{a}(t_0)\delta t \quad (2.10)$$

The velocities at time t can be approximated by:

$$\mathbf{v}(t_0) = \frac{1}{2}\left[\mathbf{v}\left(t_0 - \frac{1}{2}\delta t\right) + \mathbf{v}\left(t_0 + \frac{1}{2}\delta t\right)\right] \quad (2.11)$$

Beeman's Algorithm (Rapaport, 1996): This algorithm is closely related to the Verlet algorithm. According to that the respective position and velocity of atoms can be described by,

$$\mathbf{r}(t_0 + \delta t) = \mathbf{r}(t_0) + \mathbf{v}(t_0)\delta t + \frac{2}{3}\mathbf{a}(t_0)\delta t^2 - \frac{1}{6}\mathbf{a}(t_0 - \delta t)\delta t^2 \quad (2.12)$$

$$\mathbf{v}(t_0 + \delta t) = \mathbf{v}(t_0) + \mathbf{v}(t_0)\delta t + \frac{1}{3}\mathbf{a}(t_0)\delta t + \frac{5}{6}\mathbf{a}(t_0)\delta t - \frac{1}{6}\mathbf{a}(t_0 - \delta t)\delta t^2 \quad (2.13)$$

The advantage of this algorithm is that it provides a more accurate expression for the velocities and better energy conservation and the disadvantage is that the more complex expressions make the calculations more expensive.

The velocity Verlet Algorithm (Swope et al., 1982): During the MD simulations the new positions and velocities of atoms in the system are obtained using a numerical integration method. According to the velocity Verlet method, position and velocity of atoms can be described by,

$$\mathbf{v}\left(t_o + \frac{\delta t}{2}\right) = \mathbf{v}(t_o) + \mathbf{a}(t_o)\frac{\delta t}{2} \quad (2.14)$$

$$\mathbf{r}(t_o + \delta t) = \mathbf{r}(t_o) + \mathbf{v}\left(t_o + \frac{\delta t}{2}\right)\delta t \quad (2.15)$$

$$\mathbf{v}(t_o + \delta t) = \mathbf{v}\left(t_o + \frac{\delta t}{2}\right) + \mathbf{a}(t_o)\delta t \quad (2.16)$$

The velocity Verlet algorithm is required less computer memory as only one set of positions, velocities and forces need to calculate at one time. Due to that fact this algorithm mostly used in MD simulation of atomic systems.

In order to simulate the real system during MD simulation, controlling temperature and pressure is necessary. The temperature control is achieved by modifying the velocities of atoms, while pressure is controlled by adjusting the size of the simulation box. A review of commonly used techniques to control temperature and pressure is given below.

2.2.4 Temperature control

Temperature is a fundamental parameter that reflects the thermal state of a system. The temperature of a system is the average of kinetic energies of all the atoms, which is calculated from the atomic velocities and can be given as (Rapaport, 1996):

$$T = \frac{1}{k_B N_f} \sum_{i,\alpha} m^\alpha (\mathbf{v}_i^\alpha)^2 \quad (2.17)$$

where k_B is Boltzmann's constant, N_f is the total translational degree of freedom of the system, m^α is the mass of atom α , and \mathbf{v}_i^α is the velocity of atom α in \mathbf{i} direction.

During the simulation, it is not possible to keep temperature constant due to the fluctuations of velocities of atoms of the system. Hence, the average value of temperature can be maintained during the MD simulation. According to Eq. (2.17), the system temperature depends on the velocities of atoms. Therefore, by scaling the velocities of atoms, the temperature can be controlled, which is usually accomplished by a thermostat. The most commonly used thermostats are Anderson, Berendsen and Nose-Hoover.

Anderson thermostat (Andersen et al., 1980): This is the most straightforward thermostat and, in this method, the velocity of a random particle is replaced by a value chosen from the Maxwell-Boltzmann distribution for a given temperature. Anderson thermostat is computationally expensive.

Berendsen thermostat (Berendsen et al., 1984): This is the most commonly used thermostat due to its simplicity and easy implementation. To maintain the constant temperature during the simulation, the system is coupled to an external heat bath source with fixed temperature T_0 . The velocities of atoms are scaled at each time state such that the change in the rate of temperature is proportional to the difference in temperature:

$$\frac{dT(t)}{dt} = \frac{1}{\tau}(T - T(t)) \quad (2.18)$$

This method provides an exponential decay of the system towards the target temperature using a factor λ :

$$\lambda = \left[1 - \frac{\delta t}{\tau} \left(\frac{T - T_0}{T}\right)\right]^{\frac{1}{2}} \quad (2.19)$$

where τ is the characteristic relaxation time, δt is the time-step size, T the instantaneous temperature, and T_0 is the target temperature. This method maintains a constant temperature with good approximation and the temperature can be controlled by changing τ and adjusting T_0 .

Nosé-Hoover thermostat (Shuichi Nosé et al., 1984): This is a method for performing constant-temperature dynamics that produces true canonical ensembles in both momentum and coordinate spaces. This method was used in this study because it is one of

the best-considered thermostats among all the thermostats (Hünenberger et al., 2005). This thermostat uses a friction factor (μ) to alter the equations of motion, as follows:

$$\frac{d\mu(t)}{dt} = \frac{k_B N_f}{Q} (T(t) - T_0) \quad (2.20)$$

where Q is the effective mass of thermostat:

$$Q = k_B N_f T(t) \tau_T^2 \quad (2.21)$$

where τ_T is the specified time constant for the fluctuations of temperature. To achieve the smooth temperature transition, the value of the time constant is usually considered in the order of hundred-time steps. The modified equation of motion is defined by,

$$\mathbf{a} = \frac{f(t)}{m} - \mu(t)\mathbf{v}(t) \quad (2.22)$$

Then using the velocity verlet algorithm the updated position and velocities are obtained.

2.2.5 Pressure control

The pressure is a basic thermodynamic variable that provides the state of system of atoms and is defined as:

$$P = \frac{1}{3V} \sum_{\alpha=1}^3 \left(\sum_{i=1}^N m_i \mathbf{v}_{i\alpha} \cdot \mathbf{v}_{i\alpha} - \sum_{i=1}^N \sum_{j>i}^N \mathbf{r}_{ij\alpha} \cdot \mathbf{F}_{ij\alpha} \right) \quad (2.23)$$

where V is the volume of system, i and j are assigned number to neighboring atoms that passes from one atom to the other neighboring atom (N), $\mathbf{r}_{ij\alpha}$ are the positions of atoms i and j in α direction. Term $\mathbf{F}_{ij\alpha}$ is the force on atom i due to atom j , and $\mathbf{v}_{i\alpha}$ and m_i are the velocity and mass of atom i , respectively in α direction. The value of $\alpha = 1,2,3$ for 3 dimensional systems.

During the simulation, the pressure of the system of atoms can be adjusted by changing the dimension of the simulation box. This can be achieved using the barostat during the simulations, and the most commonly used barostats are Berendsen (Berendsen et al., 1984) and Nose-Hoover barostat (Martyna et al., 1994).

Berendsen barostat maintains the pressure of a system at a target value. The Berendsen method couples the system to a pressure bath. At each time step, size of the simulation box and the coordinates of atoms are rescaled. At each step, x , y and z coordinates of each atom are scaled by the factor, μ :

$$\mu = \left[1 - \frac{\delta t}{\tau} \gamma [P - P_0] \right]^{\frac{1}{3}} \quad (2.24)$$

where P is the instantaneous pressure, P_0 is the target pressure and δt is the time step, γ is a factor related to the compressibility of the system. The cartesian components of the unit cell vectors are scaled by the same factor. Berendsen's method is less reliable compared to the Nose-Hoover method (Hünenberger, 2005).

Nose-Hoover barostat (η) is defined as: (Hoover, 1985; Shüichi Nosé, 1984)

$$\frac{d\eta}{dt} = \frac{1}{k_B N_f T_0 \tau_p^2} V(t) (P(t) - P_0) \quad (2.25)$$

where τ_p is the specified time constant for pressure fluctuations and its value usually on the order of thousands of time steps to achieve a smooth pressure fluctuation. The controlled volume of the system is determined by using the following relation:

$$\frac{dV(t)}{dt} = [3\eta(t)]V(t) \quad (2.26)$$

2.2.6 Statistical ensembles

The whole universe is governed by the thermodynamics laws through the transfer of energy between matter. This is attributed to the change in the total energy of the system. This process is very complex to consider directly, therefore, several parts of the universe, i.e., the system is considered separately, and it can be described using an ensemble. An ensemble is a collection of all possible states of the real systems that have identical thermodynamic or macroscopic states but have different microscopic states. The commonly used ensembles are (i) constant N, V and E (NVE) or microcanonical ensemble, (ii) constant N, V and T (NVT) or canonical ensemble, and (iii) constant N, P and T (NPT) or isothermal-isobaric ensemble. The N, V, E, T and P denote the number of atoms, volume, energy, temperature and pressure of the system of atoms, respectively. The graphical representations of ensembles are shown in Figure 2.3.

Microcanonical ensemble (NVE) is derived from Newton's law of motion without any pressure and temperature control (Rapaport, 1996). The energy of the system is conserved during the simulations. The NVE ensemble is a statistical ensemble that allows

to keep constant specified total energy of all the possible states of mechanical systems. The system's energy, volume, composition and shape are kept constant in all possible states of the system.

Canonical ensemble (NVT) can be obtained by maintaining the constant thermodynamic temperature and total volume and number of particles in the system. (Rapaport, 1996). The NVT ensemble is a statistical mechanics ensemble that denotes the possible states of the mechanical system in thermal equilibrium of heat bath at finite temperature. The system allows only to exchange the energy from the heat bath and the energy is no longer constant.

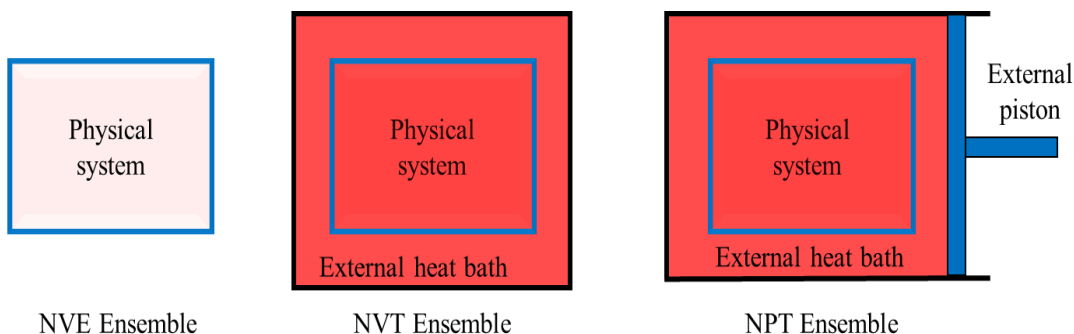


Figure 2.3 Graphical representation of the microcanonical (NVE) ensemble, the canonical (NVT) ensemble and the isothermal-isobaric (NPT) ensemble (Gale et al., 2012).

Isothermal-Isobaric ensemble (NPT) allows the control of both the pressure and temperature of the system (Rapaport, 1996). The NPT ensemble is a statistical mechanical ensemble that maintains a constant total number of particles, pressure, and temperature. NPT can also be used during equilibration to obtain the desired pressure and temperature before changing to the constant-energy and constant-volume ensembles.

2.2.7 Potential fields

The potential field is a mathematical description of the potential energy of a system of interacting atoms. The empirical relation of parameters of potential energy in potential fields are derived from both high-level quantum mechanical calculations and experimental studies. To simulate the different molecular systems required a unique potential field. The general form of a potential field as a function of energy and can be defined as

$$E_{total} = E_{covalent} + E_{non\ covalent} \quad (2.27)$$

where E_{total} , $E_{covalent}$, and $E_{non\ covalent}$ are the total energy, covalent energy, and non-covalent energy, respectively, and interatomic relative motions in molecular

mechanics depict in Figure 2.4. The components of covalent and noncovalent energies can be expressed as

$$E_{covalent} = E_{bond} + E_{angle} + E_{dihedral} + E_{out-of-plane} \quad (2.28)$$

$$E_{non\ covalent} = E_{electrostatic} + E_{vander\ Waals} \quad (2.29)$$

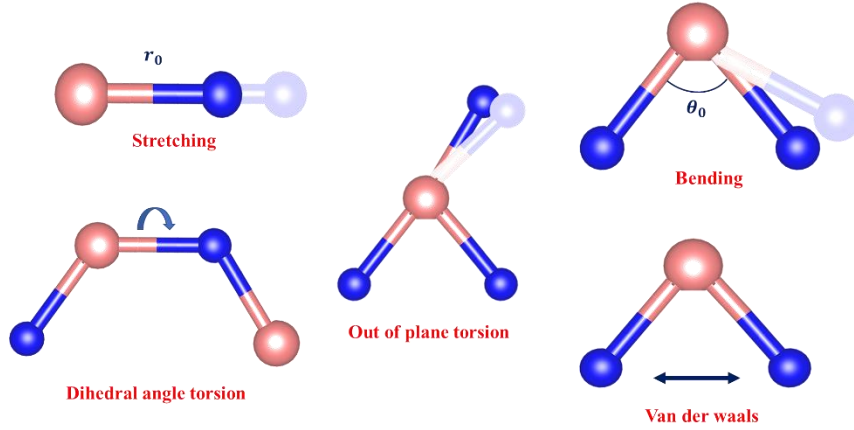


Figure 2.4 Interatomic relative motions in molecular mechanics.

In case of non-bonded van der Waals interaction between individual B and N atoms (see Figure 2.4), there is a variety of used potentials in the literature. Commonly, the non-bonded interactions are expressed as Lennard-Jones (L-J) or Morse potentials (Rahman et al., 1994). In the current study, the L-J term and a coulombic-term was used which is expressed by (Akiner et al., 2016):

$$U(\mathbf{r}_{ij}) = 4\varepsilon_{ij} \left[\left(\frac{D_{ij}}{\mathbf{r}_{ij}} \right)^{12} - \left(\frac{D_{ij}}{\mathbf{r}_{ij}} \right)^6 \right] + K_C q_i q_j \mathbf{r}_{ij}^{-1} \quad (2.30)$$

where $U(\mathbf{r})$ is potential energy (PE) between two particles, \mathbf{r}_{ij} is the finite distance at which the inter-particle potential is zero between atoms i and j in adjacent layers, while ε is a parameter determining the depth of the potential well, D_{ij} is the diameter of the atom (a length-scale parameter of the atom determining the position of the potential minimum). K_C is Coulombic constant and q_i is the partial charge of the i^{th} atom. Meanwhile, the partial charge q for the L-J potential is taken as 1.1378 eV and the cutoff distance of L-J interaction is set to 12 Å. The parameters of L-J potential are summarized in Table 2.1. The exact functional form of a potential field depends on the type and condition of the simulation. The all-atom potential fields provide the parameters for each and every type of atom in a

system, while the united-atom potential fields stipulate parameters only for specific types of atoms (Sun, 1998).

In the literature, Morse potential, reactive empirical bond order (REBO) potential, adaptive intermolecular reactive empirical bond order (AIREBO) potential fields are being used to simulate graphene interatomic interactions, and three-body Tersoff-Brenner potential force field is being used to simulate N interaction with graphene (Tersoff et al., 1988). Morse potential field is two body potential field, which does not represent the systems with many-body interactions, such as graphene. The MD simulations in this study have been conducted using Tersoff potentials field, which are many-body potentials.

2.2.8 Tersoff potential force field

Tersoff potential force field is used for semiconductors and insulators. It is parameterized from the empirical data and particularly suited for graphene based nanostructures with B and N interactions. In the MD simulation, the interactions between B, C and N atoms of a sheet were described using the Tersoff potential force field (Tersoff, 1988, 1989a). The Tersoff potential was obtained by empirically fitting the parameters obtained from either experiments or first-principles calculations. Note that the Tersoff potential has been successfully employed in numerous studies to evaluate the electromechanical response of GNSs and tube (Mortazavi and Rémond, 2012; Zhao and Xue, 2013; Zhang et al., 2017; Vijayaraghavan and Zhang, 2018; Zhang and Zhou, 2018). According to the Tersoff potential, an analytical form of the total energy E between two neighbouring atoms i and j were defined as:

$$E = \sum_i E_i = \frac{1}{2} \sum_{i \neq j} V_{ij} \quad (2.31)$$

$$V_{ij} = f_C(r_{ij})[f_R(r_{ij}) + b_{ij}f_A(r_{ij})] \quad (2.32)$$

$$V_{ij}^R = f_C(r_{ij})f_R(r_{ij}) \quad (2.33)$$

$$V_{ij}^A = f_C(r_{ij})b_{ij}f_A(r_{ij}) \quad (2.34)$$

where, E is the total energy of the system, E_i is the site energy and V_{ij} is the bond energy. The indices i and j run over the atoms of the system. Term r_{ij} is the distance between atom i and atom j , while b_{ij} is the bond angle term which depends on the local coordination of atoms around atom i . Terms f_R and f_A are the repulsive and attractive pair

potentials, respectively. Term $f_C(r_{ij})$ is the cut-off function provided to limit the range of the potential and thus saves the computational time. The cutoff function $f_C(r_{ij})$ is expressed as:

$$f_C(r_{ij}) = \begin{cases} 1 & r_{ij} < R_{ij} \\ \frac{1}{2} + \frac{1}{2} \cos\left(\pi \frac{r_{ij} - R_{ij}}{S_{ij} - R_{ij}}\right) & R_{ij} < r_{ij} < S_{ij} \\ 0 & r_{ij} > R_{ij} \end{cases} \quad (2.35)$$

where R and D are model specific parameters.

The two-body repulsion $f_R(r_{ij})$ and attraction $f_A(r_{ij})$ terms are as follows:

$$f_R(r_{ij}) = -A_{ij} \exp(-\lambda_{ij}^I r_{ij}) \quad (2.36)$$

$$f_A(r_{ij}) = -B_{ij} \exp(-\lambda_{ij}^{II} r_{ij}) \quad (2.37)$$

In Eq. (2.32), b_{ij} is the strength of the attractive term and can be expressed as:

$$b_{ij} = (1 + \beta^n \zeta_{ij}^n)^{-\frac{1}{2n}} \quad (2.38)$$

$$\text{where } \zeta_{ij} = \sum_{k \neq i,j} f_C(r_{ijk}) g(\theta_{ijk}) \exp[\lambda_3^m (r_{ij} - r_{ik})^3] \quad (2.39)$$

$$g(\theta) = \gamma_{ijk} \left(1 + \frac{c^2}{d^2} - \frac{c^2}{d^2 + (h - \cos \theta)^2} \right) \quad (2.40)$$

in which n , c , d , and h are the constants, and they can be determined from the data describing the interactions between B, C and N atoms. These constants are taken from the Ref. (Albe et al., 1997; Matsunaga et al., 2000; KInacI et al., 2012), as listed in Table 2.1.

The n , β , λ_{ij}^I , B , λ_{ij}^{II} , and A parameters are only used for two-body interactions. The m , γ , λ_3^m , c , d , and $\cos \theta_0$ parameters are only used for three-body interactions. The R and D adjustable parameters are used for both two-body and three-body interactions. The value of $m = 3$, $\beta = 0$, and $\gamma = 1$ are taken as constant. Term $g(\theta)$ is dependent on the angular deformation and θ is the angle between two vectors r_{ij} and r_{ik} . The different parameters λ_{ij}^I , λ_{ij}^{II} , A_{ij} , B_{ij} , R_{ij} , and S_{ij} for species i and j can be calculated using the mixing rules:

$$\lambda_{ij}^I = \frac{1}{2} (\lambda_i^I + \lambda_j^I) \quad (2.41)$$

$$\lambda_{ij}^{II} = \frac{1}{2} (\lambda_i^{II} + \lambda_j^{II}) \quad (2.42)$$

$$A_{ij} = (A_i \cdot A_j)^{1/2} \quad (2.43)$$

$$B_{ij} = (B_i \cdot B_j)^{1/2} \quad (2.44)$$

$$R_{ij} = (R_i \cdot R_j)^{1/2} \quad (2.45)$$

$$S_{ij} = (S_i \cdot S_j)^{1/2} \quad (2.46)$$

Table 2.1 Parameters used in Tersoff potentials for B-B, N-N, B-N, C-C, C-N and C-B interactions.

(Albe et al., 1997; KInacI et al., 2012; Matsunaga et al., 2000).

Parameter	B-B	N-N	B-N	C-C	C-N	C-B
m	3	3	3	3	3	3
γ	1	1	1	1	1	1
λ_3^m (Å ⁻¹)	0	0	1.992	0	0	0
c	0.562	17.795	1092.928	38049.450	38049.450	38049.450
d	0.001	5.948	12.38	4.348	4.348	4.348
h	0.5	0	-0.541	-0.930	-0.930	-0.930
n	3.992	0.618	0.364	0.727	0.727	0.727
β	0.000	0.019	0.000	0.000	0.000	0.000
λ_{ij}^H	2.077	2.627	2.784	2.211	2.205	2.205
B (eV)	1173.196	2563.560	3624	430	339.068	387.575
R (Å)	2	2	2.3	1.95	1.952	1.952
D (Å)	0.1	0.1	0.5	0.15	0.1	0.1
λ_{ij}^L	2.237	2.829	2.99	3.487	3.527	3.527
A (eV)	1404.052	2978.952	4483.250	1393.645	1386.781	1386.781
ϵ (kcal/mol)	0.000	0.007	0.249	-	-	-
D (Å)	0.000	3.750	3.146	-	-	-

2.2.9 Molecular dynamics parameters

Time-step: The length of time between two consecutive iterations in a MD simulation is called the time step. A time step should be less than 10% of the vibration period of an atom and, time-step of 0.5 fs to 0.8 fs provides excellent results for carbon-based structure (Arachchige, 2012; Kundalwal and Choyal, 2018a). However, researchers used time steps from 0.1 fs to 1 fs to simulate uniaxial tensile tests of GNSs (Kumar et al., 2016; Mortazavi and Cuniberti, 2014). They used three-body Tersoff potential force field

for simulating the BN-based nanostructure using LAMMPS. The selection of time-step depends on the computational efficiency and required accuracy of the simulations. The larger value of time steps increases the computational efficiency, while it reduces the accuracy of the simulations. The smaller time steps may improve the accuracy of the simulations. Therefore, the time step controls the trade-off between computational efficiency and accuracy in the MD simulations. If the value of time-step is too large, then the system might become unstable. Therefore, first, we investigated the effect of time step on the simulation of the mechanical deformation test of GNS. In order to investigate this, a set of MD simulations was performed on a $50 \text{ \AA} \times 50 \text{ \AA}$ GNS with time steps of 0.1 fs, 0.5 fs, and 1 fs. All other MD parameters were kept constant, and the values mentioned in the following sections. The results indicate that the stress-strain curves of GNS obtained with different time steps are identical. It can be concluded that a time-step between 0.1 fs and 1 fs could be used to simulate the mechanical deformation tests of GNSs. A time step of 0.5 fs, which is the most commonly used in various literatures, will be used in all the MD simulations hereafter.

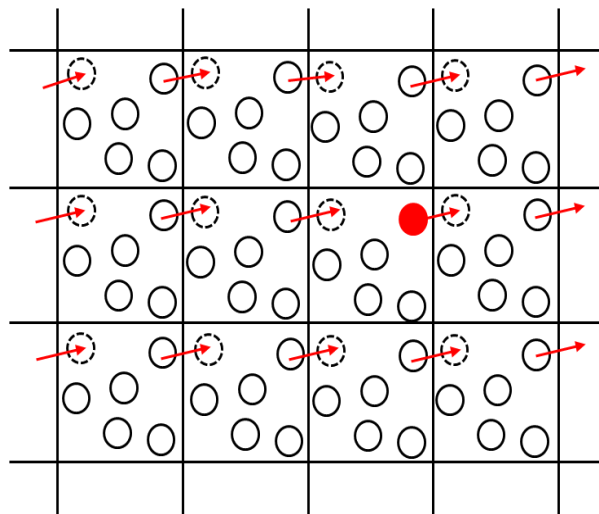


Figure 2.5 Graphical representation of the PBCs of the middlebox. The arrows indicate the directions of the velocities of atoms. The atoms in the middlebox can interact with atoms in the neighbouring boxes without having any boundary effects.

Periodic boundary conditions: The term periodic boundary condition (PBC) (Allen, 2004) refers to the simulation of structures consisting of a periodic lattice of identical subunits. The effects of edges in the systems such as GNSs should be eliminated in MD simulations in order to obtain their bulk properties. Therefore, an extremely large

system of GNS can be simulated via MD simulation by ensuring that the edges and surfaces have only a small effect on its bulk properties, but this approach is computationally expensive. To reduce the computational efforts, the use of PBCs in the MD simulation is the most efficient method to simulate an infinitely large system. In PBCs, the cubical simulation box was replicated throughout space to form an infinite lattice as shown for a 2D case in Figure 2.5. During the MD simulation, when an atom moves in the central box, then its periodic images in every other box also move exactly in the same way. Thus, when an atom leaves the box during the simulation, then it is replaced by an image particle that enters from the opposite side so the number of particles/atoms in the central box remains same and the system under consideration does not possess any edges. Therefore, the PBC was used to eliminate the effects of free edges of GNSs (Dewapriya et al., 2014; Yamakov et al., 2017).

2.2.10 MD simulator

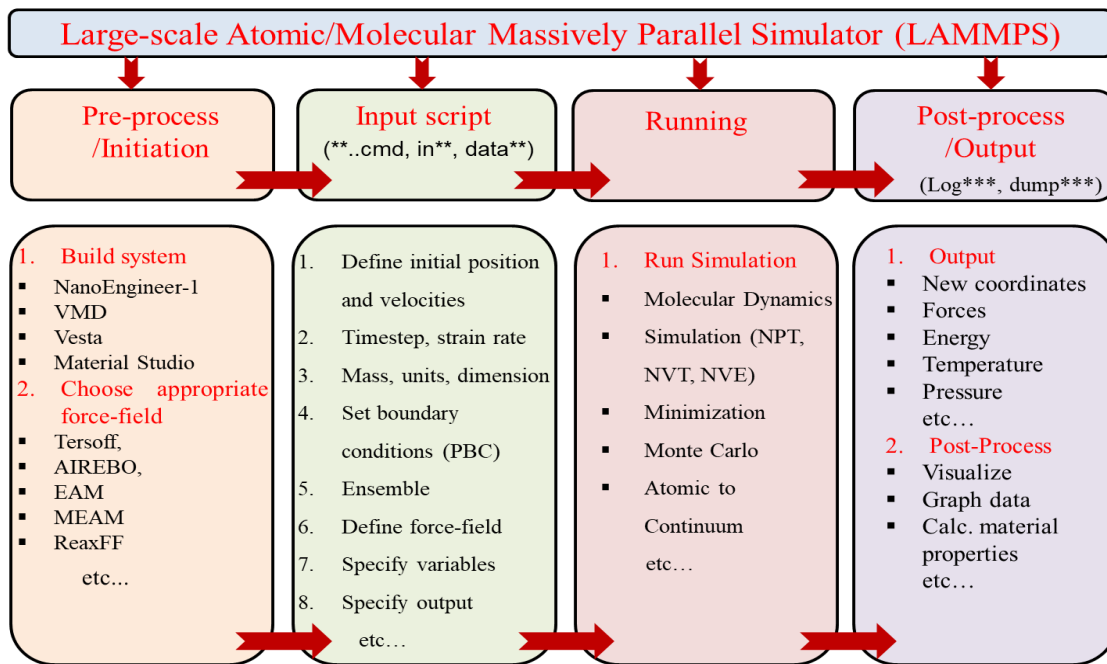


Figure 2.6 The overview of LAMMPS input script

All the MD simulation were performed in LAMMPS. The Large-scale Atomic/Molecular Massively Parallel Simulator (LAMMPS) is a classical MD simulation software that is widely used in a variety of applications at the atomistic level (S. J. Plimpton, 1995) and it allows parallel particle simulations at the atomic, meso and

continuum scales. It allows to simulate atomic, chemical or biological models at a microscopic scale. LAMMPS was developed at the Sandia National Laboratories and is written in C++ code. It is free and open-source software that continues updated by Sandia National Laboratories (Plimpton et al., 1995) and other researchers worldwide.

The MD simulator LAMMPS requires a different script to perform the MDSs, such as input script, atom coordinates of the system and potential field. The formulation of LAMMPS input script is shown in Figure 2.6, and this script can be divided into four sections: preprocess/initiation, input script, running, and output/postprocess.

- (i) **Preprocess/initiation:** build the atomic systems using the following software (NanoEngineer-1, VMD and OVITO) and also choose appropriate force field (Tersoff, AIERBO, EAM and ReaxFF etc.) that provides the interatomic interaction of the atomic systems.
- (ii) **Inputs script:** defines the atom coordinates of the system and potential field. The boundary conditions and units of the MD parameters are set in the initialization part of the input script. Different units and boundary conditions are available in LAMMPS package. The use of metal units is mandatory for the Tersoff-potential force-field. In the metal units, the units of time, distance and energy are picoseconds (ps), Angstroms (Å) and electron-volts (eV), respectively. The choice of boundary condition depends on the type of simulation and can be chosen as periodic and non-periodic. The atoms coordinates (x , y and z) and types are defined under the atom definition section. In all performed MD simulations, the atom coordinates given in a different file. During the simulation, this file is called when the input file is executed.
- (iii) **Running:** the simulation parameters, potential field coefficients and output options are given in the third section of the input script. The basic simulation parameters, such as temperature, pressure, time etc., are defined here. The temperature and pressure controlling methods are implemented in LAMMPS, such as Berendsen and Nose-Hoover methods. The thermodynamics ensemble is also implemented in the third section of the LAMMPS such as NVE, NVT and NPT ensembles. During simulation, LAMMPS allows to compute time and spatial averages of physical quantities, such as pressure, temperature, energies, stresses, etc. and separate text

files can be obtained at specified time intervals. During the simulation, LAMMPS allows to deform the simulation box. During the simulation, nanostructure is also deformed along with the simulation box.

- (iv) **Postprocess/output:** the output of the MD simulations from the LAMMPS can be obtained as *log.Lammps* file after the pre-specified number of time steps. The output of LAMMPS contains all the position information pertaining to atoms at every time-step. However, LAMMPS does not have the functional visualization capability to display the various trajectories directly. Therefore, additional visualization software is required for analyzing the results obtained more easily. In this regard, the VMD (Dalke et al., 1996) and OVITO (Stukowski et al., 2010) software can be used which are capable of reading the LAMMPS output data and rendering informative figures.

The theory behind the MD simulations in this chapter will be used for investigating the hydrogen adsorption capacity of functionalized graphene sheets in subsequent chapters. The hydrogen adsorption capacity of pristine, polycrystalline and defect containing GNS, GNS subjected to strain, and N- and Ti- doped GNS is studied in the next chapters.

Chapter 3

Simulation framework and adsorption behavior analysis of GNS

In this chapter, we delve into the establishment of a comprehensive simulation framework for studying hydrogen adsorption on graphene under varying temperature and pressure conditions. We also introduce a novel method for potential energy distribution (PED) estimation to determine the hydrogen adsorption gravimetric density. The chapter presents a detailed analysis of the adsorption behavior, including adsorption isotherms at different temperatures and pressures, revealing the optimal conditions for hydrogen storage.

3.1 Introduction

Graphene (Novoselov et al., 2004), a single layer that is made of hexagonally arranged carbon atoms, demonstrates excellent mechanical strength (Alian et al., 2017a; Lee et al., 2008a), thermal stability (Balandin et al., 2008), and possesses a high specific surface area (SSA) of $\sim 2630 \text{ m}^2\text{g}^{-1}$ (Zhu et al., 2010). In addition to these remarkable properties, graphene has good reversibility, faster adsorption, and desorption kinetics (Patchkovskii et al., 2005). Graphene also has potential application in nanocomposites as a reinforcement agent (Kumar et al., 2020), gas barrier (Cui et al., 2016a), and nanoelectromechanical systems (S.I. Kundalwal et al., 2017).

The search for efficient solid-state hydrogen storage solutions has prominently featured the role of SSA and chemical modifications in enhancing the gravimetric density of hydrogen storage within various carbon-based materials (Klechikov et al., 2015; Ma et al., 2009a). Various chemical reactions can also be used to tune graphene properties and their interlayer spacing (Prabhu et al., 2020), thus enhancing the adsorption properties. Lijie Ci et al. experimentally found that the annealed CNT at the temperature range of 1700-2200 $^{\circ}\text{C}$ can store the hydrogen up to 3.98 wt% (Ci et al., 2002). M. Hirscher and B.

Panella experimentally found that the carbon nanostructure has a high SSA and can store hydrogen up to 4.5 wt% at 77K (Hirscher and Panella, 2005). Hangkyo jin et al. experimentally investigate the microporous activated carbons with an SSA of 2800 m²/g and get the maximum hydrogen adsorption of 1 wt% at room temperature (Jin et al., 2007). Subsequently, S.F. Braga et al. studied carbon nanoscrolls for hydrogen adsorption using the atomistic molecular dynamics simulations. They revealed that at a lower temperature of 77 K, hydrogen molecules are adsorbed, and on increasing the temperature to 300 K, desorption occurs (Braga et al., 2007). Valentino R. Cooper et al. studied hydrogen adsorption on single-layer graphene using the newly developed van der Waal density functional. They concluded that the molecular hydrogen, closer to the surface, has greater interaction with graphene (Cooper et al., 2012). Guo et al. studied the hydrogen adsorption capacity of the graphene sheet generated by the arc discharge method in an atmosphere of hydrogen at lower pressure. Experimentally, their results reveal that the graphene sheet with few layers exhibits the highest capacity of electrochemical hydrogen storage and good cyclic performance (Guo et al., 2013). Yong-Chae Chung et al. studied the boron substituted Li decorated graphene sheet using the density functional theory (DFT) with the *ab initio* package (VASP). Their results reveal that the boron substitution enhances the ability of lithium decorated sheets for hydrogen adsorption and gets the high hydrogen storage capacity much beyond the target value set up by the department of energy (DOE) in 2010 (Park et al., 2010a). Sharma et al. studied the hydrogen adsorption on platinum decorated GNS using the first principle study. Their results reveal that the platinum decorated GNS efficiently store hydrogen compared to pristine, and their design and synthesis can store hydrogen (Sharma et al., 2019).

A literature survey over the two decades suggests that numerous experimental and theoretical studies were performed on CNTs, CNFs, graphene, and metal hydrides for hydrogen storage. These works of literature lack a detailed computational and analytical study of the effect of temperature and pressure on the hydrogen adsorption capacity of a graphene sheet. Therefore, it is of great significance to investigate hydrogen adsorption behavior on graphene to analyze the gravimetric density and adsorption energy of hydrogen. Low temperature and high pressures are the extreme optimum conditions where a high gravimetric density can be achieved with a low-cost volumetric setup. For instance,

hydrogen is transported in the cryogenic vessels in large quantities and at high pressures in composite pressure vessels at high gravimetric density (Barthelemy et al., 2017; Barthélémy, 2012; Weinberger and Lamari, 2009). To the best of current authors' knowledge, no single MDS study is performed to study the effect of temperature and pressure on graphene sheets' hydrogen adsorption capacity. Keeping in mind the practical application aspects related to hydrogen storage process at low temperature (77 to 300 K) and pressures in the range of 1 to 10 MPa, we investigated hydrogen adsorption behavior of graphene under varied conditions using a novel energy-centered method. To accomplish this, an innovative framework needs to be developed to improve the conceptual knowledge of graphene adsorption properties. The present chapter attempts to simulate hydrogen adsorption on monolayer graphene using MDS and introduce a pathway for creating novel materials based on computational techniques that can hold hydrogen at ambient conditions through physisorption. The obtained isotherms at different temperatures are fitted over the available isotherm models.

3.2 MD modeling of GNS

MDS allows studying the mechanisms and behaviours of nanomaterials which no other simulation methods can perform in a computationally efficient manner. MDS carried out in this study uses the LAMMPS, an open-source package developed by Sandia National laboratories (Steve Plimpton, 1995). To study the influence of graphene sheet size, square sheets with edge lengths ranging from 50 Å to 200 Å were considered. The results of MDS were fitted over different analytical adsorption equations. To carry out MDS, firstly, a graphene sheet surrounded by hydrogen molecules was modeled. Perfect graphene lattices were modeled separately using VESTA (Momma and Izumi, 2011a) and then imported into the simulation box. The modeled graphene sheet structures were relaxed to achieve stress-free sheets at a given temperature, and then H₂ molecules were randomly added surrounding the graphene sheet.

In all MD calculations, periodic boundary conditions were applied in in-plane directions of graphene sheet to eliminate the free edge effects, and out-of-plane direction was applied with periodic boundary conditions with large dimensions to avoid any interlayer interactions. Figure 3.1(a) illustrates the relaxed graphene sheet placed in the

middle of the simulation box and hydrogen molecules randomly surrounding the sheet. The interatomic interactions of the carbon atoms in the graphene sheet was modeled using Tersoff potential (Tersoff, 1989b) as it has been successfully applied to predict properties of graphene (Bu et al., 2009; Javvaji et al., 2016; Thomas and Ajith, 2014; Volokh, 2012). A detailed discussed of Tersoff potential is available in section 2.2.8.

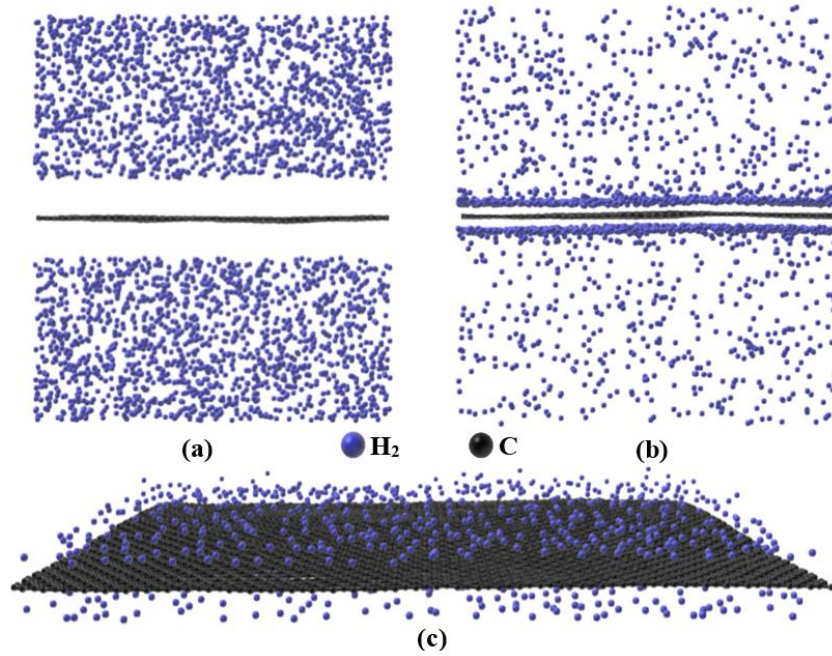


Figure 3.1 System configuration of graphene sheet and H_2 molecules: (a) Initial system configuration with relaxed graphene sheet, (b) system at simulation time 1 ns, and (c) adsorbed H_2 molecules around graphene.

A physisorption based interaction between H_2 molecules and carbon atoms was modeled using Lennard-Jones (LJ) 12-6 potential.

$$u_{ij} = 4\varepsilon_{ij} \left[\left(\frac{\sigma_{ij}}{r} \right)^{12} - \left(\frac{\sigma_{ij}}{r} \right)^6 \right] \quad (3.1)$$

where u_{ij} is the pairwise interaction energy, and ε_{ij} and σ_{ij} are the well-depth energy and the distance at which pair interaction energy goes to zero, respectively. The cut-off distance of 12 \AA ($\sim 4\sigma$) was chosen for LJ interactions. Table 3.1 describes the LJ potential parameters used in this work reported by Cracknell (Cracknell, 2001). Carbon atoms and H_2 molecules interactions were obtained using Lorentz-Berthelot mixing rules:

$$\varepsilon_{ij} = \sqrt{\varepsilon_i \cdot \varepsilon_j} \quad \& \quad \sigma_{ij} = \frac{\sigma_i + \sigma_j}{2} \quad (3.2)$$

Table 3.1 LJ interaction parameters for carbon atoms and hydrogen molecules.

Parameter	H ₂ -H ₂	C-C
ϵ [Kcal/mol]	0.067962	0.055641
σ [Å]	2.96	3.40

Initially, carbon atoms were arranged according to the ideal graphene atomic configuration at 0K with a lattice constant of 0.148 nm. For all simulations, a timestep of 1.0 fs was considered to encapsulate the adsorption dynamics. The conjugate gradient method was applied with an energy convergence of 10^{-10} Kcal mol⁻¹ (Kundalwal et al., 2020a) to obtain an energy minimized graphene sheet. After energy minimization, the system was equilibrated for 250 ps under isothermal and isobaric conditions to achieve a stress-free and equilibrated sheet in planar directions. H₂ molecules were added randomly in the simulation box above and below the relaxed graphene sheet. The number of H₂ molecules added to the system was arbitrarily chosen to be about six molecules of H₂ per carbon atom in the graphene sheet. A long equilibration step of 15 ns was performed to ensure an equilibrated system with uniform distribution, as shown in Figure 3.2. It can be seen that the system gets equilibrated after 2 ns, so to save computational time, all subsequent MDS runs were conducted for 4 ns. In all MDS, the system ran for 250 ps to achieve the desired system temperature and pressure. After that, an equilibration run of 4 ns was performed under the isothermal and isobaric conditions. Nosé-Hoover thermostat and barostat were used for controlling the temperature and pressure of the system, respectively. The above simulation steps were performed multiple times for each set of pressure and temperature to obtain reliable results.

The amount of hydrogen adsorbed was calculated by observing the distribution of potential energy of each particle, discussed in detail in section 3.6. The gravimetric density (wt%) was calculated by

$$wt. \% = \frac{W_{H_2-adsorbed}}{W_{H_2-adsorbed} + W_{C-Graphene}} \quad (3.3)$$

where, $w_{H_2-adsorbed}$ is the weight of adsorbed hydrogen molecules and $w_{C-Graphene}$ is the weight percentage of the graphene sheet. The adsorption energy was calculated by

$$E_{adsorption} = E_{Graphene+H_2} - (E_{Graphene} + E_{H_2}) \quad (3.4)$$

where, $E_{Graphene}$ is the potential energy of graphene sheet, E_{H_2} is the potential energy of one hydrogen molecule and $E_{Graphene+H_2}$ is the potential energy of the graphene sheet with adsorbed hydrogen molecules.

3.3 Adsorption isotherms

To explain the adsorption behavior between adsorbate (hydrogen) and adsorbent (graphene) at different pressures, various analytical expressions of adsorption isotherms are used in this work. These equations define the adsorption capacity (q) of the adsorbent as a function of pressure (p) for a specific temperature.

3.3.1 Langmuir isotherm

The Langmuir theory (Langmuir, 1918) assumes that the adsorbate adheres to the adsorbent and covers the surface forming a monolayer of the adsorbate. It also assumes the adsorption to be homogeneous, i.e., all adsorption sites are equal. At low pressures, this dense state allows higher volumes to be stored by sorption than is possible by compression.

$$q = \frac{q_{mL}K_L p}{1 + K_L p} \quad (3.5)$$

where q is the amount of adsorbate on the surface adsorbent at a pressure p . q_{mL} is the constant reflecting theoretical monolayer capacity, and K_L is the affinity constant or Langmuir constant, which indicates the strength of adsorption.

3.3.2 Freundlich isotherm

Freundlich isotherm (Freundlich, 1907) defines the surface heterogeneity and the exponential distribution of active sites and their energies. Its expression applies to heterogeneous adsorption, and the expression is given by

$$q = K_L p^{n_F} \quad (3.6)$$

where K_F is the Freundlich constant, and n_F is the heterogeneity factor.

3.3.3 Sips (Langmuir–Freundlich) isotherm

The Sips isotherm (Sips, 1948) is a combination of the Langmuir and Freundlich isotherms. Its general expression is

$$q = \frac{q_{mS}K_S p^{n_S}}{1 + K_S p^{n_S}} \quad (3.7)$$

where q_{mS} is the maximum adsorption capacity at a particular temperature, K_S is the Sips constant, and n_S is the heterogeneity factor. If n_S is equal to 1, the Sips equation is reduced to the Langmuir equation, and the surface is homogeneous.

3.3.4 Toth isotherm

Toth isotherm (Tóth, 2000) is another modification of Langmuir isotherm with an aim to reduce the actual and predicted data differences. It is also applicable to heterogeneous adsorption. Most sites have adsorption energy lower than the maximum. The Toth equation assumes the asymmetrical quasi-Gaussian distribution of site energies.

$$q = \frac{q_{mT}K_T p}{(1 + (K_T p)^{n_T})^{1/n_T}} \quad (3.8)$$

where q_{mT} is the constant reflecting maximum adsorption capacity, K_T is the Toth constant, and n_T is the heterogeneity factor, $0 < n_T \leq 1$, For homogeneous adsorption $n_T = 1$ and the Toth equation reduces to the Langmuir equation.

3.3.5 Fritz–Schlunder isotherm

The Fritz–Schlunder isotherm (Fritz and Schlunder, 1974) expression is described as follows:

$$q = \frac{q_{mFS}K_{FS}p}{1 + q_{mFS}p^{n_{FS}}} \quad (3.9)$$

where q_{mFS} is a constant reflecting maximum adsorption capacity (mg g^{-1}), K_{FS} is the Fritz–Schlunder equilibrium constant, and n_{FS} is the Fritz–Schlunder model exponent.

3.4 Error functions

Accuracy of linear fits are described by Pearson correlation coefficient, R . The R describes the strength of the linear relationship between two variables. To carry out a curve fitting for the above isotherms, non-linear fitting methods are required. Unlike linear regression, non-linear regression requires the minimization of an objective function using the iterative methods. Here, the objective function is the error function. The minimization of the error function between the actual and predicted data leads to a converged solution. Thus, an accurate set of parameters can be obtained for the adsorption isotherm models. Five different error functions are used in this work.

3.4.1 The sum of the squares of the errors

The sum of the squares of the errors (SSE) is the most widely used error function:

$$SSE = \sum_{i=1}^n (q_p - q_a)_i^2 \quad (3.10)$$

where q_p is the adsorption capacity predicted, q_a is the adsorption capacity obtained from MDS, and n is the number of data points in the adsorption isotherm obtained from MDS. The major drawback is that it provides a better fit for high-pressure ranges only. As iterations proceed, the square of the errors becomes very small for the high-pressure values the minimization converges.

3.4.2 The hybrid fractional error function

The hybrid fractional error function (HYBRID) was developed to improve the fitting of SSE at low-pressure ranges:

$$HYBRID = \frac{100}{n-p} \sum_{i=1}^n \left[\frac{(q_p - q_a)^2}{q_a} \right]_i \quad (3.11)$$

where p is the number of parameters that are free to evolve with iterations, i.e., denotes the degree of freedom for the minimization. Each sum of the squares of the error values is divided by the actual adsorption values.

3.4.3 The average relative error function

The average relative error (ARE) is a function developed for minimizing the fractional error distribution across the entire range of pressures. Its expression is given by

$$ARE = \frac{100}{n} \sum_{i=1}^n \left| \frac{q_p - q_a}{q_a} \right|_i \quad (3.12)$$

The number of experimental points is included as a divisor.

3.4.4 The marquardt's percent standard deviation

The Marquardt's percent standard deviation (MPSD) is expressed as

$$MPSD = 100 \sqrt{\frac{1}{n-p} \sum_{i=1}^n \left(\frac{q_p - q_a}{q_a} \right)_i^2} \quad (3.13)$$

and is similar to a geometric mean error distribution modified according to the number of degrees of freedom of the system.

3.4.5 The sum of the absolute errors function.

The sum of the absolute errors (SAE) is similar to the SSE. The expression is given by

$$SAE = \sum_{i=1}^n |q_p - q_a|_i \quad (3.14)$$

Thus, the parameters obtained from this fit also has the same limitation of providing a better fit at only high-pressure ranges.

3.5 Accuracy of the fit

The level of accuracy or the goodness of the fit depends upon the thorough interpretations of the adsorption isotherms. Meaningful comparisons of the set of obtained parameters can be made by using the sum of the normalized errors (SNE) described by Porter et al. (Porter et al., 1999), Standard Error (SE), and Correlation index or the coefficient of determination (R^2). To calculate SNE, the errors obtained from each isotherm

fitting equation for each error function were normalized with the maximum value and summed. The standard error (SE) of y values is defined as

$$SE = \sqrt{\frac{\sum(y_a - y_p)^2}{n - p}} \quad (3.15)$$

and, Correlation index or the coefficient of determination (R^2) determined by the relation

$$R^2 = 1 - \frac{\sum(y_a - y_p)^2}{\sum(y_a - y_{mean})^2} \quad (3.16)$$

The above relation is used for determining the goodness of fit; it determines the strength of the relation between the dependent and independent variables. In non-linear models, a high correlation can exist even if the model differs from the actual data. So, an examination of the residuals is also performed.

3.6 Results and discussion

Temperature and pressure are critical parameters for gas adsorption and desorption phenomena as well as application point of view. For example, consider a boiler of the central heating system of building which can be considered as energetically excellent as almost all the energy content of oil fuel/natural gas is converted to heat. Exergetically, the boiler is not a good idea because it exergo-thermodynamically generates flame temperatures up to 1000 °C for achieving the objective of supplying room radiator temperatures of some 60–70 °C. If a hydrogen-fueled low temperature fuel cell is installed then it firstly generates electricity from 35 to 40% of the fuel's energy, with the remaining heat still sufficing to warm the building over most of the year [55]. Another low temperature energetic use includes the space industry and submersibles, which could have been non-existent without the highly energetic hydrogen, where low temperature high efficiency hydrogen fuel cells can guarantee their extended travel [55]. Keeping in mind such practical applications, the simulations were performed at lower temperatures in the pressure range of 1 - 10MPa to store hydrogen, resulting in a significant amount of hydrogen adsorption (illustrated in Figure 3.1 (b) and (c)). We also validated current simulations in the same range of temperatures and pressures. To simulate an accurate

adsorption molecular dynamics, an equilibrated system should be achieved. A system with equilibrated potential energy, temperature, and pressure indicates a stable system. Figure 3.2 (a) shows the time evolution of the system properties at temperature and pressure of 77 K and 1 MPa, respectively, for 15 ns. It can be observed that the system was stable and equilibrated throughout the simulation after raising it to the desired temperature and pressure. This is due to the thermodynamic controls that keep the system to the desired temperature and pressure during the simulation and then a relaxation of the system achieving an equilibrated system. Figure 3.2. (b) shows that the initial potential energy and weight percentage value gradually reaches an equilibrium after increasing temperature and pressure. In all MDS, a runtime of 4 ns was chosen to save the computational time as the system equilibrates after 2 ns. The system is controlled to be in thermodynamic equilibrium, and the intermolecular interaction of the H₂ molecules repels each other as more and more hydrogen attaches itself to the graphene sheet. Gradually, H₂ molecules adhere to low potential energy sites, thus bringing the whole system to an equilibrium.

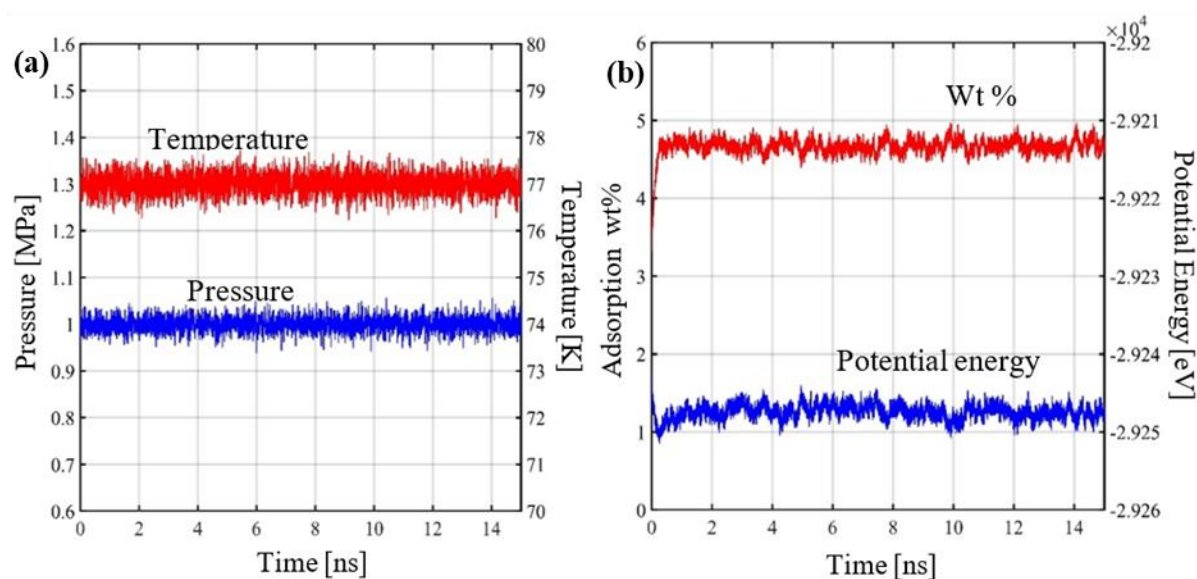


Figure 3.2 (a) Time evolution of the system at 77 K and 1 MPa, respectively, and (b) variation of potential energy of the system and adsorption of H₂ molecules with the time.

In order to calculate the hydrogen adsorption percentage, potential energy distribution patterns of H₂ molecules were observed. It was found that H₂ molecules adsorbed around the graphene sheet had lower potential energy as compared to free H₂ molecules, setting the basis for adsorption percentage estimation. Figure 3.3 shows the

potential energy distribution of each H₂ molecules around the graphene sheet at 77K and 1 MPa with a probabilistic curve fitting. It can be observed from Figure 3.3 that a local minima point exists in the energy distribution, and below this minimum point, adsorbed H₂ molecules lie, as shown in Figure 3.3 (a). For validation of the estimation method, the H₂ molecules belonging to the adsorbed potential energy were segregated and can be observed to be surrounded around the sheet as visualized in Figure 3.3 (b). Graphene sheet was kept hidden in the figure for clarity. Then, the number of adsorbed H₂ molecules were counted, and adsorption weight percentage (wt%) was calculated using Equation (3.3). An average of wt% for the last few timesteps of the equilibrated system was calculated to get an approximate adsorption value. To the best of current authors' knowledge, no other study has used such novel method to observe adsorption phenomena using MDS.

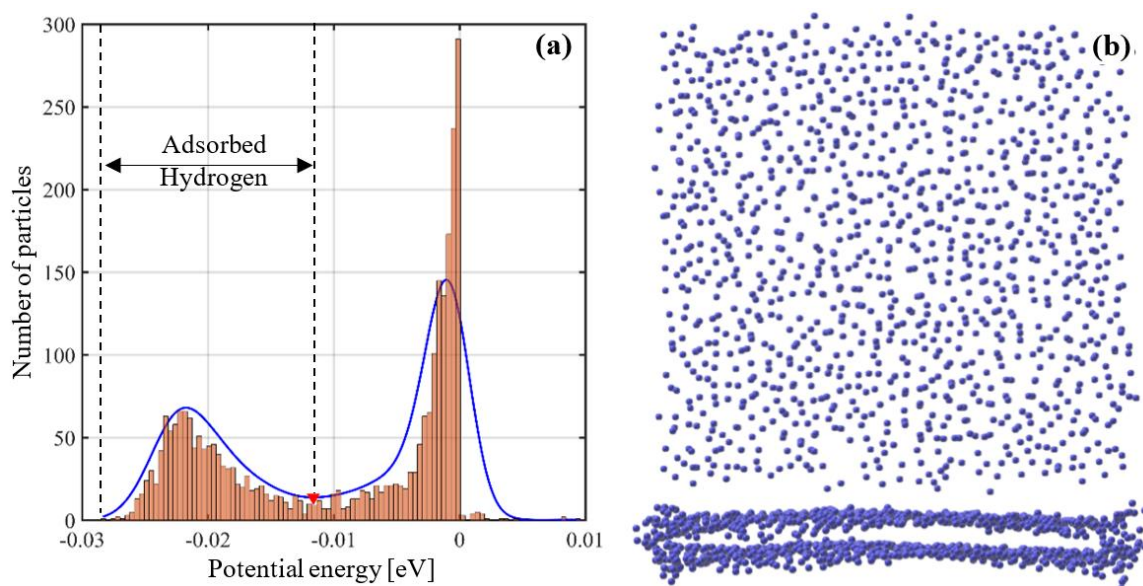


Figure 3.3 (a) Potential Energy Distribution (PED) of hydrogen molecules, and (b) front and top views of H₂ molecules at 77 K and 1 MPa.

Using the above method for estimating adsorption wt%, the hydrogen adsorption phenomenon was studied on multiple systems of graphene sheets and H₂ molecules. The adsorption energy (E_a) of the hydrogen molecules was also calculated using Equation (3.4). It should be noted that the adsorption energies calculated are negative values which signifies the strength of the attraction between H₂ molecules and graphene sheet. A higher value signifies a stronger attractive force between the adsorbate (hydrogen) and adsorbent (graphene layer).

It is well known fact that MDS with small systems tends to be very unstable, and produce false results, and large systems require a lot of computational resources. So, we considered graphene sheets of edge lengths 50 Å, 60 Å, 70 Å, 80 Å, 90 Å, 100 Å, 150 Å and 200 Å to study the influence of graphene sheet size on the adsorption energy and weight percentage of H₂ molecules. Table 3.2 shows the results of the simulations performed on these sheet sizes at 77 K and 1 MPa. It can be observed that the graphene sheet size variation has an influence on hydrogen adsorption up to a sheet edge length of 90 Å. After that, sheet size has no significant impact on the adsorption energy and wt% of small systems in MDS impose problems while controlling the temperature and pressure fluctuations. Thus, a square sheet with an edge length of 100 Å was considered for subsequent simulations to study the adsorption phenomena.

Table 3.2 The influence of sheet edge length on hydrogen adsorption at 77 K and 1 MPa.

Length [Å]	50	60	70	80	90	100	150	200
wt%	6.279	5.593	5.379	5.151	4.815	4.953	4.829	4.931
E_a [eV]	0.0207	0.0205	0.0205	0.0204	0.0199	0.0202	0.0201	0.0202

From Figure 3.2 (b) and Table 3.2, it can be seen that a pristine graphene sheet of 100 Å with a SSA of ~2630 m²/g at 77 K and 1 MPa can hold hydrogen molecules with 4.9 wt%. Current results agree well with the experimental results obtained by Klechikov et al. (Klechikov et al., 2015). The adsorption energy of the H₂ molecule on the graphene sheet was found to be 0.0202 eV. The low adsorption energy of the H₂ molecule indicate that a graphene-based system is physisorption based adsorption phenomenon, which agrees with previous literature.

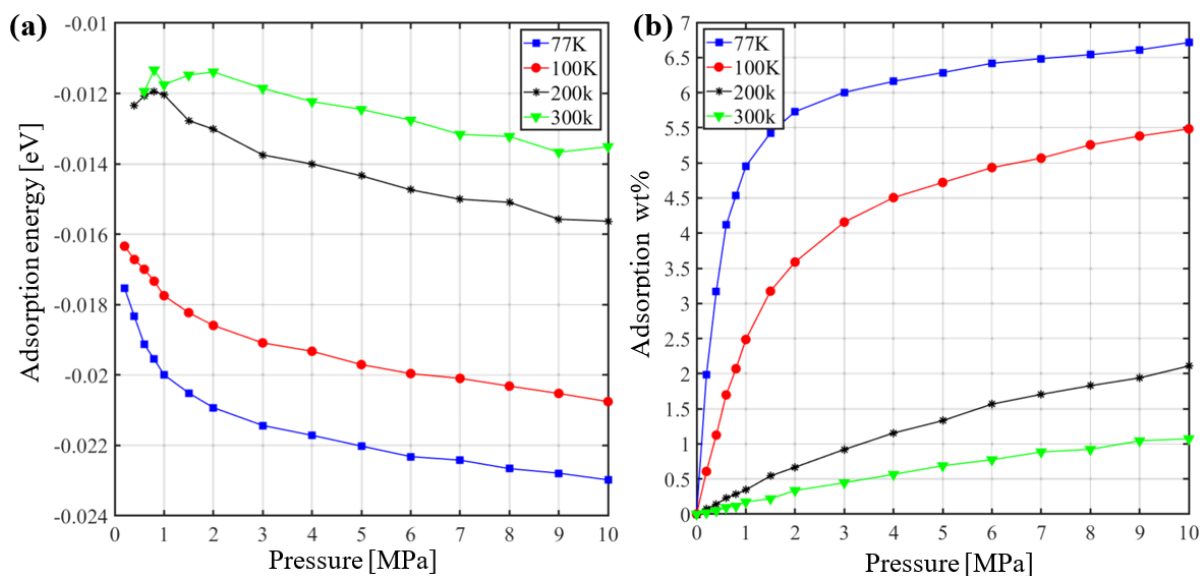


Figure 3.4 (a) Variation of adsorption energy with pressure, and (b) adsorption isotherms at 77 K, 100 K, 200 K, and 300 K.

Figure 3.4 (a) illustrates the adsorption energy of H_2 molecules adhering to the graphene sheet up to a pressure of 10 MPa at 77 K, 100 K, 200 K, and 300 K. It is observed that as the pressure increases the adsorption energy reduces to a more negative value indicating stronger adsorption between the graphene sheet and H_2 molecules. At higher temperatures, an increase in adsorption energy is observed, indicating a weaker adsorption strength. Adsorption isotherms up to a pressure of 10 MPa at 77 K, 100 K, 200 K, and 300 K are shown in Figure 3.4 (b). It can be seen that the gravimetric hydrogen density increases as the pressure rises. A higher density of H_2 molecules adheres to the adsorbent upon increasing the pressure.

At 77 K temperature, the gravimetric density increases 2.07, 2.73, 3.16, and 3.38 times as the pressure increases from 0.2 MPa to 0.6, 1.5, 5, and 10 MPa, respectively. At lower temperatures, the gravimetric density increases rapidly with the pressure, but after a certain pressure value, it reaches a saturation level. As the temperature increases, the gravimetric density of H_2 molecules largely reduces. As H_2 molecules are weakly bonded with graphene sheet, the kinetic energy of the system increases at higher temperatures, and as a result, the adsorbed H_2 molecules are desorbed, which is in agreement with previous works (Dimitrakakis et al., 2008; Lamari and Levesque, 2011). At 10 MPa pressure, the gravimetric density increases 1.96, 5.11, and 6.26 times as the temperature is lowered from

300 K to 200 K, 100 K, and 77 K. It can be seen that Figure 3.4 (b) shows the characteristics of type I adsorption isotherms out of the five characteristic isotherms described by Brunauer, Emmett, and Teller (BET) (Tien, 1994). The adsorption isotherms resulted from MDS at 77 K is used for determining the best fitting analytical model amongst the Langmuir, Freundlich, Sips, Toth, and Fritz-Schlunder models described in section 3.3. These models describe the behavior of type I adsorption isotherms. The parameters for the isotherm models were determined by minimizing the error functions described in section 3.4. Each isotherm model was fitted against the adsorption isotherm at 77 K for each error function.

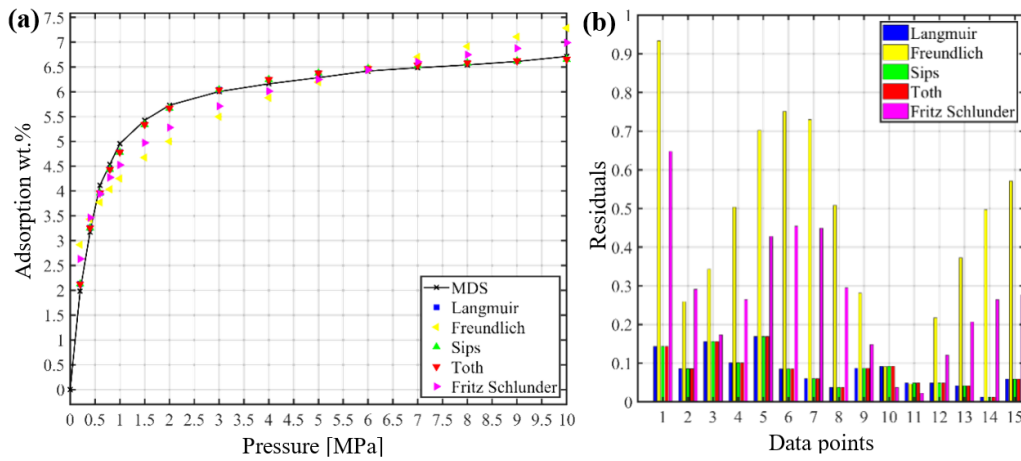


Figure 3.5 (a) Non-linear fitting, and (b) error residuals of the isotherm from MDS at 77 K.

Table 3.3 A comparison of the sum of normalized errors (SNE), standard error (SE) and coefficient of determination (R^2)

Fitting Attributes		SSE	HYBRID	ARE	MPSD	SAE
Sum of normalized error (SNE)	<i>Langmuir</i>	0.195	0.195	2.902	0.363	1.417
	<i>Freundlich</i>	1.085	1.085	0.517	2.029	0.717
	<i>Sips</i>	0.195	0.195	2.825	0.363	1.200
	<i>Toth</i>	0.195	0.195	2.809	0.363	1.104
	<i>Fritz-Schlunder</i>	0.649	0.649	0.524	1.922	1.785
Standard error (SE)	<i>Langmuir</i>	0.0099	0.0099	0.0156	0.0128	0.0115
	<i>Freundlich</i>	0.3081	0.3081	0.2693	0.4391	0.3206
	<i>Sips</i>	0.0100	0.0100	0.0166	0.0138	0.0178
	<i>Toth</i>	0.0100	0.0100	0.0165	0.0138	0.0191

Correlation index (R²)	<i>Fritz–Schlunder</i>	0.1257	0.1257	0.1127	0.1883	0.1619
	<i>Langmuir</i>	0.9953	0.9953	0.9929	0.9943	0.9941
	<i>Freundlich</i>	0.8617	0.8617	0.8345	0.8451	0.7369
	<i>Sips</i>	0.9953	0.9953	0.9930	0.9943	0.9913
	<i>Toth</i>	0.9953	0.9953	0.9931	0.9943	0.9906
	<i>Fritz–Schlunder</i>	0.9420	0.9420	0.9399	0.9267	0.8873

Table 3.3 shows the comparison of SNE, SE, R², and thereby the isotherm parameters for each model that provides the closest fit to the MDS isotherm data. Similar values of SNE, SE, and R² can be observed for the SSE and HYBRID error functions. For a good fit, the values of SNE and SE should be the lower, and the value of R² should be higher. It can be seen that the Freundlich isotherm model has the highest SNE and SE values and lowest R² value for about all error functions. The minimum values of SNE and SE are found to be 0.195 and ~0.0099, respectively, for Langmuir, Sips, and Toth isotherm models with the SSE and HYBRID error functions. The SSE and HYBRID error functions also provide the maximum value of the correlation index (R²) of magnitude 0.9953 for Langmuir, Sips, and Toth isotherms. This indicates that the Langmuir, Sips, and Toth isotherm models fit well with the provided adsorption isotherms. A more detailed analysis is provided in Figure 3.5. Figure 3.5 (a) depicts the non-linear fitting of the adsorption isotherm at 77 K obtained from MDS and Figure 3.5 (b) illustrates the error residuals of the five isotherm models at 15 data points obtained with the minimization of the HYBRID error function. Curve fitting and residual analysis of all five models are shown in both figures, and it is observed that the Freundlich and Fritz-Schlunder isotherms show poor-fitting compared to the other models. The Langmuir, Sips, and Toth isotherm models show almost equal residuals at all data points and provide an equally good curve fitting at high-pressure regions. From Figure 3.3 (a) it can be observed that the potential energy of adsorbed hydrogen molecules is a gaussian distribution, and the Toth isotherm model assumes an asymmetrical quasi gaussian distribution.

Table 3.4 The parameters obtained from Toth isotherm models at different temperatures using the HYBRID error function

Temperature [K]	K _T	n _T	q _{mT}
-----------------	----------------	----------------	-----------------

77	2.202	1.000	6.956
100	0.598	1.000	6.384
200	0.086	1.000	4.520
300	0.048	1.000	3.403

Thus, the Toth isotherm model is considered the best fitting model. Table 3.4 shows the parameters of Toth isotherms fitted for the isotherms at 77 K, 100 K, 200 K, and 300 K. The heterogeneity factor (n_T) is equal to 1 at all temperatures, thus indicating a homogenous surface. The Toth constant K_T values are found to be decreasing rapidly with increasing temperatures. Thus, indicating a firm relation of adsorption energy with temperatures. The maximum adsorption capacity or gravimetric density predicted from the Toth isotherms also decreases as the temperature increases.

3.7 Conclusions

MDS simulations were performed to investigate the hydrogen adsorption phenomena on monolayer graphene sheets. A new method based on potential energy distributions (PEDs) was developed to calculate the adsorption capacity of hydrogen on graphene sheets at varied temperature and pressure. PEDs in conjunction with MDS used in this thesis provide an accurate description of the number of adsorbed hydrogen molecules on graphene sheet. To the best of current authors' knowledge, no existing study employed such novel method for the estimation of gravimetric density. The effect of temperature and pressure on gravimetric density and adsorption energy of H_2 molecules on the graphene sheet was analysed in detail. The adsorption energies observed are far less than required for hydrogen storage systems. Due to the weak attraction between the H_2 molecule and the graphene sheet, the gravimetric density is high at only low temperatures. The H_2 molecules are desorbed at higher temperatures due to the increase in the kinetic energies. Low temperature and high pressure favour the adsorption of H_2 molecules on the graphene sheet. The adsorption isotherms obtained from MDS at different temperatures were modelled and evaluated using five existing adsorption isotherms. A thorough comparison of non-linear fit by minimizing five different error functions were performed on the basis of three attributes belonging to each isotherm model SNE, SE, and R^2 . The order of the goodness of adsorption isotherm models is as follows: Toth > Langmuir >

Sips > Fritz – Schlunder > Freundlich. The Toth isotherm was found to be the best fit model over the MDS isotherms and provides best predictions. On the basis of Toth model, the maximum adsorption capacity (wt%) values were found to be 6.956, 6.384, 4.520, 3.403 at 77 K, 100 K, 200 K, and 300 K.

Chapter 4

Hydrogen storage capacity of GNS: The role of strain and vacancy defects

This chapter investigates the influence of strain and vacancy defects on the hydrogen storage capacity of graphene nanosheets (GNS). The research explores modifications to GNS through strain application and the introduction of monovacancy, Stone-Wales, and double vacancy defects, assessing their effects on hydrogen adsorption and desorption under various pressures and temperatures.

4.1 Introduction

The exploration of hydrogen storage capabilities in graphene and its derivatives has garnered significant attention over the past decade, marked by a series of experimental and theoretical investigations that underscore the material's potential in energy applications. Initial studies by Armandi et al. laid foundational insights into hydrogen adsorption in porous graphene, achieving a maximum uptake of 2 wt% at varying temperatures, with pore structures playing a pivotal role in physisorption (Armandi et al., 2008). This was further elaborated upon by subsequent research, including Kun Xue and Zhiping Xu, who demonstrated that biaxial strain up to 10% could enhance the hydrogen storage potential of structurally deformed graphene beyond its pristine state (Xue and Xu, 2010). Srinivas et al. synthesized graphene powder through the reduction of exfoliated graphite oxide, reporting hydrogen storage capacities of 1.2 wt% and 0.1 wt% at 77 K and 298 K, respectively (Srinivas et al., 2010). Zhou et al. and subsequent studies expanded on the concept of strain engineering and metal decoration (Zhou et al., 2010), illustrating how these methods prevent metal clustering on the graphene surface and significantly improve hydrogen uptake, with notable achievements including a 2.81 wt% storage capacity at 77 K and low pressure.

Further advancements were made by exploring the effects of lithium doping and vacancy defects on graphene sheets. Hussain et al. found that biaxial strain not only increases lithium stability on the graphene sheet but also significantly enhances its hydrogen storage capacity (Hussain et al., 2012). Similarly, studies by Chattopadhyay et al. and others have shown that introducing double vacancy defects or decorating with lithium and titanium can lower adsorption energy, provide excellent stability, and increase hydrogen storage capacity to levels much beyond the targets set by the Department of Energy for 2015, with gravimetric densities reaching up to 7.26 wt% (Sen et al., 2013a). The comprehensive review by Nagar et al. and the investigation into strain engineering by Deng et al. underscore the consensus that combining structural and surface modifications, including defect engineering and metal decoration, offers a promising path forward for maximizing the hydrogen storage capabilities of graphene-based materials, thereby contributing to the advancement of energy storage technologies (Deng et al., 2018; Nagar et al., 2017b).

A literature survey over a decade suggests numerous experimental and first-principle studies on carbon nanostructures (CNT, graphene, etc.). Very few studies were performed on graphene using the MD simulation. There is no single study that reports the effect of strain and vacancy defect on hydrogen adsorption on GNS using the MD simulation to the best of current authors' knowledge. This has inspired us to conduct this study. The work stated in this chapter is based on the modification of GNS by providing the strain and different structural defects like monovacancy, Stone Wales defect, and double vacancy defect and analyze the H₂ adsorption and desorption capability. Also, examine the effects of pressure and temperature on adsorption and desorption phenomena using the MD simulation. Additionally, we widen our research scope beyond this and find the change in mechanical strength when we created different defects, as mentioned above in GNS.

4.2 MD modeling of defected GNS

In this study, the effect of uniaxial strain (De Andres and Verés, 2008)(Zhou et al., 2010) and various point defects (Banhart et al., 2011b) on GNS capacity for hydrogen adsorption is simulated at different pressure ranging from 0 bar to 100 bar and at a

temperature of 77 K and 300 K using MD simulations. To carry out MD simulation, GNS are modeled separately using the VMD and VESTA (Humphrey et al., 1996a)(Momma and Izumi, 2011b). The coordinates of the model created are then used to create a LAMMPS data file, which is then imported in LAMMPS. The interatomic interaction in GNS is described in terms of the adaptive intermolecular reactive empirical bond order (AIREBO) force field (Stuart et al., 2000); it has been successfully applied to predict the properties of graphene (Pregler et al., 2007)(Ng et al., 2012)(Lotfi et al., 2015)(Han et al., 2017). In AIREBO potential, the potential energy (E) of an atomic configuration consists of three terms:

$$E = \frac{1}{2} \sum_i \sum_{j \neq i} [E_{ij}^{REBO} + E_{ij}^{LJ} + \sum_{k \neq i, j} \sum_{l \neq i, j, k} E_{kijl}^{TORSION}], \quad (4.1)$$

where E^{REBO} = REBO energy, this term in AIREBO potential gives the model its reactive capabilities only describes the short-ranged C-C, C-H, and H-H interaction ($r < 2 \text{ \AA}$). Where, E^{LJ} = Lenard-Jones energy, this term adds non-bonded interactions and $E^{TORSION}$ = Torsion energy; it describes the dihedral angle preference in hydrocarbon configurations.

$$E_{ij}^{LJ} = 4\epsilon_{ij} \left[\left(\frac{\sigma_{ij}}{r} \right)^{12} - \left(\frac{\sigma_{ij}}{r} \right)^6 \right], \quad (4.2)$$

where the ij indices indicate the chemical species (C or H) of two interacting atoms, ϵ_{ij} and σ_{ij} are the well-depth energy and the distance at which pair interaction energy goes zero, respectively.

Initially, GNS modeled using the modeling software are not in their minimum energy configuration. A minimization and equilibration of the GNS are performed to obtain a relaxed GNS. All simulations are performed with a time step size of 0.001 ps to encapsulate the accurate hydrogen adsorption dynamics. Firstly, the optimized GNS structure is obtained by minimizing the modeled system's energy, using the conjugate gradient method. The modeled structure initially contains some pre-stored stress. To achieve a stress-free GNS, a relaxation process is conducted at a low temperature (77 K) for 250 ps, using the NVT and NPT ensembles sequentially. After that, H_2 molecules are added to the simulation box, and further simulations are performed using the NPT

ensemble to achieve the adsorption capacity at the desired pressure and temperature. After that, an equilibration run of 1 ns is conducted under the isothermal and isobaric conditions. The above simulation steps are performed multiple times for each pressure and temperature.

4.2.1 Providing strain:

After obtaining stress-free/relaxed GNS, the armchair direction of the GNS is stretched. One end of the sheet (left side) is fixed, and the other end (right side) is free. Then, the free edge of the GNS is displaced along the direction perpendicular to the edge using move command in LAMMPS. Initially, C-C bond length is 1.42 Å, and the maximum elongation of C-C bond in this study is set to the bond length of 1.562 Å. This change in bond length corresponds to a limited strain of 10% to observe the adsorption trend while avoiding the failure of the sheet. The strain (e) is calculated as,

$$e = \frac{\text{Change in length}}{\text{Initial length}} = \frac{l_f - l_o}{l_o}, \quad (4.3)$$

where l_f = final C-C bond length in GNS, l_o = initial C-C bond length.

4.2.2 Introducing defects in GNS:

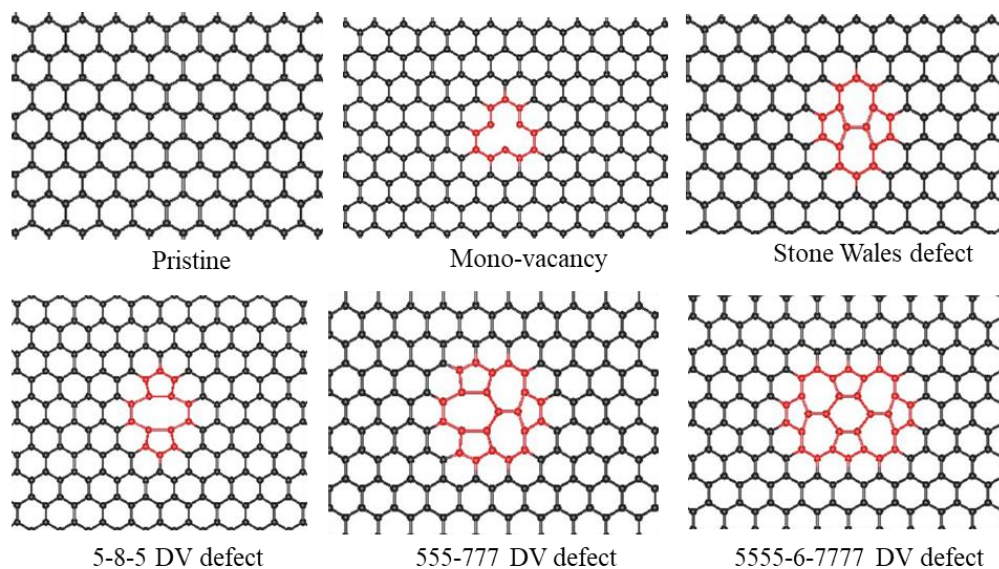


Figure 4.1 Different point defects

The particle irradiation process of solids with energetic particles such as electrons or ions to create atomic defects in the material and alter their properties is a well-known technique (Banhart et al., 2011b)(Deretzis et al., 2012). This work considers the different types of point vacancy defects such as monovacancies, Stone Wales (SW) defect, and double vacancies (DV) can be viewed as a special case of vacancy concentration in GNS. These defects often occur randomly during the synthesis of graphene. We intend to measure how vacancy; different types of vacancy concentration may influence the mechanical properties and hydrogen adsorption capability of GNS. The vacancy concentration (ρ) is calculated using the following relation (Kundalwal and Choyal, 2018b)(Kothari et al., 2018):

$$\rho = \frac{N_r}{N} \times 100, \quad (4.4)$$

where, N_r is the number of removed C atoms, and N is the total number of atoms in the pristine GNS. The adsorption capacity and adsorption energies are calculated using Equation 3.3 and 3.4, respectively.

We chose to model the GNS with dimensions $100 \times 100 \text{ \AA}^2$ and to create a vacancy defect, unless otherwise mentioned, the carbon atoms from the central segment of GNS are removed, as shown in Figure 4.1. The figure shows the pristine and different vacancy defects, such as MV, SW, and different types of DV defects, respectively. The MV defect is created when one C atom is removed from its lattice position. In SW defect, any one of the C-C bonds rotated by 90° , creating heptagon and pentagon rings. When two adjacent MV combines or two adjacent C atoms are removed simultaneously, a 5-8-5 DV defected GNS is obtained. Further, when the one side of the octagon formed in 5-8-5 is rotated by 90° then 555-777 DV defect is made, and in last, when the other side of the octagon is also turned by 90° then 5555-6-7777 DV defect is created.

4.3 Results and discussions

4.3.1 Effect of strain on H₂ adsorption:

The impact of strain on GNS for their ability to adsorb hydrogen is performed using MD simulations; strain is provided in a uniaxial armchair direction. Figure 4.2 represents the variation of wt.% with strain. To calculate the strain, we have used the above standard

Equation 4.3. Once the required strain is provided, the system is equilibrated at the desired temperature and pressure. Then the wt.% is calculated using the method provided in section 3.4 at 77 K temperature and 10 bar pressure. Figure 4.2 depicts an increase in the wt.% of the strained pristine GNS from 5.42 to 6.28 with increasing strain. Straining GNS increases the chemical activity by reducing the potential barrier and makes them more chemically active for hydrogen adsorption (Surya et al., 2012). Simultaneously, the C-C bond length also increases, due to which the total surface area increases and physisorption is a surface phenomenon, so the wt.% increases with strain increment.

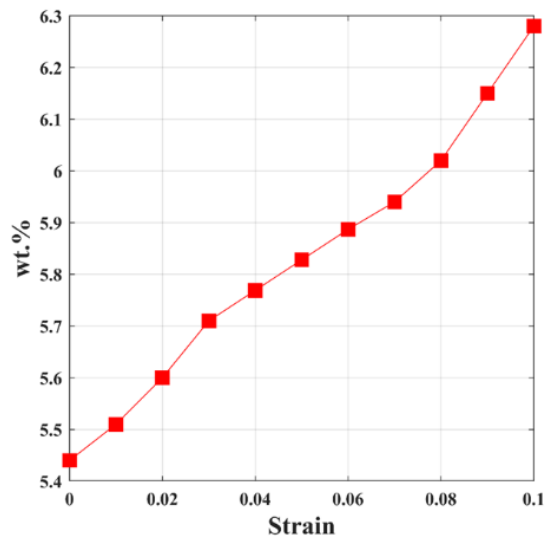


Figure 4.2 Variation of wt.% of hydrogen adsorption on graphene with strain at 77 K and 10 bar.

4.3.2 Effect of defects on H₂ adsorption:

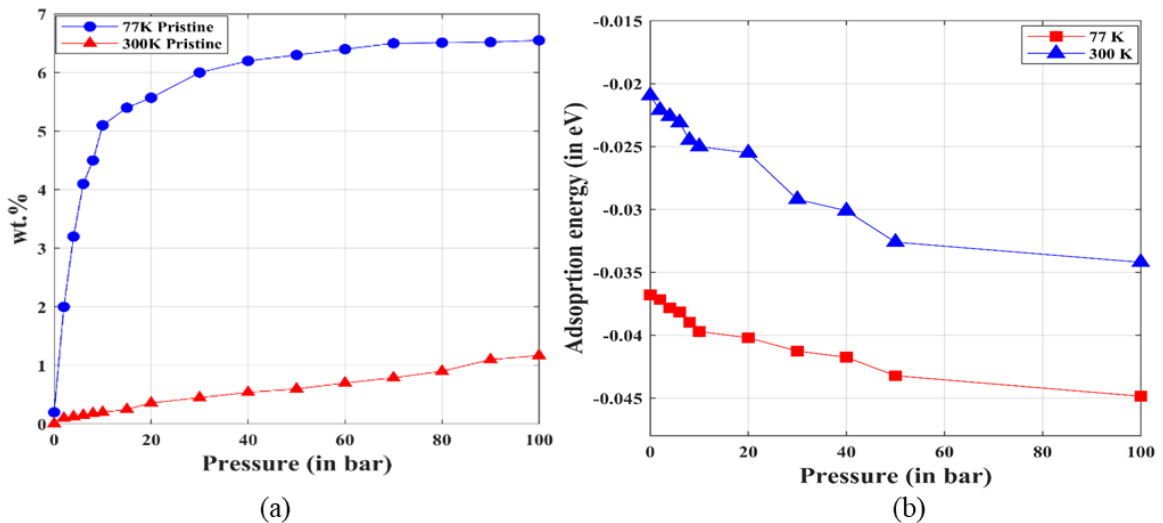


Figure 4.3 (a) Adsorption isotherm and (b) average adsorption energy vs pressure for pristine graphene.

In this section, the impact of different point defects on the hydrogen adsorption capacity is discussed. The presence of vacancies causes stress in the system and alter the chemical reactivity (Pablo A Denis and Iribarne, 2013). Figure 4.3 (a) represents the variation of gravimetric density with pressure for pristine GNS at a constant temperature. The wt.% increases with an increase in pressure at a temperature of 77 K, and at higher pressures (after 50 bar), the wt% becomes invariable with the increase in pressure. So, it is concluded that the saturation state had achieved at the given temperature. Figure 4.3 (b) represents the variation of adsorption energy with pressure at constant temperature. From the respective figure we can conclude that, at lower temperature the magnitude of adsorption energy is more as compare to at higher temperature. If magnitude of adsorption energy is more the stronger is the interaction between the interacting elements and the wt.% is more at lower temperature. From the respective figure, it is concluded that the increase in the magnitude of the adsorption energy shows the remarkable ability of GNS to hold more H₂ molecules with increasing pressure. With the pristine sheet, a maximum value of 6.55 wt.% of H₂ at 77 K temperature and 1.17 wt.% of H₂ at 300 K is achieved. The adsorption energy calculation of hydrogen molecule on the GNS is found to be -0.0402 eV at a temperature of 77 K (Yadav et al., 2014a)(Costanzo et al., 2012). And also, a 0.6 wt.% at 77 K and 1 bar pressure and 0.083 wt.% at 300 K and 1 bar pressure (Ma et al., 2009b) is achieved. At higher temperatures, molecules' kinetic energy increases, leading to the desorption of H₂ molecules; hence, at 300 K, a lower wt% is obtained.

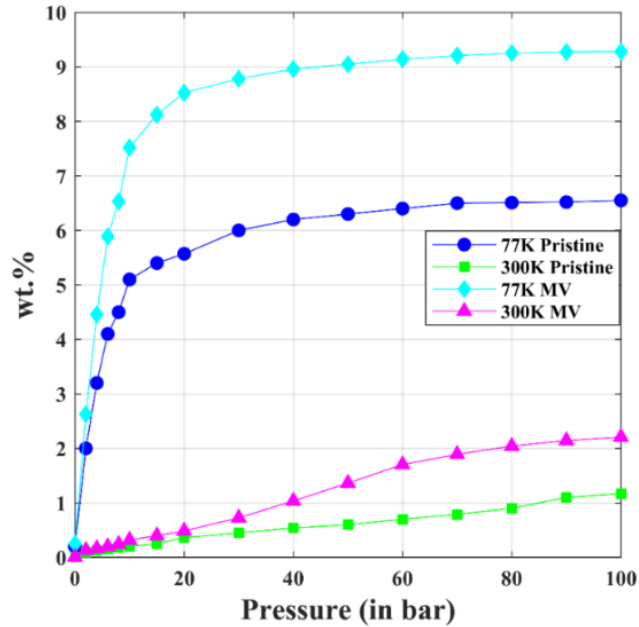


Figure 4.4 Comparison of MV-GNS hydrogen adsorption isotherms with P-GNS at 77 K and 300 K.

Figure 4.4 represents the comparison of the gravimetric density of the GNS containing 1% of MV concentration with the pristine GNS at various pressures and temperatures. It is observed that the wt.% of the GNS containing the MV concentration is more than pristine, and with increment in pressure, the wt.% increases. The GNS containing MV defects achieves a maximum value of 9.3 wt.% of H_2 at 77 K temperature and 2.208 wt.% of H_2 at 300 K at a constant pressure of 100 bar, and a minimum value of 0.25 wt.% at 77 K and 0.00625 wt.% at 300 K at 0 bar pressure. The adsorption energy of the hydrogen molecule adsorbed on GNS is found to be -0.3282 eV at a temperature of 77 K (Yadav et al., 2014a). With a 1% of MV concentration defect, the percentage rise in wt.% is $\approx 42\%$ compared to the pristine GNS at 77 K and 100 bar.

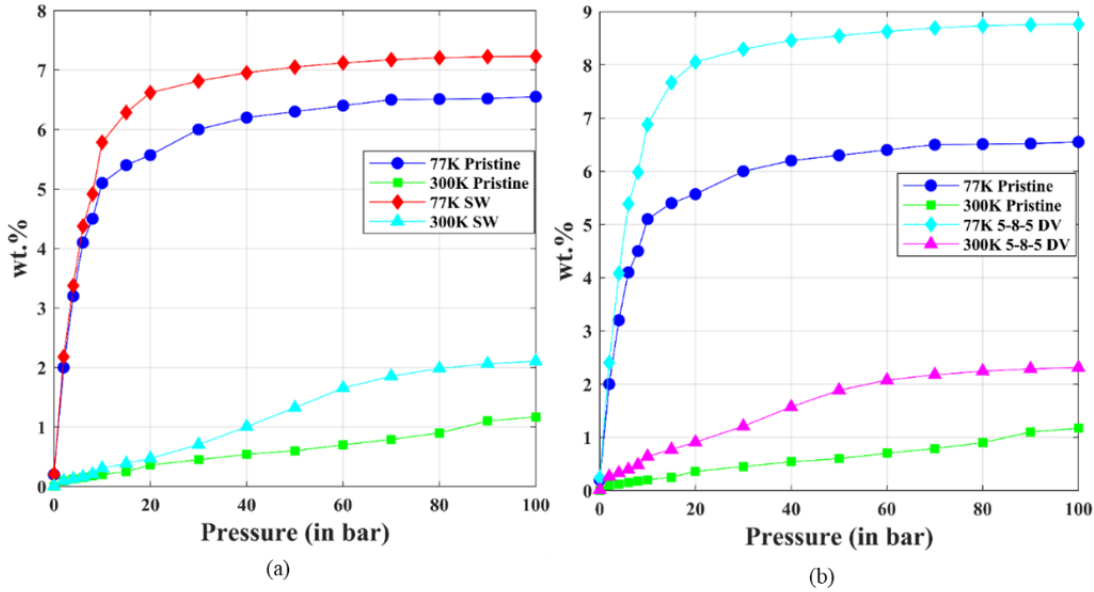


Figure 4.5 Comparison of (a) SW-GNS (b) 5-8-5 DV-GNS hydrogen adsorption isotherms with P-GNS 77 K and 300 K.

Figure 4.5 (a) represents the comparison of the gravimetric density of the GNS containing the 1% of SW concentration with the pristine GNS at different pressures and constant temperature. The figure depicts that the wt.% of the GNS having the SW defect is more than the pristine GNS. In the case of the GNS containing the SW defects, a maximum value of 7.23 wt.% of H_2 at 77 K and 2.1043 wt.% of H_2 at 300 K temperature is obtained, and a minimum value of 0.208 wt.% at 77 K and 0.00561 wt.% at 300 K at a pressure of 0 bar is obtained. The adsorption energy of hydrogen molecule on GNS with SW defect is found to be -0.04409 eV at a temperature of 77 K (Yadav et al., 2014a)(Costanzo et al., 2012). With a 1% of SW defect concentration, the percentage rise in wt.% is $\approx 10.4\%$ compared to the pristine GNS at 77 K and 100 bar. Figure 4.5 (b) represents the comparison of the gravimetric density of the GNS containing 1% concentration of 5-8-5 DV defect with the pristine sheet at different pressures and constant temperature. It is observed that the adsorption wt.% of H_2 molecules is more in 5-8-5 DV defect as compared to pristine. GNS containing the 5-8-5 DV defects can adsorb a maximum value of 8.763 wt.% of H_2 at 77 K and 2.3098 wt.% of H_2 at 300 K temperature and the minimum value of 0.234 wt.% at 77 K and 0.0085 wt.% at 300 K at a pressure of 0 bar. The adsorption energy of the H_2 molecule for adsorption on 5-8-5 DV GNS is -0.0956 eV, which is greater than the adsorption energy for pristine sheets. With a 1% concentration of 5-8-5 DV defect, the percentage rise in wt.% is $\approx 34\%$ compared to pristine at 77 K and 100 bar.

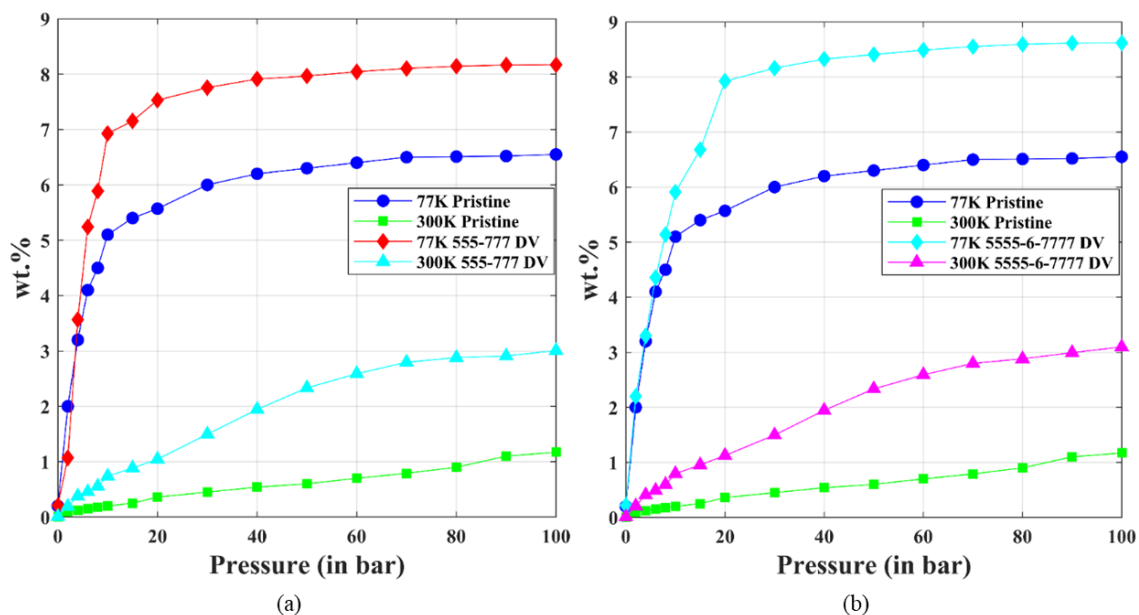


Figure 4.6 Comparison of (a) 555-777 DV-GNS (b) 5555-6-7777 DV-GNS hydrogen adsorption isotherms with P-GNS 77 K and 300 K.

Figure 4.6 (a) represents the comparison of the gravimetric density of GNS containing the 1% concentration of 555-777 DV defect with the pristine sheet at different pressures and constant temperature. The following figure depicts that the wt.% of adsorbed H_2 molecules is higher for the defected GNS compared to pristine. The GNS containing the 555-777 DV defects adsorbs a maximum value of 8.17 wt.% of H_2 at 77 K and 3.006 wt.% of H_2 at 300 K temperature, and a minimum value of 0.21 wt.% at 77 K and 0.00918 wt.% at 300 K at 0 bar pressure. The adsorption energy calculation of adsorbed H_2 molecule on 555-777 DV GNS is -0.07929 eV at a higher adsorption temperature than pristine GNS. With a 1% of 555-777 DV defect concentration, the percentage rise in wt.% is $\approx 25\%$ compared to pristine GNS at 77 K and 100 bar. Figure 4.6 (b) represents the comparison of the gravimetric density of the GNS containing the 1% concentration of 5555-6-7777 DV defect with the pristine sheet at different pressures and constant temperature. GNS having the 5555-6-7777 DV defects adsorbs a maximum value of 8.6205 wt.% of H_2 at 77 K and 3.096 wt.% of H_2 at 300 K temperature, and a minimum value of 0.218 wt.% at 77 K and 0.00991 wt.% at 300 K at 0 bar pressure. The adsorption energy of adsorbed hydrogen molecule on 5555-6-7777 DV GNS is -0.8403 eV, which is very much comparable to pristine GNS and a possible reason to get the more wt.% of hydrogen at a temperature of

77 K. With a 1% concentration of 5555-6-7777 DV defect, the percentage rise in wt.% is $\approx 31\%$ compared to pristine GNS at 77 K and 100 bar.

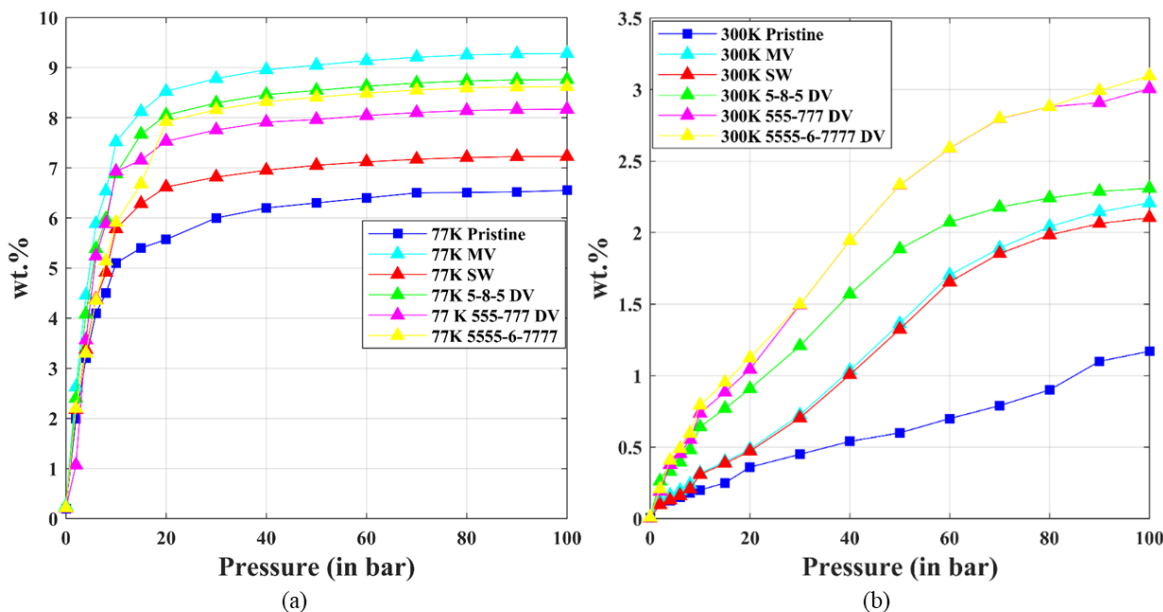


Figure 4.7 Variation of D-GNS hydrogen adsorption isotherms at (a) 77 K and (b) 300 K.

Figure 4.7 (a) represents the comparison of adsorption wt.% of pristine GNS to the GNS containing the different vacancy defects at a temperature of 77 K. From the following figure, it can be concluded that the defective GNS can adsorb more hydrogen molecules as compared to pristine GNS. The MV defected sheet shows the maximum H₂ wt.% compared to other defects, provided that the MV's activity towards the adsorption of H₂ is more compared to different types of possible point defects mentioned in the present work, and also the adsorption energy calculation suggests that the MV had a highest magnitude of adsorption energy as compare to the other possible defects. Figure 4.7 (b) represents the isotherm at 300 K, showing the comparison of the gravimetric density of GNS with various point defects to the pristine GNS. The following figure depicts that the GNS with the MVs and SW defects have a greater desorption ability than other possible defects. A maximum value of 1.17 wt.%, 2.2083 wt.%, 2.1043 wt.%, 2.3098 wt.%, 3.006 wt.%, and 3.096 wt.% is achieved at a pressure of 100 bar for pristine, MV defected, SW defected, 5-8-5 DV defected, 555-777 DV defected, and 5555-6-7777 DV defected sheet respectively.

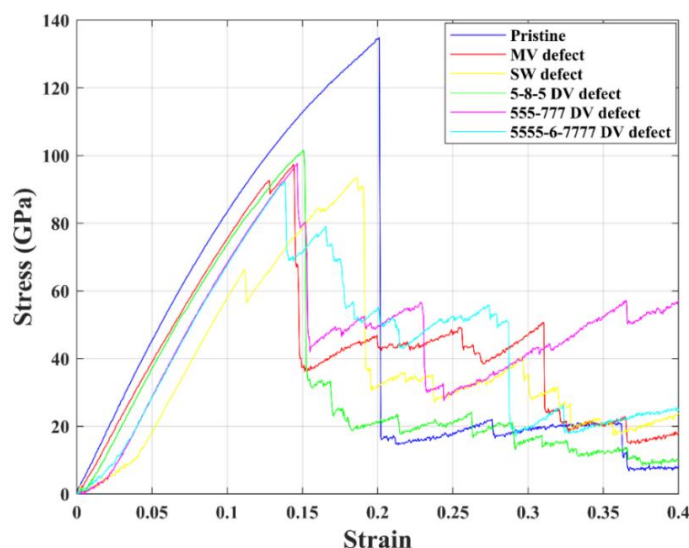


Figure 4.8 Strain vs stress curve of D-GNS at 300 K.

Table 4.1 Comparison of critical strain and stress of pristine graphene predicted by different methods.

Method	Critical strain	Critical stress (GPa)	Ref.
<i>Experimental</i>	25%	130 ± 10	(Lee et al., 2008b)
<i>Ab initio</i>	19.4%	110	(Liu et al., 2007)
<i>MD simulation</i>	23.3%	127	(Ansari et al., 2012)
<i>MD simulation</i>	20%	134.83	Present

Figure 4.8 represents the variation of stresses induced in the GNS with 1% defect with increasing strain. The following figure depicts the critical stress and critical strain value 134.83 GPa and 0.2, respectively, for the pristine GNS. Figure 4.8 shows that the defective sheet has a higher ability to adsorb the H_2 molecules than pristine GNS, but the critical stress and strain carrying capacity are reduced. By providing 1% concentration of defect, critical stress and strain value can be minimized by $\approx 30\%$ and $\approx 31\%$, respectively. If the concentration of defects increases further, the maximum strength carrying ability is going to decrease a lot. To verify the current MD simulations, the critical strain and stress values for pristine graphene reported by other researchers using different techniques were compared with our results, as summarised in Table 4.1. The comparison was found to be in good agreement.

4.4 Conclusion

In this study, the effect of strain and different vacancy defects on hydrogen adsorption capacity of GNS was investigated comprehensively using the MD simulation. An analysis of the impact of defects on maximum strength was studied. The interatomic interactions among C-C and H-H were modeled using the REBO potential and nonbonded interaction among C and H₂ molecule models using the LJ potential force field and they are in good agreement with the previous study. First, the effect of strain on the sheet was analyzed and found that the wt.% increases with the increase in strain up to 10%, and a maximum of 6.28 wt.% is achieved at 0.1 strain (5.4 wt.% in pristine), 10 bar and 77 K pressure and temperature respectively. The different types of vacancy defects have 9.3 wt.% in MV, 7.23 wt.% in SW, 8.763 wt.% in 5-8-5 DV, 8.17 wt.% 555-777, and 8.62 wt.% 5555-6-7777 DV at a 100 bar pressure and 77 K temperature while pristine GNS had a maximum of 6.55 wt.% at 100 bar and 77 K pressure and temperature, respectively. We can easily conclude that with the defects, the wt.% increases, and GNS with the MV defect can adsorb more H₂ compared to other possible point defects. We can also conclude that if defect concentration increases, the wt.% will increase, but at the same time, the strength analysis shows that the critical stress and critical strain decreases with defects, so we are not going beyond the 1% of defect concentration. From the isotherms, we can conclude that the wt.% increases with increment in pressure and reaches a saturation state at higher pressure. We can say that the maximum wt.% value went at a specified temperature. The present chapter offers a theoretical framework for predicting the hydrogen adsorption on GNS, considering the strain and defects at 77 K and 300 K temperatures and different pressures.

Chapter 5

Enhanced hydrogen storage in titanium decorated polycrystalline graphene

This chapter examines the hydrogen storage capabilities of Ti-PGs through MDS. It highlights the influence of grain boundaries, Ti atom concentration, and environmental conditions on hydrogen adsorption and desorption behaviors. The findings suggest that Ti-PGs present a promising avenue for efficient hydrogen storage, emphasizing the role of surface modification and atomic interactions in optimizing adsorption capacities.

5.1 Introduction

Pristine graphene sheets cannot bind sufficient hydrogen on their surface at ambient temperature due to low binding energy (Heine et al., 2004; Okamoto and Miyamoto, 2001; Tozzini and Pellegrini, 2011). Therefore, many theoretical and experimental studies have focused on increasing the hydrogen storage capacity of graphene. One of the most widely used methods is the functionalization of the surface of graphene, which leads to the tailoring of characteristics like the surface area, chemical reactivity, porosity, and interlayer spacing to enhance the adsorption capacity (Gangu et al., 2019; Jain and Kandasubramanian, 2020; Shiraz and Tavakoli, 2017; Szczeniak et al., 2017).

Experimental studies and computational simulations have provided extensive insights into the structural, mechanical, and adsorption properties of polycrystalline graphene (PGs) and its composites. Research has consistently shown that the presence of grain boundaries (GBs) in PGs impacts their mechanical properties significantly, reducing Young's modulus and fracture strength as the grain size decreases, while the electrical properties remain relatively unaffected (Chen et al., 2015; P. Y. Huang et al., 2011; Yazyev and Chen, 2014). Furthermore, the orientation of GBs plays a crucial role in the mechanical performance of materials such as polycrystalline carbon nanotubes, where transverse GBs

lead to a substantial reduction in strength (Alian et al., 2017c). The modification of PGs with dopants like boron and nitrogen or defects such as nanopores has been investigated, revealing that such modifications can influence tensile strength and ultimate failure strain, with nitrogen doping having a more pronounced effect than boron (Izadifar et al., 2018, 2017).

In terms of hydrogen storage, the adsorption behavior on PG surfaces and the effect of titanium (Ti) decoration have been key areas of research. Studies indicate that nanostructured graphene and Ti-decorated graphene provide enhanced active sites for hydrogen adsorption, with the latter showing significant promise for high-capacity hydrogen storage. First-principles calculations and DFT simulations have demonstrated the potential of Ti-decorated graphene and its analogs to achieve stable, high-capacity hydrogen storage at room temperature, with desorption occurring at elevated temperatures. The adsorption capacity is further influenced by external factors such as electric fields, which can enhance the interaction between Ti and hydrogen molecules (Bhattacharya et al., 2009; Lebon et al., 2015a; Lee et al., 2013; Park et al., 2010b; Rafique et al., 2019; Wang et al., 2013; Yuan et al., 2018; Zhang et al., 2014).

The literature on the fabrication of large-area graphene reveals that the GBs are wide-ranging in them, owing to inherent issues with fabrication techniques, surface energy, impurities, etc. (Alian et al., 2017c; Cui et al., 2016b; Guo et al., 2018; Roh et al., 2021; Wei et al., 2021). To the best of our knowledge, there has been no single attempt to study the adsorption and desorption behavior of PGs and Ti-decorated PGs towards hydrogen storage using MDS. The present chapter focused on studying the adsorption and desorption behavior and showing a novel pathway to enhance the hydrogen adsorption capability of PGs by decorating Ti atoms via large-scale MDS. Fracture mechanics analysis of PGs and Ti-PGs is also carried out under uniaxial tensile loadings. The importance of the presence of inherent GBs and the domain sizes as well as the Ti atoms concentration, temperature, and pressure in determining the interactions between hydrogen gas and the graphene surface is considered. The isosteric enthalpy of adsorption for Ti-decorated PGs is also determined to analyze the mechanics of adsorption at different temperature ranges. The understanding of the interface properties between graphene, Ti, and H₂ molecule provides

a wide range of possibilities for the use of Ti–graphene-based structures as a potential material for efficient hydrogen storage systems.

5.2 Methodology

5.2.1 Modeling of Ti decorated PGs

Our simulations consist of PGs created from a unit cell of graphene using Voronoi tessellation and Delaunay triangulation techniques (Alian et al., 2017c), while also allowing the wrapping of edges of the sheets to create a square shaped PGs. Multiple PGs are created, with varying grain sizes calculated by $\sqrt{\frac{L^2}{N}}$ (Izadifar et al., 2018), where L is the length of the sheet and N is the number of grains.

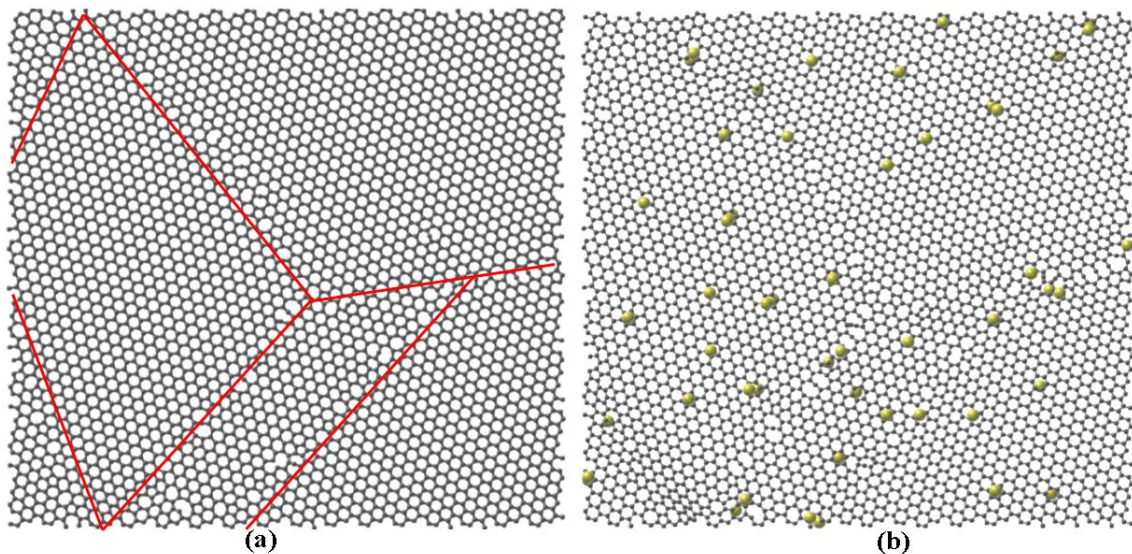


Figure 5.1 (a) Polycrystalline graphene sheet [red lines indicate the GBs], and (b) polycrystalline graphene sheet decorated with randomly distributed titanium atoms. [Yellow Ti atoms; and gray C atoms].

The misorientation angle of GBs varies during the synthesis of graphene; thus, misorientation angles were not controlled in this study, and randomly oriented PGs of various grain sizes were simulated. The PGs were then decorated with different concentrations of Ti atoms to study the doping effect on the strength under uniaxial tension and hydrogen adsorption capacities. Figure 5.1 shows the equilibrated structures of PG with a grain size of 4.47 nm and Ti-PGs with 1% Ti concentration.

MDS are performed on systems of PGs with and without decoration of Ti atoms for investigating the hydrogen adsorption capacity of PG systems. All MDS were conducted

via the LAMMPS (S Plimpton, 1995) software package based on classical molecular dynamics. To accurately perform MDS of hydrogen adsorption on PGs decorated with Ti atoms, the interatomic interactions of PGs atoms are described using the Tersoff potential (Tersoff, 1989b), which was applied successfully in previous studies (Kundalwal et al., 2020a, 2021). The interactions between carbon atoms of PGs and Ti atoms are described using the Lennard–Jones (LJ) 12-6 potential. In this study, the diatomic hydrogen molecule is considered as a single entity. The interatomic interactions between hydrogen molecules (H_2) and Ti-PGs are also described using the LJ potential, as follows:

$$u_{ij} = 4\varepsilon_{ij} \left[\left(\frac{\sigma_{ij}}{r} \right)^{12} - \left(\frac{\sigma_{ij}}{r} \right)^6 \right] \quad (5.1)$$

where u_{ij} is the pairwise interaction energy, and ε_{ij} and σ_{ij} are the well-depth energy and the distance at which the pair interaction energy goes to zero, respectively. The cut-off distance of 12 Å is chosen for LJ interactions.

Table 5.1 LJ interaction parameters for different atomic interactions.

Parameter	H₂-H₂	C-C	Ti-Ti
ε [kcal/mol]	0.067962	0.055641	0.5681
σ [nm]	0.296	0.340	0.268

Table 5.1 describes the LJ potential parameters used in this study (Chu et al., 2011; Cracknell, 2001; Faria et al., 2020; Zhen and Davies, 1983). The LJ parameters between different species are obtained using Lorentz–Berthelot mixing rules:

$$\varepsilon_{ij} = \sqrt{\varepsilon_i \varepsilon_j} \quad ; \quad \sigma_{ij} = \frac{\sigma_i + \sigma_j}{2} \quad (5.2)$$

Tensile simulation tests on pristine graphene sheets in the armchair direction are performed. However, various factors like the strain rate, the direction of stress applied, and temperature influence the mechanical properties of graphene sheets; such effects are not considered for validation purposes. The tensile test simulation carried out herein provides the Young’s modulus, fracture strength, and fracture strain of 857.9 GPa, 162.8 GPa, and 0.189, respectively, which is in good agreement with the previous study (Yang et al., 2015). Thus, the above description of the interatomic potential is sufficient to proceed with the simulation of the Ti-PGs tensile test and hydrogen adsorption capacity investigation.

PGs with a grain size of 1 to 8 nm are modeled, and then these sheets are decorated with Ti atoms with a concentration up to 2.0%. These concentrations are a measure of the coverage of the Ti atoms on PGs. These sizes are chosen to optimize the computational time required with a large number of atoms in the system under consideration. Ti atoms are randomly placed above and below the PGs in the simulation box, with the Ti concentration up to 2.0%. The amount of Ti atoms to spread around the PGs depends on the adatoms concentration, given by

$$\rho(\%) = \frac{\text{Number of titanium atoms}}{\text{Number of carbon atoms in the PGs}} \times 100 \quad (5.3)$$

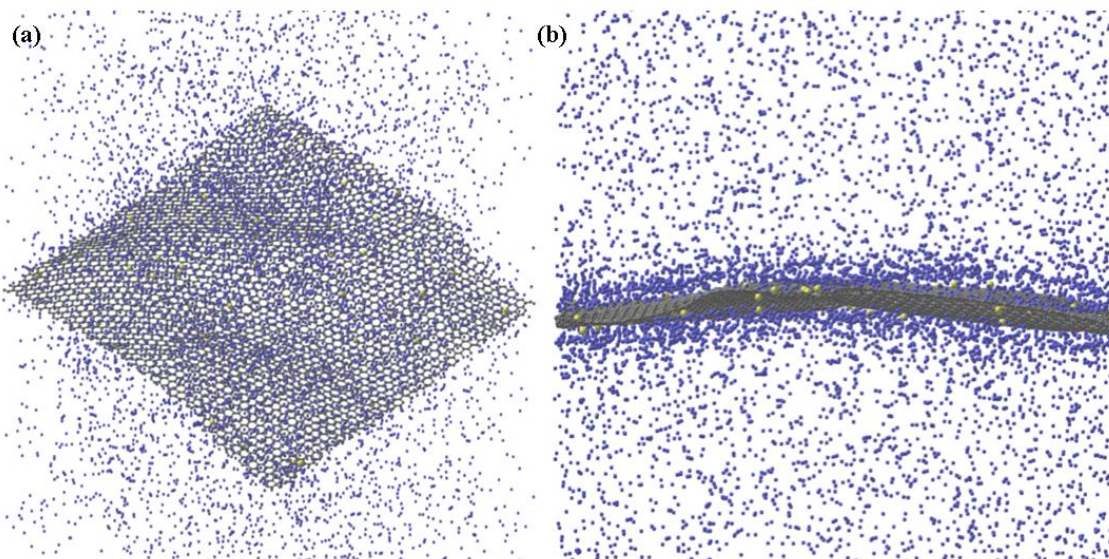


Figure 5.2 System configuration of titanium-decorated polycrystalline graphene sheets: (a) isometric view and (b) side view. [Blue hydrogen atoms; yellow Ti atoms; and gray C atoms].

Figure 5.2 shows the simulation box with hydrogen molecules surrounding the Ti-decorated PGs. For simulating monolayer sheets, the PGs are placed in a box with a periodic boundary condition in all directions. The out-of-plane directions of Ti-PGs are kept large enough to avoid the interlayer interactions. A timestep of 0.5 fs was adopted, which is small enough to encapsulate accurate fracture and adsorption dynamics. The conjugate gradient method was applied with an energy convergence of 10^{-10} to obtain energy-minimized systems. For a stress-free sheet, an equilibration run for 250 ps is performed under an isothermal and isobaric ensemble.

Tensile tests are performed at a temperature of 300K and pressure of 1 bar, where the Nosé–Hoover thermostat and barostat control the temperature and pressure of the system, respectively. During the tensile test, a strain rate of 10^{-7} Å/fs was applied, and the stresses on the atomic structures were recorded every few timesteps. Atomic stresses on the sheet were estimated on the basis of the virial theorem. The average virial stress ($\sigma_{\alpha\beta}$) over volume Ω with a total number of atoms n^A is described by

$$\sigma_{\alpha\beta} = \frac{1}{\Omega} \left(\frac{1}{2} \sum_{i=1}^{n^A} \sum_{\substack{j=1 \\ j \neq i}}^{n^A} \mathbf{r}_{ij\alpha} \otimes \mathbf{f}_{ij\beta} - \sum_{i=1}^{n^A} m_i \dot{\mathbf{u}}_{i\alpha} \otimes \dot{\mathbf{u}}_{i\beta} \right) \quad (5.4)$$

where m_i is the mass of atom i ; $\mathbf{r}_{ij\alpha}$ is the position vector in α direction, $\mathbf{f}_{ij\beta}$ is the force vector in β direction, between atoms i and j . $\dot{\mathbf{u}}_{i\alpha}$ and $\dot{\mathbf{u}}_{i\beta}$ are the velocity vectors of atom i , in α and β directions respectively. The engineering strain is used for measuring deformation described by $\varepsilon = \frac{\Delta L}{L_0}$, where ΔL defines the change in the length of the sheet upon deformation and L_0 is the original length of the sheet.

5.2.2 GCMC technique

For hydrogen adsorption, grand canonical Monte Carlo (GCMC) simulations with an isothermal ensemble are performed, where hydrogen molecules are added into the system randomly at different locations in the simulation box. In GCMC simulations, the input parameters like the temperature and chemical potential (or pressure) of a fictitious gas reservoir are the known parameters, and the amount of gas in the system can be calculated. The amount of gas present in the simulation box is in equilibrium with the fictitious gas reservoir when its temperature and chemical potential (or pressure) become equal. The three operations in a GCMC simulation, such as insertion, deletion, and displacements, are performed with equal probabilities randomly. Figure 5.3 shows the steps involved in a typical Monte Carlo (MC) simulation where the acceptance and rejection of a random move is defined. The potential energy U of the system at the initial atomic configuration i is evaluated. Then, a random move is applied to the atoms, which corresponds to $i + 1$. If the energy of the system after this move is reduced, i.e. $U_{i+1} < U_i$, then the move is accepted. The probability of adding the new configuration to the trajectory after every MC move is given by $p_{i+1} = \exp\left(-\frac{\Delta U}{k_B T}\right)$, where k_B is the Boltzmann constant. If $U_{i+1} > U_i$, then a

random number ε is generated, where $0 < \varepsilon < 1$. Now, if $\varepsilon < p_{i+1}$, then the move is accepted; otherwise, the move is rejected. The amount of MC cycles is defined while running the simulations. The accepted moves are added to the trajectory, and the rejected moves are traced back to the previous state, and then they are also added to the trajectory, i.e., the same trajectory is added twice to obtain the correct probability. Finally, ensemble averages are calculated for every MC move.

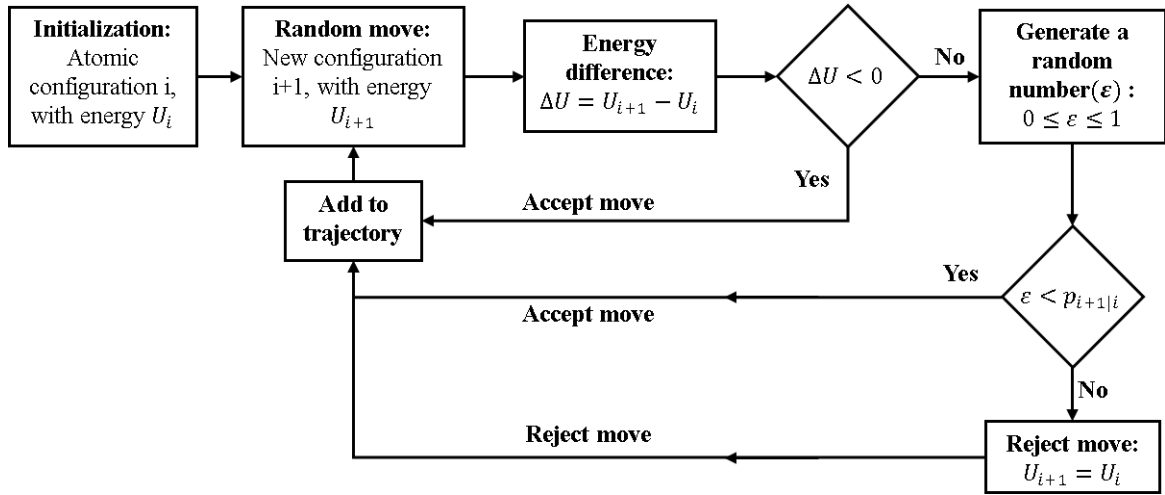


Figure 5.3 Flow diagram of MC simulations.

After the GCMC run, a system equilibration is performed using the isothermal and isobaric ensemble at the desired temperature and pressure for 2 ns. During adsorption simulations, the wt.% at each pressure is calculated with the adsorbed amount of hydrogen molecules on the sheets, whereas, during desorption simulations, the sheet and hydrogen molecules system at 100 bar is brought down to the desired pressure to calculate the adsorption capacity. The hydrogen molecules that are adsorbed on the Ti-PGs are measured in wt.% calculated by

$$wt. \% = \frac{w_{H_2-adsorbed}}{w_{H_2-adsorbed} + w_C + w_{Ti}} \quad (5.5)$$

where $w_{H_2-adsorbed}$ is the weight of the adsorbed hydrogen molecule, w_C and w_{Ti} are the weight of the carbon and Ti atoms present in the Ti-PGs, respectively. The number of adsorbed hydrogen molecules on the sheet is estimated using the potential energy distribution (PED) of atoms (Luhadiya et al., 2021a).

5.2.3 Isotheric enthalpy

Hydrogen adsorption simulations are performed on Ti-PGs of different adatom concentrations at different temperatures and pressures ranging from 77–300 K and 0–100 bar, respectively. Adsorption isotherms at temperatures of 77 K, 97 K, 280 K, and 300 K are studied up to 100 bar pressure to calculate the isotheric enthalpy of adsorption (ΔH_{ads}). The Ti-PGs–H₂ interaction energy at a particular temperature is typically calculated from at least two adsorption isotherms obtained at very close temperatures (i.e., with a maximum difference of 20 K). The adsorption isotherms data from the MDS are fitted with the Toth isotherm (Tóth, 2000). Toth is an empirical model commonly used to describe the adsorbate adsorbent interactions for hydrogen adsorption with graphene (Luhadiya et al., 2021a). The amount of adsorbed quantity using the Toth model is calculated by

$$wt. = \frac{wt.m.K.p}{(1+(Kp)^n)^{1/n}}, \quad (5.6)$$

where $wt.m$ is the constant reflecting the maximum adsorption capacity, K is the Toth constant representing the affinity of the adsorbent for the adsorbate, and n is the heterogeneity factor. The isotheric enthalpy of adsorption, ΔH_{ads} , is given by

$$\Delta H_{ads} = -RT^2 \left(\frac{\partial(\ln p)}{\partial T} \right)_{wt.i}. \quad (5.7)$$

The above equation is known as the Clausius–Clapeyron equation, where R is the universal gas constant, T is the temperature at which enthalpy is calculated, and p is the pressure at the same adsorbed quantity ($wt.\%$) for different isotherms (i.e., isotheric pressures). To determine ΔH_{ads} , $\ln(p)$ against $wt.\%$ is plotted using the values from the modeled Toth isotherms at two close temperatures. The isotheric pressures are calculated from these plots and then, using Equation 5.7, the enthalpy of adsorption is calculated.

5.3 Results and discussion

Comprehensive MD simulations are carried out to study the effect of GBs and Ti decoration on PGs' hydrogen storage capacity. Adsorption and desorption simulations are performed on PGs and Ti-PGs with varying grain sizes and adatom concentrations in this section. Also, the simulations are performed at high to low pressures and temperatures, enabling deep insight into the adsorption mechanics. The addition of Ti atoms on the PGs

surface may produce a weak and unstable sheet. So firstly, PGs and Ti-PGs with varying concentrations and grain sizes are strained under tensile load until they fracture. Then, hybrid NVT-GCMC simulations are performed for investigating the hydrogen adsorption at different temperatures and pressures to obtain adsorption isotherms. The isosteric enthalpy of adsorption is determined at 77 K and 300 K using the isosteric pressures from the adsorption isotherms.

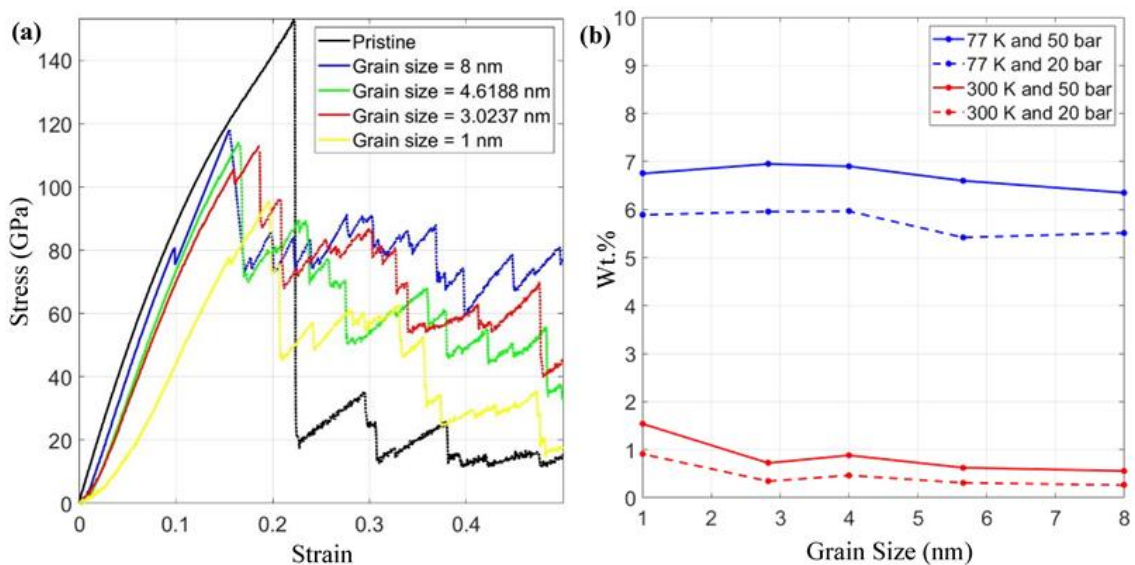


Figure 5.4 (a) Uniaxial tensile test of PGs for different grain sizes and (b) hydrogen adsorption capacity of PGs with varying grain sizes at different temperatures and pressures.

Figure 5.4 (a) shows the uniaxial tensile test of PGs with varying grain sizes at a temperature of 300 K. It can be observed that the fracture strength of PGs reduces as the grain size reduces, and a strength reduction of $\sim 38\%$ is observed from the pristine graphene at a grain size of 1 nm. The fracture strain of PGs increases with decreasing grain size; however, this value is still less than the pristine graphene, which is in good agreement with previous results [56]. Under the application of tensile loads, strained pristine sheets tend to adsorb slightly more hydrogen due to an increase in surface area and strong binding of stretched carbon atoms [40]. As evident from Figure 5.4 (a), PGs fracture at lower strain than pristine thus strained PGs will not contribute significantly towards the hydrogen adsorption. The hydrogen adsorption capacity of PGs is also studied, as shown in Figure 5.4 (b) at 77 K and 300 K, and pressures of 20 bar and 50 bar. The gravimetric density of the PGs at 77 K shows a small increase with decreasing grain size for both pressure

conditions. Also, at 300 K, the wt.% shows a small increment with decreasing grain size. Adsorption simulation of PGs at the cryogenic temperature and pressures is performed to observe significant changes. The PGs with a 1 nm grain size at 300 K and 50 bar pressure show ~57% higher gravimetric density than the pristine sheet at the same temperature and pressure as found in an existing study (Luhadiya et al., 2021a). Compared to the pristine sheet, the PGs show an increase in gravimetric density and a reduction in mechanical strength, but the strength of the PGs is still higher than most materials. So, PGs with a grain size of 1nm are used further in this study as the basis for further improving the hydrogen adsorption capacity.

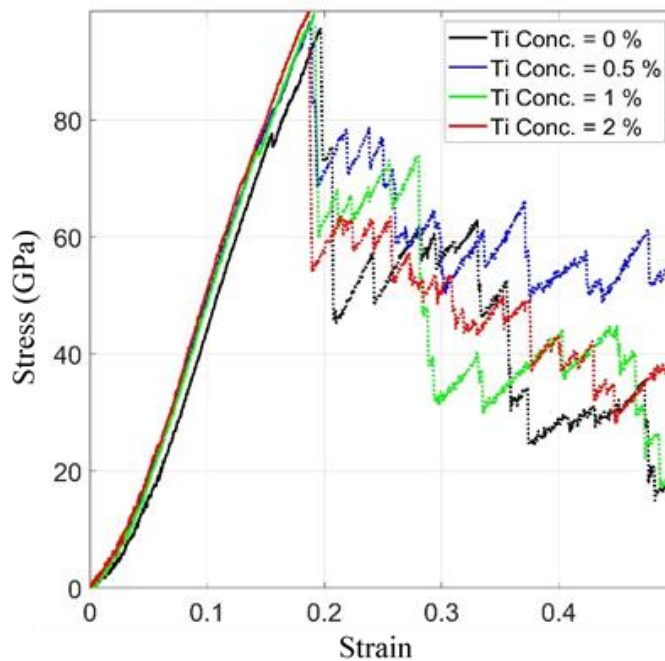


Figure 5.5 The stress–strain curves of titanium-decorated PGs (1 nm grain size) for different titanium concentrations.

Tensile tests are performed on functionalized PGs with a grain size of 1 nm and decorated with Ti atoms ranging from 0.5% to 2.0%. Figure 5.5 shows the stress–strain curves of the Ti-PGs with varying Ti concentrations. It can be observed from Figure 5.5 that the concentration of Ti adatoms does not alter the PGs’ mechanical properties. A small, insignificant increase in strength and decrease in strain is observed with Ti-decorated PGs as compared to non-decorated sheet. Thus, our findings indicate that Ti adatoms have no

adverse effect on the mechanical properties of PGs. The fracture mechanics of the PGs is also studied under tensile tests as shown in Figure 5.6.

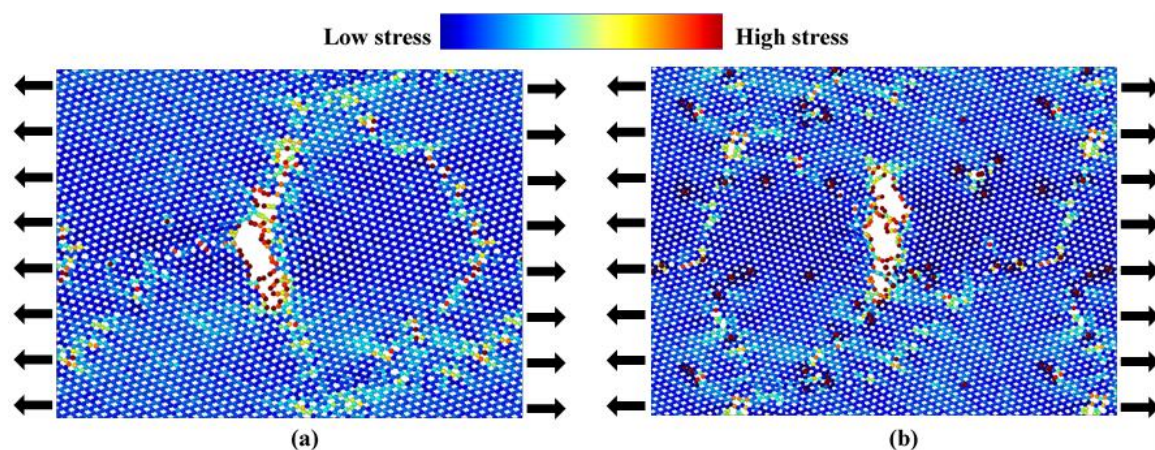


Figure 5.6 Fracture of (a) polycrystalline graphene and (b) Ti-decorated polycrystalline graphene. Color coding shows the intensity of the stress. [Magenta Ti atoms].

Figure 5.6 (a) and (b) show the fracture of PGs with 1 nm grain size and Ti-PGs with 1 nm grain size (with 1% Ti concentration), respectively. It is observed that the GBs of the sheets are under more stress when the deformation is applied in the x-direction as compared to the inner part of the grain. Then, at a specific strain, a crack initiates almost perpendicular to the loading direction at the grain boundary and then propagates along the grain boundary; subsequently, the sheet ruptures along the armchair or zigzag path, keeping the crack almost perpendicular to the loading direction. It is noted that the Ti-decorated PGs also demonstrate similar fracture mechanics. Thus, this confirms our prediction that the Ti decoration has little to no effect on the mechanical properties of Ti-PGs. In PGs, GBs are a region containing multiple types of defects like 5-, 7-, 8-, and 9-membered rings, vacancies etc., thus possibly demonstrating reduced strength compared to the inner pristine part of the grain. Also, the GBs with an orientation perpendicular to the direction of the load bear more load than other GBs and are more prone to crack initiation.

The hydrogen adsorption capacity of PGs with 1 nm grain size decorated with varied concentrations of Ti atoms is determined using MDS. The hydrogen adsorption–desorption capacity of Ti-PGs is demonstrated in Figure 5.7 (a) and (b) at 77 K and 300 K, respectively. The hydrogen adsorption capacity of Ti-PGs at 20, 50, and 100 bar is calculated for different Ti concentrations. The desorption capacity is obtained at 20 and 50

bar after equilibrating the system at 100 bar and then reducing to the desired pressure. It can be seen from Figure 5.7 (a) that the hydrogen adsorption capacity increases with the increase in Ti concentration up to 1.5%, and then decreases at 2% Ti concentration at 20, 50, and 100 bar pressures. A maximum adsorption capacity of 10.8 wt.% is achieved at 100 bar and 1.5% Ti concentration.

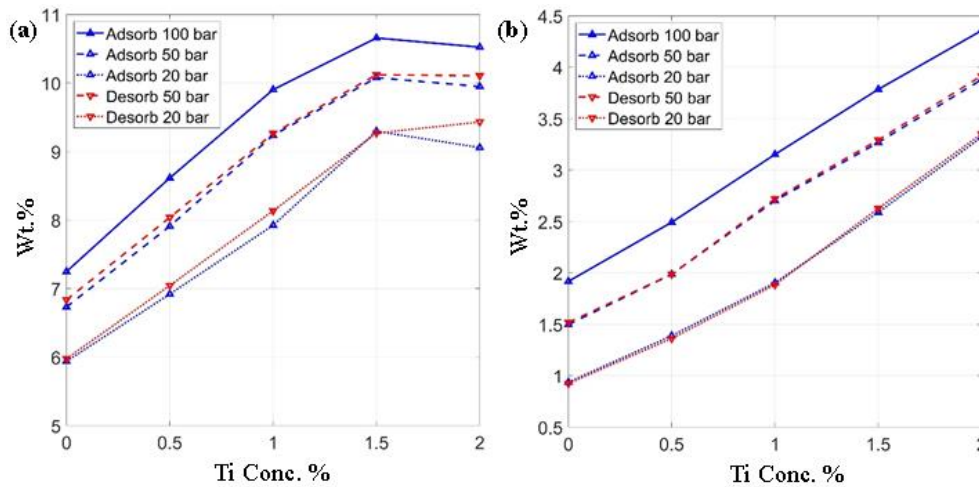


Figure 5.7 Hydrogen adsorption and desorption capacity of Ti-PGs with 1 nm grain size at varying Titanium concentrations at various pressures: (a) 77 K, and (b) 300 K temperatures.

Titanium adatom preferably attaches to the most active sites, and as the Ti concentration increases, the adatoms begin to agglomerate around these sites; thus, the reduction in hydrogen adsorption capacity at 2.0 % Ti concentration and 77 K might be owed to (i) the decrease in the number of accessible Ti atoms for H₂ molecules as well as (ii) the increase in net mass with increasing Ti concentration. The desorption curves follow a path similar to the adsorption curves, indicating a physisorbed state of H₂ molecules, but a lesser amount of hydrogen is released at 2% Ti concentration during the desorption with respect to the first adsorption, showing a stronger attraction of H₂ molecules to the Ti-PGs. At 300 K, there is a linear increase in the hydrogen adsorption capacity with increasing Ti concentration, as shown in Figure 5.7 (b). A maximum H₂ adsorption capacity of 4.4 wt.% is achieved at 2% Ti concentration and 100 bar pressure. It is observed that there is a linear increase in adsorption capacities and the desorption curve at the temperature of 300 K, and pressures of 50 and 20 bar follow a path similar to the adsorption curves; thus, it indicates the physisorption of H₂ molecules. A high temperature of 300 K excites the Ti atoms and H₂ molecules with high velocities, hindering the agglomeration of Ti atoms and reducing

the H₂ adsorption capacity of the Ti-PGs. The Ti-PGs show a higher adsorption capacity as compared to pristine sheets [54] at the same atmospheric conditions. The high adsorption capacity is due to the Kubas interaction (Hoang and Antonelli, 2009; Skipper et al., 2012). The σ bonding orbital of the H₂ molecule donates electron density to empty d-orbitals of Ti atoms with simultaneous π -back donations from the filled Ti d-orbital to the antibonding orbital of H₂ molecules. The respective loss and gain of electron density from bonding and antibonding orbitals result in elongation of the H₂ bonds, which reduces the interatomic repulsions and increases the adsorption capacity. Also, the carbon atoms neighboring the Ti adatoms tend to be more active for H₂ molecules adsorption. As discussed earlier, 1% Ti decoration does not lead to Ti atom agglomeration; therefore, Ti-PGs with 1% Ti concentrations will be used in further simulations.

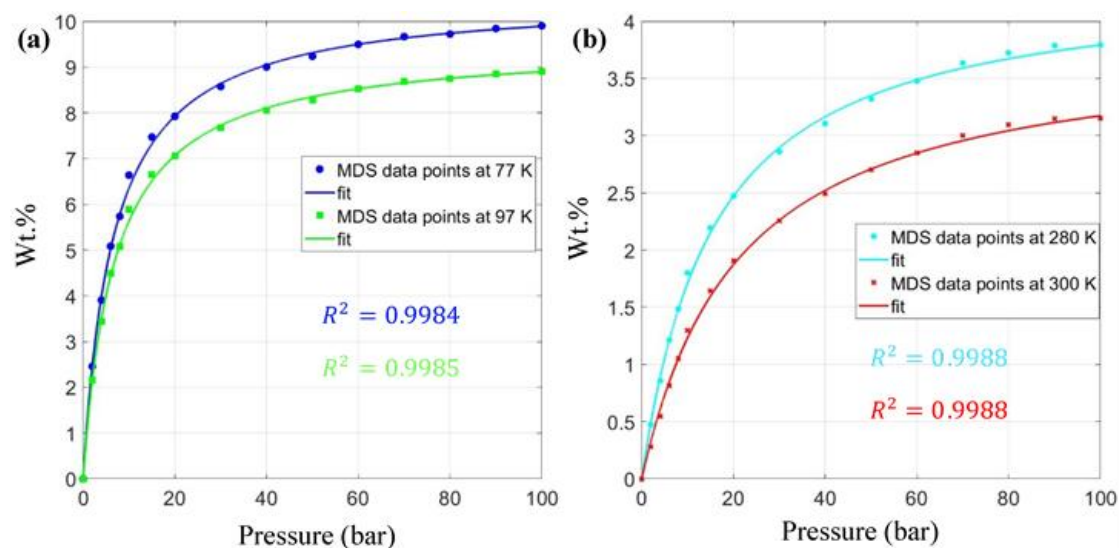


Figure 5.8 Hydrogen adsorption isotherms of Ti-PGs with 1% Ti concentration at (a) low temperatures (77 K and 97 K), and (b) high temperatures (280 K and 300 K). MDS data points are fitted with Toth isotherm model.

Using MDS, the adsorption isotherms of H₂ molecules at temperatures of 77 K, 97 K, 280 K, and 300 K in the pressure range of 0–100 bar are demonstrated in Figure 5.8 (a) and 8(b) for Ti-PGs with 1 nm grain size and 1% Ti concentration. As discussed in the earlier section, the isosteric enthalpy of adsorption is calculated using two isotherms with a temperature difference ≤ 20 K. The data points from MDS are fitted with the Toth isotherm model using Equation 5.6. A visual inspection and correlation coefficient (R^2) is

used for the accuracy of the fit. All the fitted curves are in excellent agreement with the MDS data points, as shown in Figure 5.8.

It can be observed from Figure 5.8 (a) that the H₂ adsorption capacities of Ti-PGs (with 1% Ti and 1 nm grain size) increase linearly at the start and then start to saturate between 40–50 bar pressure. The maximum adsorption capacities at 77 K and 97 K are 9.9 wt.% and 8.8 wt.%, respectively, at 100 bar pressure. Compared to the pristine graphene sheet at 77 K and 100 bar [54], a 46.67% increase in gravimetric density is observed. As discussed earlier, the desorption curves for Ti-PGs with 1 nm grain size and 1% Ti concentration follow a path similar to the adsorption curves; thus, the usable hydrogen, i.e., the hydrogen released (at 1 bar and 77 K) is ~55% more compared to the pristine sheet. The H₂ adsorption isotherms of Ti-PGs (with 1nm grain size and 1% Ti concentration) at 280 K and 300 K are depicted in Figure 5.8 (b). The adsorption capacity at these temperatures also follows a very short linear path. The gravimetric densities of these sheets are 3.8 wt.% and 3.2 wt.% at 280 K and 300 K, respectively, at 100 bar. The H₂ adsorption capacities of these sheets are ~4 times higher than the pristine graphene sheets [54]. The usable hydrogen is ~2.5 times higher than the pristine graphene sheets at 1 bar and 300 K. The H₂ adsorption capacity of Ti-PGs at 100 bar and 77 K is ~3 times higher as compared to 100 bar and 300 K. This is due to the higher kinetic energy of H₂ molecules at 300 K, which causes them to detach from the surface of Ti-PGs.

In order to study the energetics of H₂ adsorption on Ti-PGs, the isotherm obtained at low temperatures (77 K and 97 K) and high temperatures (280 K and 300 K) is used. The isosteric enthalpy of adsorption is determined using Equation 5.7, where the natural log of pressures at specified wt.% is plotted with the respective wt.% as shown in Figure 5.9 (a) and (b). Generally, the curve becomes linear over a wide range for gases with a low attraction to the adsorbent. The plot of the function $\ln p$ vs. wt.% is curved and diverging, as depicted in Figure 5.9. Also, curves are an indication of complex adsorption phenomenon with heterogenous surface sites, indicating a strong attraction of H₂ molecules on Ti-PGs. Thus, a Toth isotherm fitting for the MDS data points is required to approximate the curve. The vertical lines are isosteric lines in Figure 5.9, which indicate the logarithmic pressure values at constant wt.%. Multiple pairs of logarithmic pressure values at the two

temperatures are noted at different wt.% in both Figure 5.9 (a) and (b). Ten data pairs are noted in both the figures to determine the adsorption enthalpy using Equation 5.7.

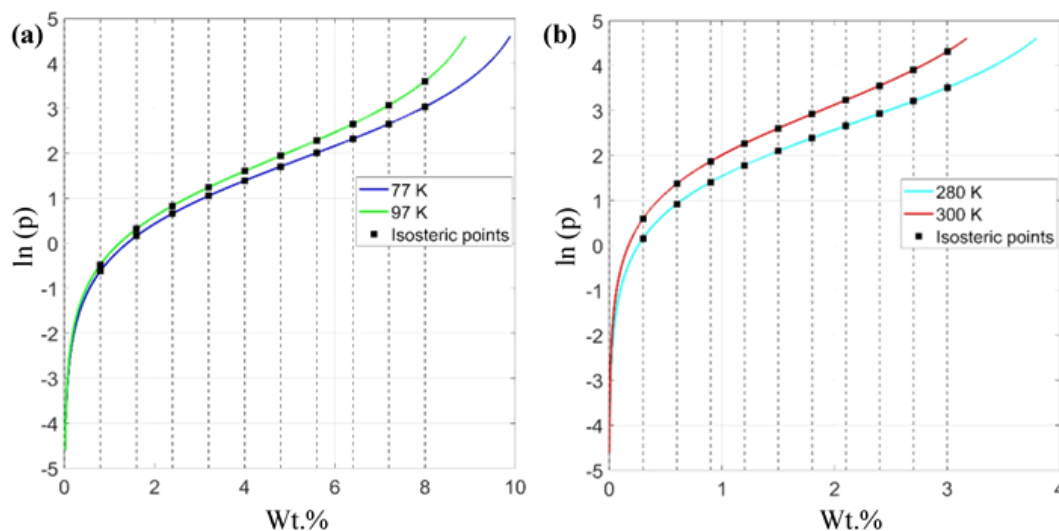


Figure 5.9 Plot of logarithmic pressure against wt.% obtained from the isotherms of Ti-PGs at (a) low temperatures (77 K and 97 K) and (b) high temperatures (280 K and 300 K). Dashed lines are isosteric lines, and square markers are isosteric logarithmic pressures at different wt.%

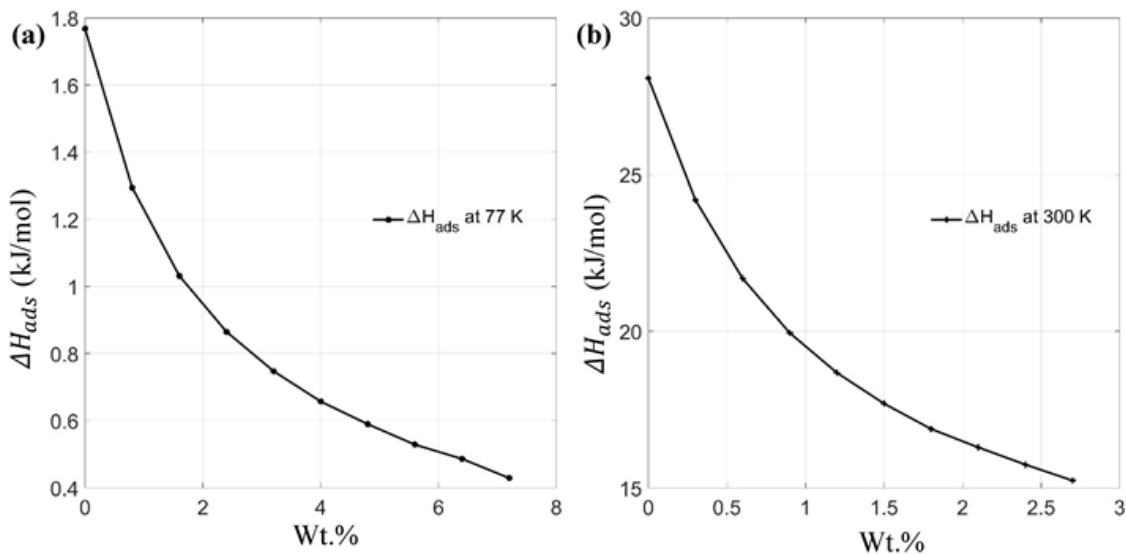


Figure 5.10 Isosteric enthalpy of adsorption of H_2 for Ti-PGs (a) 77 K and, (b) 300 K.

The isosteric enthalpy of adsorption (ΔH_{ads}) determines the amount of heat released or absorbed during the adsorption process, and most of the adsorption processes are exothermic. The variation of the enthalpy of adsorption (ΔH_{ads}) with wt.% is shown in Figure 5.10 (a) and (b) at 77 K and 300 K, respectively. Conventionally, it is expected that the absolute value of ΔH_{ads} will reduce as the adsorption on the adsorbent increases

because of the increasing intermolecular repulsions with increasing adsorbate density around the adsorbent surface, as evident from Figure 5.10. The parameter ΔH_{ads} indirectly determines the strength of the adsorbent to attract the adsorbate. At low pressures, the adsorbate prefers to occupy the adsorption sites with the highest affinity, and these sites are associated with higher absolute ΔH_{ads} values at low loadings. The ΔH_{ads} at the start of adsorption, i.e., when the wt.% is zero, is called the enthalpy of adsorption at zero coverage (ΔH_{ads}^0). As shown in Figure 5.10, the absolute value of ΔH_{ads}^0 is 1.78 kJ/mol and 28.5 kJ/mol at 77 K and 300 K, respectively, indicating that the high adsorption sites are available at 300 K. Since the kinetic energy increases at high temperatures, the adsorbent's adsorption capacity reduces. However, the fewer molecules that are adsorbed at high temperatures have a very high ΔH_{ads} .

5.4 Conclusion

In this study, the effect of GBs and Ti concentration on the hydrogen adsorption and desorption capacity of PGs is studied using MD simulations. A uniaxial tensile test of PG systems is also performed to analyze their fracture mechanics. The tensile tests on PGs with 1 nm grains show a maximum reduction in fracture strength by ~38% compared with the pristine graphene sheets, and Ti decoration on PGs shows no significant effect on the net strength. It is also observed that the crack initiation in PGs and Ti-PGs originates from the GBs that are vertical to the direction of the applied load. The H₂ adsorption capacity of PGs increases with the introduction of GBs; for example, the gravimetric density increases by ~57% compared to pristine graphene sheets at 300 K and 50 bar. The maximum adsorption capacity of PGs with 2% Ti decoration reaches 4.4 wt.% and shows no indication of Ti agglomeration at 300 K and 100 bar. It is observed that the desorption of PGs at 300 K follows the adsorption curve, indicating the physisorption of H₂ molecules. The maximum adsorption capacity at 280 K and 300 K is 3.8 wt.% and 3.2 wt.%, respectively, at 100 bar. The adsorption capacity of Ti-PGs is ~4 times higher, and the usable hydrogen released is ~2.5 times higher than the pristine graphene sheet at 300 K. In the case of the lower temperature (77 K), Ti adatoms on PGs agglomerate and a significant reduction in gravimetric density at 2% Ti concentration is observed. The maximum H₂ adsorption capacity of Ti-PGs with 1.5% Ti concentration reaches 10.8 wt.% at 100 bar

and 77 K. The adsorption isotherms of Ti-PGs with 1% Ti concentration at 77 K and 97 K achieve a maximum adsorption capacity of about 9.9 wt.% and 8.8 wt. %, respectively, at 100 bar, and start to saturate at 40–50 bar pressure. Compared to the pristine graphene sheet at 77 K, the adsorption capacity of Ti-PGs with 1 nm grain size and 1% Ti concentration increases by ~46.67%, and the usable hydrogen released at 1 bar is raised by ~55%. The absolute value of ΔH_{ads} decreases with increasing adsorption of H₂, indicating a stronger preference of H₂ for adsorption sites with higher enthalpy. The present chapter provides a theoretical background on the possible use of PGs and Ti-PGs towards hydrogen storage systems at high and low temperatures and pressures up to 100 bar.

Chapter 6

Hydrogen Storage in Graphene: Nitrogen Doping and Titanium Implantation

This study explores the enhancement of hydrogen storage capacity in graphene sheets with vacancy defects (D-G), through nitrogen doping and titanium adatom implantation, using molecular dynamics simulations. This research highlights the potential of structural modifications at the atomic level to optimize graphene's efficacy for hydrogen storage, showcasing the critical role of dopants and adatoms in increasing adsorption capacity and facilitating reversible hydrogen storage.

6.1 Introduction

Graphene is a promising option for the storage application because it has large surface area, excellent thermal stability, high mechanical strength (Kundalwal, 2018; Kundalwal and Ray, 2013), and the ability to readily accept functional groups (Peigney et al., 2001; Ströbel et al., 2006b). In contrast to carbon nanotubes (Kundalwal et al., 2015; Shailesh I. Kundalwal and Ray, 2014), graphene's two surfaces may be actively used to store hydrogen (Ataca et al., 2008), but pristine monolayer graphene has low binding energy, resulting in a low gravimetric density (Ma et al., 2009a). To improve the adsorption capacity, graphene has previously been functionalized with a range of metals, including alkali, platinum, and light transition metals (Chen et al., 2008; Durgun et al., 2006; P. and Ramaprabhu, 2014; Sun et al., 2006). First-principles calculations were performed to explore the efficacy of functionalized carbon-based nanostructures for hydrogen storage (Durgun et al., 2008).

Recent investigations into the enhancement of hydrogen storage capacities in carbon-based materials have yielded promising results through the introduction of metal atoms and nitrogen doping. Corral et al. (López-Corral et al., 2010b) and Sen et al. (Sen et

al., 2013b) demonstrated that palladium atoms on graphene and carbon nanotubes (CNTs) increase the binding energy for hydrogen, especially at the bridge site of carbon bonds, thereby suggesting a potential for higher gravimetric density of hydrogen storage. The addition of nitrogen doping to palladium-implanted graphene sheets was found to significantly enhance the adsorption capacity, with Vinayan et al. (Vinayan et al., 2012) reporting an increase by almost 272% at room temperature and a pressure of 2 MPa. Further experimental work by Xiao et al. (Xiao et al., 2016) and Das et al. (Das et al., 2018) on N-doped porous carbon materials highlighted the importance of a high specific area and the formation of numerous pores with small diameters for maximizing hydrogen storage capacity.

Additionally, the role of metallic and non-metallic atom doping in altering the electronic structure and increasing hydrogen adsorption was explored. Zhang et al. (Zhang et al., 2013) found that doping graphene sheets with metallic atoms, particularly titanium, led to the highest interaction energy among the tested dopants. This finding was supported by Liu et al. (Liu et al., 2010), who emphasized the significance of hybridization between titanium's 3d orbital and molecular hydrogen in enhancing binding energy. Notably, studies on boron-doped graphene and lithium-implanted graphene with DV defects by Nachimuthu et al. (Nachimuthu et al., 2014) and Seenithurai et al. (Seenithurai et al., 2014b) respectively, demonstrated the feasibility of reversible hydrogen storage at ambient temperatures, with lithium adatoms enabling storage up to 7.26 wt.%. Further, Ismail et al. (Ismail et al., 2015) and Wang et al. (Wang et al., 2017) highlighted the effectiveness of palladium and nickel doping on reduced graphene oxide and lithium metal coating on porous graphene sheets for hydrogen storage, achieving high adsorption capacities at low temperatures and ambient pressures. Lastly, Yuan et al. (Yuan et al., 2018) reported that titanium adatoms on porous graphene sheets significantly enhance hydrogen adsorption through polarization and orbital hybridization, offering stability at 300 K without external pressure.

In this chapter, the graphene sheets consisting of vacancy defects (D-G) were doped with N atoms as well as implanted with Ti metal to increase their hydrogen adsorption capacity at room temperature. To the best of our knowledge, no one has performed MD

simulations to explore the effects of dopant and adatom concentration on the hydrogen storage capacity of D-G. Now, we expand our previous efforts and perform MD simulations at the nanoscale, demonstrating the critical role of N doping, Ti adatom concentration, temperature, and pressure in hydrogen adsorption. Graphene sheets with various vacancy defects were modeled and then subjected to N atoms and Ti adatoms to enhance their adsorption capacity. We can better understand the factors that affect hydrogen adsorption capacity using sophisticated MD Simulations.

6.2 Methodology

6.2.1 Modeling of atomic structures

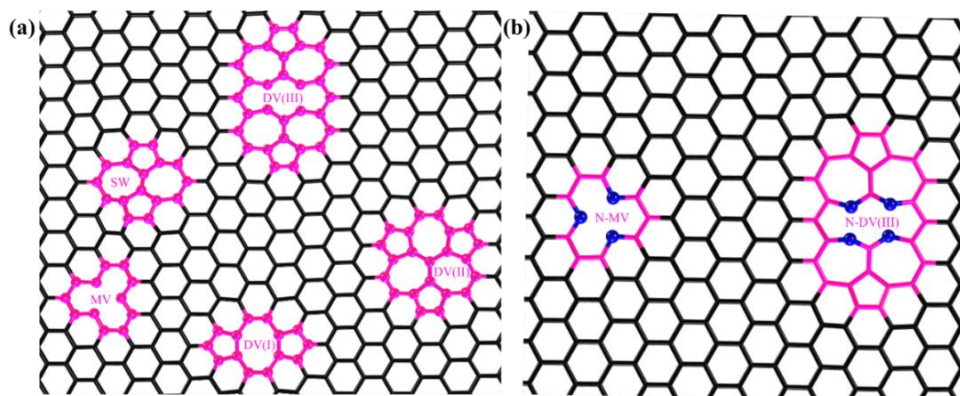


Figure 6.1 (a) Graphene sheet with various types of common defects encountered during synthesis, (b) Graphene sheet containing defects doped with pyridinic nitrogen atoms; black lines are graphene lattice, defects are outlined in magenta, N atoms are in blue

Our simulations consisted of graphene sheets containing multiple defects, for which pristine graphene sheets were initially modeled using the visual molecular dynamics (VMD) (Humphrey et al., 1996b) software tool. Then, using the VESTA (Momma and Izumi, 2008) modeling program, it is possible to insert structural defects into the pristine graphene sheets. Graphene sheets with a variety of defects were modeled, including monovacancy (MV), double vacancy (DV-I, II, III), and Stone–Wales (SW) defects (see Figure 6.1 a). These vacancy defects will present themselves during the synthesis of graphene as a result of temperature and pressure perturbations (Banhart et al., 2011a; Kotakoski et al., 2011; Meyer et al., 2008), and by using these D-G, researchers could enhance the hydrogen adsorption capability and functionalization efficiency of the material. Defects were introduced in the pristine graphene sheet either by removing one or two carbon atoms from the lattice location or by a 90° bond rotation. Different kinds of

vacancy defects have different formation energies and geometries, and the D-G could capture significantly more hydrogen at cryogenic and ambient temperatures. It was possible to model the MV defects when one C atom was removed from the pristine graphene's lattice site. A C-C bond rotated by 90° resulted in the SW defect, containing two heptagon rings and two pentagon rings in the final structure. A DV(I) defect was created when two neighboring monovacancies merged or when two adjacent C atoms were removed simultaneously. When one side of the octagon created in the DV(I) defect rotates by 90° , it results in the formation of the DV(II) defect, and when the other side of the octagon also turns by 90° , it results in the formation of the DV(III) defect. These defects commonly occur at random during the synthesis of graphene (Araujo et al., 2012). The concentration of defects is given by Equation 4.4. In all MD simulations, we considered different types of graphene sheets with a 1% defect concentration, created randomly.

Functionalization of graphene sheets like adding dopants improves their hydrogen adsorption capacities and also helps in uniform dispersion of the metal atoms, avoiding clustering (Ma et al., 2014). Thus, to further enhance the D-G hydrogen adsorption capacity, they were modeled with doping of pyridinic N atoms; all of the possible vacancy sites that can accommodate pyridinic N atoms were doped. The MV-G and DV(III)-G sheets show the most significant results for hydrogen adsorption, so the graphene sheets with these defects were doped at the vacancy sites with pyridinic N atoms (N-D-G), as depicted in Figure 6.1 (b). We also investigated the influence of Ti adatom concentrations on the hydrogen adsorption capabilities of the N-/D-G; they were implanted with varying Ti adatom concentrations. Ti atoms were distributed randomly above and below the N-/D-G in the simulation box, with a concentration varying from ~ 0 -10.5 % by weight. As MD simulations are computationally expensive and time-consuming, the adatom concentration is kept to a maximum of 10.5 wt.% to save computational time.

6.2.2 Interatomic potential

In order to accurately conduct MD simulations of hydrogen adsorption on functionalized graphene sheets, the interatomic interactions of carbon and nitrogen were modeled using the Tersoff potential (Tersoff, 1989b) that was used reliably in the existing studies (Kundalwal et al., 2020b; Luhadiya et al., 2021b). To characterize the interactions

of atoms of N-/D-G and Ti atoms, the Lennard-Jones (LJ) 12-6 potential was utilized (Chu et al., 2011). In this investigation, the diatomic hydrogen molecule was treated as a single entity, and the interatomic interactions between hydrogen molecules (H_2) and Ti-/N-/D-G were also described using the LJ potential. The stated description of the interatomic potential accurately captured the dynamics of adsorption as physisorption mechanisms were only involved between hydrogen and different atomic species. The interaction energy described by the LJ potential is calculated using

$$u_{ij} = 4\varepsilon_{ij} \left[\left(\frac{\sigma_{ij}}{r} \right)^{12} - \left(\frac{\sigma_{ij}}{r} \right)^6 \right], \quad (6.1)$$

where u_{ij} denotes the pairwise interaction energy and ε_{ij} and σ_{ij} denote the well-depth energy and the distance at which the pair interaction energy equals zero, respectively. The interaction parameters for the LJ potential between each atomic entity were reported in previous articles (Chu et al., 2011; Cracknell, 2001; Zhen and Davies, 1983). Lorentz-Berthelot mixing methods were used to calculate the LJ parameters between various species:

$$\varepsilon_{ij} = \sqrt{\varepsilon_i \varepsilon_j} ; \quad \sigma_{ij} = \frac{\sigma_i + \sigma_j}{2}. \quad (6.2)$$

6.2.3 Titanium implantation on N-/D-Gs using MD simulations

Initially, during all MD simulations, the periodic boundary condition was applied to all directions of the simulation box. As illustrated in Figure 6.2, the N-/D-G were placed at the center of the box while keeping the out-of-plane direction large enough to simulate a monolayer graphene sheet. A minimal energy configuration for the simulation box was achieved using the conjugate gradient method, and the system was then equilibrated for 100 ps at atmospheric pressure and the desired temperature using an isothermal-isobaric (NPT) ensemble. Then, on both sides of the sheets, random additions of Ti atoms were carried out (see Figure 6.2 a), the number of atoms added to the system depended on the titanium concentration required to be achieved. The system was heated to a higher temperature of 1000 K, the increase in temperature of the system allows the Ti atoms to migrate more quickly, which results in their bonding to the most active adsorption sites. The system was then gently cooled down to the necessary temperature in 2 ns, and then

equilibrated at the same temperature for 500 ps to obtain an equilibrated and relaxed Ti-N-/D-G at the desired temperatures. The Ti adatoms that did not adhere to the sheet were excluded from the model, and the Ti concentration was again calculated for the relaxed Ti-N-/D-G.

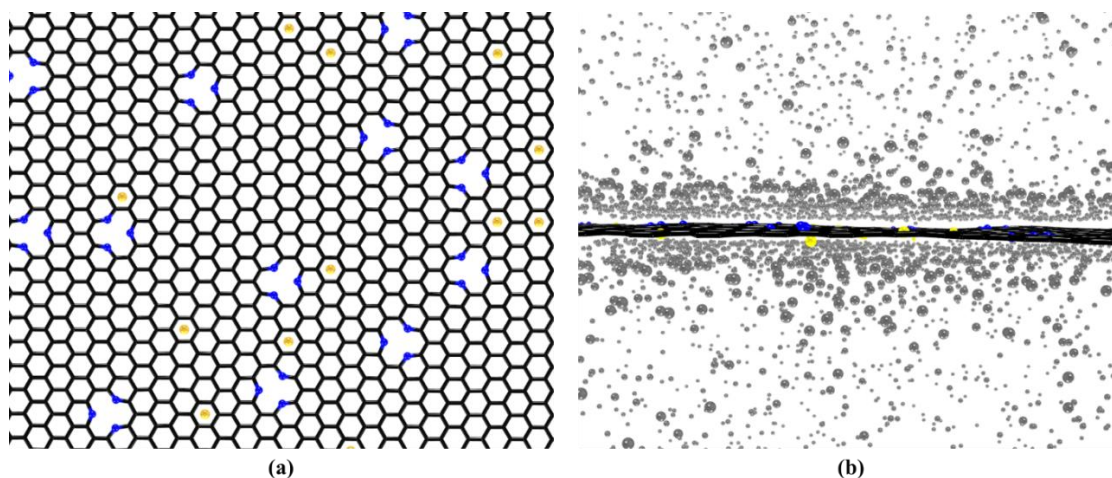


Figure 6.2 (a) Relaxed graphene sheet containing MV defects with titanium adatoms; (b) system configuration with adsorbed hydrogen molecules surrounding Ti-DGs at 1 ns simulation time. The black lines are graphene lattice, N atoms are in blue, Ti atoms are in yellow, and H atoms are in grey.

6.2.4 MD simulation of hydrogen adsorption on functionalized Ti-N-/D-G sheets

In this work, simulations of hydrogen adsorption were carried out using MD at temperatures ranging from 77 to 300 K and pressures ranging from 0 to 100 bar, respectively. A combination of hybrid grand canonical Monte Carlo (GCMC) simulations with the NVT ensemble was used to introduce hydrogen molecules into the system after the Ti-N-/D-G had been completely relaxed. In the GCMC+NVT ensemble, a virtual box containing hydrogen molecules is introduced into the simulation box, which is then set to the appropriate temperature and pressure. Random addition and deletion of hydrogen molecules occur within the simulation box as a result of pressure differences between the virtual box and the simulation box. When the pressure in the simulation box equals the pressure in the virtual reservoir, the insertion and deletion of hydrogen molecules in the simulation box becomes equilibrated with the virtual reservoir. The parameters like temperature, pressure, and interacting potential are known while running the GCMC

simulation. Insertion, deletion, and displacement are the three operations performed during the GCMC run with equal probability randomly.

Following the completion of the GCMC run, the system of hydrogen molecules with Ti-/N-/D-G was re-equilibrated using the thermodynamic ensemble isothermal-isobaric with a total run duration of 2 ns in order to achieve an equilibrated system at the desired temperature and pressure conditions (see Figure 6.2 b). A timestep size of 0.5 fs is used for temporal integration, and temperature and pressure control in all the simulations are performed using the Nosé–Hoover thermostat and barostat.

The adsorption capacity is measured by gravimetric density (wt.%), calculated after completing a simulation at the specified pressure and temperature, using, $wt\% = \frac{w_{H_2adsorbed}}{w_{H_2adsorbed} + w_C + w_N + w_{Ti}}$, where $w_{H_2adsorbed}$ is the weight of the adsorbed hydrogen molecules, w_C is the weight of carbon atoms of the graphene sheet, w_N is the weight of the doped N atoms, and w_{Ti} is the weight of the Ti adatoms. The number of adsorbed hydrogen molecules was calculated by observing the potential energy distribution of all the hydrogen molecules, as discussed in our previous work (Kag et al., 2021; Luhadiya et al., 2021b). A minimum point in the potential energy distribution signifies that hydrogen molecules with a magnitude of potential energy higher than the minimum are adsorbed.

6.3 Results and Discussion

We have conducted extensive research on the combined effect of Ti implantation, N doping, and vacancy defects on the graphene sheet's hydrogen adsorption capacity. According to previous studies (Han et al., 2021; Sunnardianto et al., 2021; Yadav et al., 2014b), graphene sheets with vacancy defects have a better capacity for hydrogen adsorption than pristine sheets, and functionalizing them with other atoms or molecules would further enhance the sheet's capability to adsorb the hydrogen with greater gravimetric density. Due to their distinctive features, we have identified that Ti and N atom functionalization on D-G strengthens the interaction between H₂ molecules and D-G. The pyridinic N atoms were doped near the vacancy sites, and Ti atoms were randomly implanted to ensure that they adhered to the sheet from both sides, preventing their agglomeration and ensuring that the incoming hydrogen adheres to the more active sites,

resulting in an enhanced gravimetric density of hydrogen. Firstly, we reported the effect of Ti implantation on D-G, which helps us identify the sheets with the highest potential to hold the hydrogen at lower and higher temperatures. These sheets were then doped with N atoms, and after that, the effect of Ti adatoms on the N-D-G was reported. In all our simulations, we examined the extent of hydrogen adsorption on N-/D-G with Ti adatoms at lower (77 K) and higher (300 K) temperatures, distinguishing the hydrogen's kinetic behavior towards the adsorbent. The adsorption calculations were performed at 20, 50, and 100 bar pressures with varying Ti adatom concentrations from 0-10.5 wt.% to observe the effect of Ti adatoms at different pressures on the N-D-G hydrogen adsorption capacity.

6.3.1 Effect of Ti adatoms on hydrogen uptake of D-G sheets

As discussed earlier, we ran numerous MD simulations over the Ti-D-G, changing the adatom concentration across the various kinds of vacancy defects. We considered the randomly created various vacancy defects (MV, DV, and SW) and found which type of vacancy defect shows the highest adsorption capacity. For this, we varied the concentration of Ti adatoms while keeping the concentration of defects fixed and calculated the gravimetric density using the potential energy distribution method (Luhadiya et al., 2021b).

The impact of Ti adatoms on the gravimetric density of adsorbed hydrogen on MV-G at various pressures and fixed temperatures is shown in Figure 6.3. The figure implies that at a constant temperature, the hydrogen adsorption capacity of Ti-MV-G rises as the pressure increases. According to Figure 6.3 (a), the maximum hydrogen carrying capacity of Ti-MV-G at 77 K and 10.5% Ti concentration is 9.59, 10.73, and 11.60 wt.% at 20, 50, and 100 bar pressure, respectively. Compared to MV-G, the increase in adsorption capacity due to Ti adatoms at the defined pressures is 12.46%, 19.48%, and 22.75%. Figure 6.3 (b) depicts the variation in the gravimetric density of adsorbed hydrogen on Ti-MV-G at 300K temperature and different pressures.

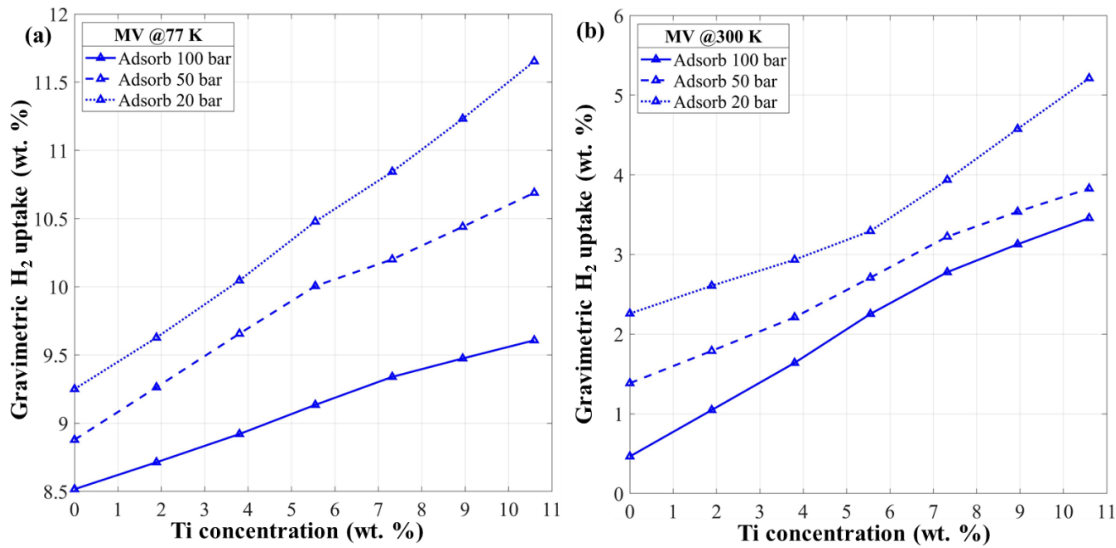


Figure 6.3 Variation in adsorption capacity of Ti-MV-G with increasing Ti concentrations at various pressures and temperatures, (a) 77 K and (b) 300 K.

At 20, 50, and 100 bar pressure, the hydrogen carrying capacity of Ti-MV-G with a 10.5% Ti adatom is 3.45, 3.80, and 5.09 wt.%, which is 7.10, 2.78, and 2.30 times more than that of MV-G, respectively. As the pressure rises, the effect of Ti adatom on adsorption capacity decreases, and it is also noticed that implantation of Ti atoms is more advantageous for hydrogen adsorption at 300 K than at 77 K for the Ti-MV-G. The adsorption at 300 K is enhanced because the MV-G is not saturated at 300 K, even at high pressures, and the addition of Ti atoms saturates them more rapidly as the quantity of adsorbed hydrogen molecules increases. At 77 K, adsorption of Ti atoms on MV-G results in the adsorption of six more H₂/Ti atoms, whereas at 300 K, adsorption of five extra H₂/Ti atoms occurs. Due to their high adsorption energy, MV DGs have the greatest activity towards hydrogen molecules (Pablo A. Denis and Iribarne, 2013; Kag et al., 2021). At 300 K temperature and 100 bar pressure, a 1% Ti adatom raises the gravimetric density by 34.56%, a 2% coating increases it by 79.74%, and a 10.5% coating increases it by 2.30 times. Thus, the inclusion of Ti atoms significantly improves the hydrogen adsorption capability of MV-G

Figure 6.4 represents the variation of the gravimetric density of hydrogen over the Ti-DV(III)-G. This defect consists of four pentagons, one hexagon, and four heptagons and has the highest defect sites among the other possible vacancy defects. Figure 6.4 (a) shows that hydrogen adsorption at a lower temperature of 77 K increases with increasing Ti

concentration and pressure. The maximum gravimetric density of Ti-DV(III)-G with 10.5% Ti concentration at 77 K temperature is 9.75, 10.255, and 10.745 wt.% at 20, 50, and 100 bar pressure, which is 23.04%, 21.96%, and 21.81% more than DV(III)-G, respectively. Figure 6.4 (b) also shows that at higher temperatures, hydrogen adsorption increases with increasing Ti adatom concentration. The maximum wt.% of hydrogen at 300 K temperature is 3.7, 4.23, and 5.38 at 20, 50, and 100 bar pressure, with a maximum Ti adatom concentration of 10.5%. Compared to DV(III)-G, the adsorption capacity increased by 2.42 times, 81%, and 73%, respectively. The adsorption capacity of Ti-DV(III)-G at 300 K temperature and 100 bar pressure is 5.59% higher than that of Ti-MV-G at the same conditions. The higher adsorption capacity is owed to the fact that the DV(III)-G shows higher activity towards the hydrogen molecules as a consequence of higher formation energy (Kag et al., 2021; Yadav et al., 2014b), and the added Ti atoms over the sheet help in achieving a higher gravimetric density and faster saturation. Graphene sheets containing other defects like SW, DV(I), and DV(II), with varying titanium adatom concentrations, adsorb a lesser amount of hydrogen compared to the MV-G and DV(III)-G.

Table 6.1 Comparison of gravimetric density of graphene sheets containing SW, DV(I), DV(II) defects with 10.5% Ti adatom concentration.

Temperature (k)	Gravimetric density (wt.%)					
	77			300		
Pressure (bar)	20	50	100	20	50	100
SW	09.21	09.72	10.01	3.03	3.60	4.63
DV(I)	09.59	10.03	10.43	3.60	3.99	5.16
DV(II)	10.07	10.63	10.98	3.65	4.17	5.30

For brevity, the adsorption capacities of DV(I)-G, DV(II)-G, and SW-G sheets with 10.5% Ti adatom concentration at different temperatures and pressures are shown in Table 6.1. It is observed that the hydrogen adsorption capacity varies as follows: SW < DV(I) < DV(II). The adsorption capacities of these sheets are lower than the Ti-MV-G and Ti-DV(III)-G at 77 K and 300 K, respectively. Compared to all the graphene defect types, Ti-

MV-G and Ti-DV(III)-G show higher adsorption capacities at lower (77 K) and higher (300 K) temperatures, respectively. The MV-G sheets have smaller-sized pores that are high in number, allowing the binding of hydrogen molecules in large amounts but with weak binding; thus, at the higher temperature (300 K), a decrease in adsorbed hydrogen molecules is observed. DV(III)-G sheets, on the other hand, have a small number of larger-sized pores that adsorb fewer hydrogen molecules but with strong binding, demonstrating an increase in adsorption capacity at higher temperatures. Thus, in order to investigate the effect of nitrogen doping in conjunction with titanium adatoms, we performed nitrogen doping on MV-G and DV(III)-G in subsequent adsorption simulations.

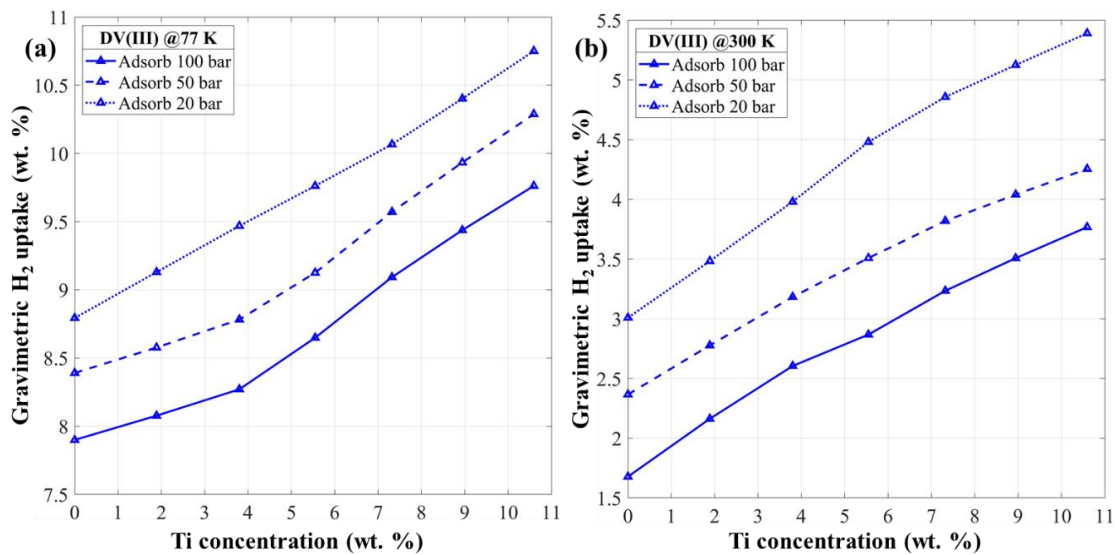


Figure 6.4 Variation in adsorption capacity of Ti-DV(III)-G with increasing Ti concentrations at various pressures and temperatures, (a) 77 K and (b) 300 K.

6.3.2 Effect of Ti adatoms on hydrogen uptake of N-D-G sheets

We also investigated the effect of nitrogen doping on Ti-D-G, where only MV and DV(III) defects were doped with nitrogen, as they showed higher hydrogen adsorption capacities at lower and higher temperatures, respectively. Researchers have found that graphene sheets doped with pyridinic N atoms have a lower formation energy than pyrrolic and graphitic N atoms (Bu et al., 2020; Wang et al., 2012). We doped the D-G sheets with N atoms in such a way that they became pyridinic N atoms; Figure 6.1 (b) shows the structure of D-G sheets with doped pyridinic N atoms. The addition of nitrogen atoms helps in a uniform dispersion of metal adatoms with 2D growth mode and strong binding than

the pristine graphene (Jin et al., 2022). Figure 6.5 and Figure 6.6 show the hydrogen adsorption capacity of the N-MV-G and N-DV(III)-G at 77 and 300 K temperature and 20, 50, and 100 bar pressure with varying Ti concentrations.

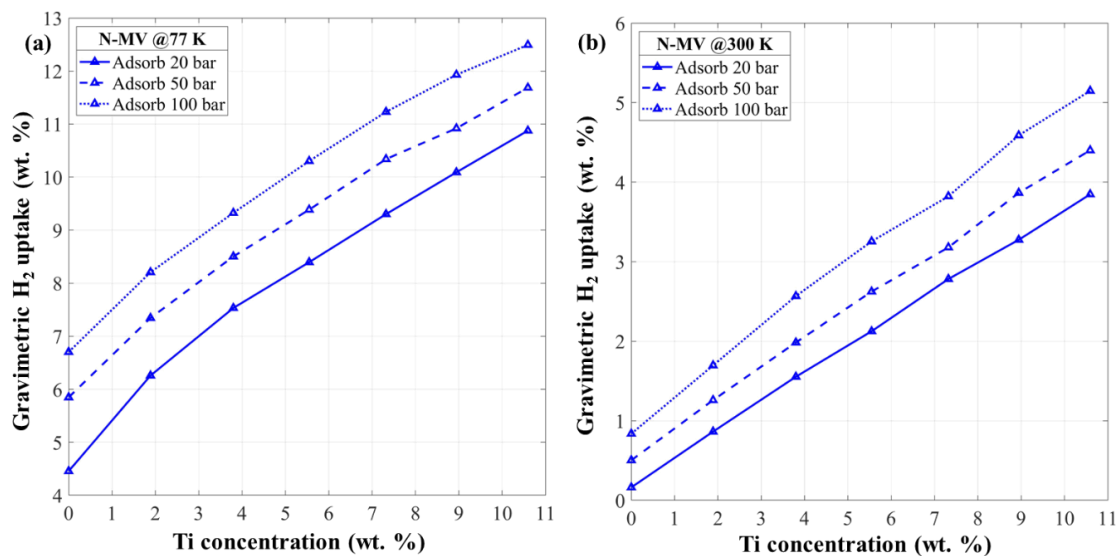


Figure 6.5 Variation in adsorption capacity of Ti-N-MV-G with increasing Ti concentrations at various pressures and temperatures, (a) 77 K and (b) 300 K.

Figure 6.5 (a) and (b) show the hydrogen carrying capacity of the N-MV-G sheets with varying Ti adatom concentrations at 77 and 300 K temperatures, respectively. The maximum hydrogen adsorption capacity of the N-MV-G sheets without Ti adatoms at 100 bar pressure and 77 and 300 K temperatures is 6.71 and 0.84 wt.%, respectively. Figure 6.5 (a) shows that at 77 K temperature and 10.5% Ti adatom concentration, the hydrogen uptake of the N-MV-G sheets at 20, 50, and 100 bar pressure is 10.88, 11.69, and 12.50 wt. %, compared to the MV-G sheets, the adsorption capacity of the N-MV-G sheets increases by 13.41%, 8.91%, and 7.70%, respectively. Figure 6.3 (b) depicts that at 300 K temperature and 10.5% Ti concentration, the hydrogen uptake of N-MV-G sheets is 3.85, 4.34, and 5.15 wt.% at 20, 50, and 100 bar pressure, respectively; which is 11.51%, 15.79%, and 1.14% higher than the MV-G sheets at the same conditions. The N-MV-G compared to Ti-MV-G, at 20 bar pressure, adsorbs hydrogen with a larger difference, and at 100 bar pressure, it adsorbs hydrogen with a negligible difference. Thus, the doping of N atoms into the MV-G sheets saturates the sheets with fast kinetics, as observed from the decreasing rate of hydrogen uptake with increasing pressure.

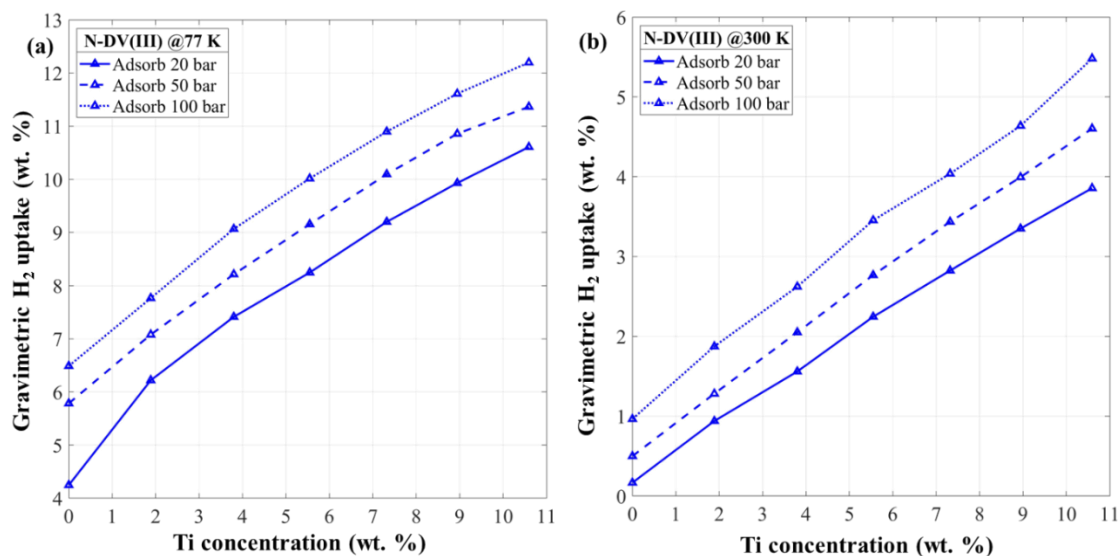


Figure 6.6 Variation in adsorption capacity of Ti-N-DV(III)-G with increasing Ti concentrations at various pressures and temperatures, (a) 77 K and (b) 300 K.

The hydrogen adsorption capacity of N doped DV(III)-G sheets with varying Ti adatom concentration is shown in Figure 6.6 (a) and (b) at 77 and 300 K temperatures, respectively. The maximum hydrogen adsorption capacity of the N-DV(III)-G sheets without Ti adatoms at 100 bar pressure and 77 and 300 K temperatures is 6.48 and 0.96 wt.%, respectively. The hydrogen uptake of the N-DV(III)-G increases with increasing pressure and Ti concentrations. According to Figure 6.6 (a), at 77 K temperature, the hydrogen adsorption capacity of the N-DV(III)-G at 10.5% Ti concentration is 10.61, 11.37, and 12.20 wt.% at 20, 50, and 100 bar pressures, which is higher than the Ti-DV(III)-G sheets by 13.53%, 10.84%, and 8.80%, respectively. Figure 6.6 (b) depicts the hydrogen adsorption capacity of the N-DV(III)-G sheets at 300 K temperature and, at 10.5% Ti concentration, the hydrogen adsorption capacity enhances to 3.86, 4.61, and 5.50 wt.% at 20, 50, and 100 bar pressures; compared to the DV(III)-G sheets, the addition of N atoms enhances the hydrogen adsorption capacity by 4.22%, 8.83%, and 1.87%, respectively. Similar to the N-MV-G sheets, doping of N atoms on DV(III)-G sheets results in fast saturation.

It can be observed from Figure 6.5 and Figure 6.6 that the N doping on the MV- and DV(III)-G sheets enhances the hydrogen adsorption capacity of the sheet. The D-G sheets with no N doping show a very high hydrogen uptake (see Figure 6.3 and Figure 6.4) compared to the N-doped D-G sheets; this implies that the addition of N atoms on the defect

sites reduces the effect of defects on the adsorption capacity. The effect of N doping in MV- and DV(III)-G sheets on the hydrogen uptake is similar, and an insignificant change in adsorption capacity is observed, which is in agreement with our observations. However, it is clearly demonstrated that the reduction due to N doping is subdued with the increasing concentration of Ti adatoms. The N doping on the D-G sheets does not enhance the adsorption capacity, but the addition of Ti adatoms on the N-doped sheet raises the hydrogen uptake more efficiently. Due to the N-doping in the D-G sheets, the dangling carbon atoms at the vacancy sites are not present anymore, and the low hydrogen affinity of doped N atoms results in reduced adsorption activity at the vacancy sites; however, the addition of Ti adatoms shows a rapid improvement in hydrogen uptake because of the high affinity of dangling N atoms towards Ti adatoms. At 10.5% Ti adatom concentration and 100 bar pressure, N-Ti-MV-G adsorbs 12.50 wt.% of hydrogen at 77 K and N-Ti-DV(III)-G sheets adsorb 5.50 wt.% of hydrogen at 300 K; this is the maximum adsorption capacity observed at respective temperatures. Thus, adding N and Ti atoms introduces faster saturation of the sheets and higher adsorption capacity than the graphene sheets containing defects.

In all of the N-/D-G sheets considered, the gravimetric density of hydrogen adsorption increased with the increasing concentrations of Ti adatoms at lower and higher temperatures and considered pressures. The addition of Ti atoms to the N-/D-G sheets shows the improvement in adsorption capacity owed to the Kubas interactions (Kubas, 2001; Skipper et al., 2012), which is a prominent effect in transition metals and hydrogen molecules. In Kubas interaction, the bonds of hydrogen molecules are stretched with no bond breaking; it also involves the σ -donation from the filled σ bonding orbital of the hydrogen molecule to the empty d-orbital of the Ti atom and a simultaneous π -back-donation from the filled Ti d-orbital to the empty σ^* anti-bonding orbital of the hydrogen molecule. Also, hydrogen molecules are physisorbed over graphene sheets due to the Kubas effect, which allows the fast kinetics for adsorption and desorption. The most significant impact of Ti implantation over the graphene sheets with different vacancy defects and N-doping at lower and higher temperatures was found in the Ti-N-MV-G with the highest hydrogen uptake at 77 K and the Ti-N-DV(III)-G having the highest hydrogen uptake at 300 K.

6.4 Conclusions

The current investigation studied the combined effect of Ti adatoms and N doping in graphene sheets containing defects on hydrogen adsorption capacity using MD simulations. The Ti adatoms are randomly decorated to ensure they adhere to the sheet from both sides, and pyrrolic N-doping is performed on the defect sites as they have low formation energy. The addition of Ti adatoms over D-G sheets further enhances the sheet's capability to adsorb hydrogen with greater gravimetric density. Due to the extreme pore number and size, the Ti-MV-G and Ti-DV(III)-G sheets have the highest hydrogen adsorption capacity when compared to all other defect types. However, adding N atoms to the D-G sheets first reduces the effect of defective sites, which reduces hydrogen uptake. Then, as the concentration of Ti adatoms rises in the N-D-G sheets, their adsorption capacities rise quickly, and the value reaches above the Ti-D-G sheets under the same conditions. The N-MV-G and N-DV(III)-G sheets at 10.5 wt.% Ti adatom concentration and 100 bar pressure show the maximum hydrogen uptake of 12.5 and 5.5 wt.% at 77 and 300 K temperatures. The gravimetric density of adsorbed hydrogen on the N-/D-G sheets increases with the increment in Ti adatom concentration and helps achieve a higher gravimetric density and faster saturation. The hydrogen adsorption on Ti-N-/D-G sheets also involves rapid adsorption kinetics as they are physisorbed due to the Kubas interactions. Thus, based on our analysis, N-doped and Ti implanted D-G sheets have special characteristics of reversible hydrogen adsorption and better adsorption capacity than pristine graphene sheets. Decidedly, the work offers detailed accounts of the hydrogen adsorption phenomenon involved in the Ti-/N-/D-G sheets, and we conclude that proper structural change at the atomic level may enhance graphene's potential for hydrogen storage.

Chapter 7

Conclusions and future scope

In this chapter, major conclusions drawn from the current research work are highlighted. Moreover, the scope for further research on GNS and their nanoporous structures with active doping is suggested.

7.5 Major Conclusions

The comprehensive study presented in this thesis provides a detailed analysis of the factors influencing hydrogen storage capabilities in graphene and its modified derivatives through MDS. The findings elucidate the intricate relationship between structural modifications at the atomic and molecular levels and their impact on the adsorption and desorption behaviors of hydrogen on graphene surfaces. The conclusions drawn from the investigation can be summarized as follows:

- MDS combined with potential energy distributions provide a novel and accurate method for analyzing hydrogen adsorption on graphene, marking a first in gravimetric density estimation studies.
- Temperature and pressure significantly influence hydrogen adsorption; lower temperatures and higher pressures improve adsorption efficiency and gravimetric density on graphene sheets.
- Among tested adsorption isotherm models, the Toth isotherm offers the best fit for MDS-generated adsorption isotherms for graphene sheets, outperforming Langmuir, Sips, Fritz-Schlunder, and Freundlich models.
- Maximum adsorption capacities were quantified across various temperatures, showcasing the potential of pristine graphene for physisorption based hydrogen storage, with values peaking at 6.956 wt.% at 77 K and 3.409 wt.% at 300 K.

- Strain increases hydrogen adsorption in GNS, peaking at 6.28 wt.% with a 0.1 strain, a notable increase from the 5.4 wt.% observed in pristine GNS at 77 K and 10 bar.
- Introduction of defects in GNS structures significantly enhances their hydrogen storage capacity compared to the pristine sheets at 77 K and 300 K.
- With vacancy defects like MV at 77 K showing maximum hydrogen adsorption capacity of about 9.30 wt.% at 77 K and GNS with 5555-6-7777 DV defects shows a maximum hydrogen adsorption of 3.09 wt.% at 300 K.
- The presence of defects increases hydrogen adsorption capacity, but adversely affects the material's strength, limiting defect concentration to avoid compromising structural integrity.
- Hydrogen adsorption in GNS reaches saturation at higher pressures, indicating a limit to efficiency gains through pressure increases at specified temperatures.
- Introducing grain boundaries in polycrystalline graphene significantly boosts hydrogen adsorption capacity, showing a ~57% increase at 300 K and 50 bar compared to pristine graphene.
- The adsorption capacity of Ti-decorated PGs significantly outperforms pristine graphene, with a 10.8 wt.% maximum at 77 K and 100 bar for a 1.5% Ti concentration.
- Titanium decoration on PGs enhances hydrogen storage, achieving a maximum of 4.4 wt.% adsorption capacity at 300 K and 100 bar, without affecting the structural strength.
- Ti-PGs demonstrate substantial improvements in hydrogen release, with the usable hydrogen at 300 K being ~2.5 times higher than that of pristine graphene.
- Titanium adatoms and nitrogen doping significantly enhance hydrogen adsorption in graphene sheets with defects, achieving higher gravimetric densities.
- The presence of Ti adatoms markedly boosts hydrogen storage capacities, especially in sheets with mono-vacancies and divacancies, leading to adsorption capacities as high as 12.5 wt.% at 77 K and 100 bar with N doping.
- N doping initially reduces hydrogen uptake due to the alteration of defective sites but subsequently increases capacity with higher Ti concentrations.

- The combination of Ti adatoms and N doping on defective graphene provides rapid adsorption kinetics and reversible hydrogen adsorption, suggesting a potent approach to enhance graphene's hydrogen storage capabilities.

In conclusion, this thesis demonstrates the potential of graphene and its derivatives as promising materials for hydrogen storage, highlighting the pivotal role of structural and compositional modifications. The insights gained from this study contribute to the ongoing efforts in developing efficient, reliable, and scalable hydrogen storage solutions, which are crucial for the advancement of hydrogen as a clean and sustainable energy carrier.

7.6 Limitations of the Study

The following are the limitations of current study:

- We cannot use MD simulations at the subatomic level (electron and proton), since MD approach is only capable of dealing with the atomic/molecular level. In MD simulations, atom is assumed as a particle and therefore, we cannot capture subatomic level phenomena. For example, DFT calculations is the appropriate technique to study the interactions of titanium with graphene and its derivatives and with hydrogen due to complex interaction, but such estimations are performed in the current study reasonably.
- The MD simulations can be performed for the system size with less than 1 million atoms in view of unavailability of computational facility for a small-time scale (shorter than 10 microseconds). If the system size and time scale become larger than 1 million atoms and 10 microseconds, respectively, then either supercomputer is required, or continuum models need to be developed.
- Coulombic interactions, which include long-range electrostatic interactions and van der Waals interactions, play a dominant role in the structural stability of layered nanomaterials in simulations. Typically, the most computationally expensive portion of MD simulations is the evaluation of Coulombic interactions. As the number of charges in a system increases, the number of Coulombic interactions grows as the square of that number, potentially resulting in a prohibitively large number of interactions to evaluate and this needs a huge computational power.

- Graphene containing specific defects and decoration of metals without cluster formation considered in the current study cannot be obtained experimentally exactly in view of some inherent fabrication issues such as reaction, surface effect with substrate/atmosphere, defects, impurities etc. Advance fabrication techniques are becoming matured and there is a possibility of obtaining graphene sheets with different vacancy defects and reduced metal agglomeration.

7.7 Scope for future work

The current fundamental study highlights the possibility of developing high performance, lightweight and multifunctional graphene-based solid state hydrogen storage nanomaterial. The success of this research (i) provided novel method for calculating the number of adsorbed hydrogen molecules using PEDs, (ii) new knowledge in the field of solid-state hydrogen storage that will enable modeling of a storage system, (iii) initiate and serve as a solid foundation for synthesizing and developing a vast range of next-generation nanomaterials for effective hydrogen storage with fast kinetics of adsorption and desorption. Thus, the present research may be followed for further experimental investigation to examine the characteristics of graphene and their nanocomposites. Some of the further research works that may be undertaken in line with the present work as follows:

- MD simulations of graphene oxide sheets with various metal nanoparticle functionalization would provide a more realistic approach. The interatomic potentials to perform these simulations could be developed using advanced machine learning techniques in combination with DFT training data.
- Synthesis of porous graphene structures doped with various nanoparticles, perform characterization for agglomeration and hydrogen storage capabilities.
- Design and propose a new generation safe, lightweight, and highly efficient hydrogen storage prototype for fast kinetics of adsorption and desorption.

References

- A.K.Geim, K.S.Novoselov, Geim, A.K., Novoselov, K.S., 2007. Rise of graphene. *Nature Materials* 6, 183–191. <https://doi.org/10.1038/nmat1849>
- Akiner, T., Mason, J.K., Ertürk, H., 2016. A new interlayer potential for hexagonal boron nitride. *Journal of Physics Condensed Matter* 28. <https://doi.org/10.1088/0953-8984/28/38/385401>
- Albe, K., Möller, W., Heinig, K.H., 1997. Computer simulation and boron nitride. *Radiation Effects and Defects in Solids*. <https://doi.org/10.1080/10420159708211560>
- Alian, A.R., Meguid, S.A., Kundalwal, S.I., 2017a. Unraveling the influence of grain boundaries on the mechanical properties of polycrystalline carbon nanotubes. *Carbon* 125, 180–188. <https://doi.org/10.1016/j.carbon.2017.09.056>
- Alian, A.R., Meguid, S.A., Kundalwal, S.I., 2017b. Unraveling the influence of grain boundaries on the mechanical properties of polycrystalline carbon nanotubes. *Carbon* 125, 180–188. <https://doi.org/10.1016/j.carbon.2017.09.056>
- Alian, A.R., Meguid, S.A., Kundalwal, S.I., 2017c. Unraveling the influence of grain boundaries on the mechanical properties of polycrystalline carbon nanotubes. *Carbon* 125, 180–188. <https://doi.org/10.1016/j.carbon.2017.09.056>
- Allen, M.P., 2004. Introduction to molecular dynamics simulation. *Computational Soft Matter: From Synthetic Polymers to*
- Ansari, R., Ajori, S., Motevalli, B., 2012. Mechanical properties of defective single-layered graphene sheets via molecular dynamics simulation. *Superlattices and Microstructures* 51, 274–289. <https://doi.org/10.1016/j.spmi.2011.11.019>
- Ao, Z., Dou, S., Xu, Z., Jiang, Q., Wang, G., 2014. Hydrogen storage in porous graphene with Al decoration. *International Journal of Hydrogen Energy* 39, 16244–16251. <https://doi.org/10.1016/j.ijhydene.2014.01.044>
- Arachchige, N., 2012. Molecular Dynamics Study of Effects of geometric defects on the mechanical properties of graphene.pdf 82–101.
- Araujo, P.T., Terrones, M., Dresselhaus, M.S., 2012. Defects and impurities in graphene-like materials. *Materials Today* 15, 98–109. [https://doi.org/10.1016/S1369-7021\(12\)70045-7](https://doi.org/10.1016/S1369-7021(12)70045-7)
- Armandi, M., Bonelli, B., Areán, C.O., Garrone, E., 2008. Role of microporosity in hydrogen adsorption on templated nanoporous carbons. *Microporous and Mesoporous Materials* 112, 411–418. <https://doi.org/10.1016/j.micromeso.2007.10.017>
- Ataca, C., Aktürk, E., Ciraci, S., Ustunel, H., 2008. High-capacity hydrogen storage by metallized graphene. *Applied Physics Letters* 93, 043123. <https://doi.org/10.1063/1.2963976>
- Balandin, A.A., Ghosh, S., Bao, W., Calizo, I., Teweldebrhan, D., Miao, F., Lau, C.N., 2008. Superior thermal conductivity of single-layer graphene. *Nano Letters*. <https://doi.org/10.1021/nl0731872>

- Banhart, F., Kotakoski, J., Krasheninnikov, A.V., 2011a. Structural Defects in Graphene. *ACS Nano* 5, 26–41. <https://doi.org/10.1021/nn102598m>
- Banhart, F., Kotakoski, J., Krasheninnikov, A. V., 2011b. Structural defects in graphene. *ACS Nano*. <https://doi.org/10.1021/nn102598m>
- Barghi, S.H., Tsotsis, T.T., Sahimi, M., 2014. Chemisorption, physisorption and hysteresis during hydrogen storage in carbon nanotubes. *International Journal of Hydrogen Energy* 39, 1390–1397. <https://doi.org/10.1016/j.ijhydene.2013.10.163>
- Barrett, S., 2005. Progress in the European hydrogen & fuel cell technology platform. *Fuel Cells Bulletin* 2005, 12–17. [https://doi.org/10.1016/S1464-2859\(05\)00591-2](https://doi.org/10.1016/S1464-2859(05)00591-2)
- Barthélémy, H., 2012. Hydrogen storage - Industrial perspectives. *International Journal of Hydrogen Energy*. <https://doi.org/10.1016/j.ijhydene.2012.04.121>
- Barthelemy, H., Weber, M., Barbier, F., 2017. Hydrogen storage: Recent improvements and industrial perspectives. *International Journal of Hydrogen Energy*. <https://doi.org/10.1016/j.ijhydene.2016.03.178>
- Bastos-Neto, M., Patzschke, C., Lange, M., Möllmer, J., Möller, A., Fichtner, S., Schrage, C., Lässig, D., Lincke, J., Staudt, R., Krautscheid, H., Gläser, R., 2012. Assessment of hydrogen storage by physisorption in porous materials. *Energy and Environmental Science* 5, 8294–8303. <https://doi.org/10.1039/c2ee22037g>
- Bénard, P., Chahine, R., 2001. Modeling of adsorption storage of hydrogen on activated carbons. *International Journal of Non-Linear Mechanics* 36, 849–855.
- Berendsen, H.J.C., Postma, J.P.M., Van Gunsteren, W.F., Dinola, A., Haak, J.R., 1984. Molecular dynamics with coupling to an external bath. *The Journal of Chemical Physics* 81, 3684–3690. <https://doi.org/10.1063/1.448118>
- Berry, G.D., Aceves, S.M., 1998. Onboard storage alternatives for hydrogen vehicles. *Energy and Fuels* 12, 49–55. <https://doi.org/10.1021/ef9700947>
- Bhattacharya, S., Majumder, C., Das, G.P., 2009. Ti-decorated BC₄N sheet: A planar nanostructure for high-capacity hydrogen storage. *Journal of Physical Chemistry C* 113, 15783–15787. <https://doi.org/10.1021/jp905853x>
- Binnig, G., Quate, C.F., Gerber, C., 1986. Atomic force microscope. *Physical Review Letters*. <https://doi.org/10.1103/PhysRevLett.56.930>
- Binnig, G., Rohrer, H., Gerber, C., Weibel, E., 1982. Surface studies by scanning tunneling microscopy. *Physical Review Letters*. <https://doi.org/10.1103/PhysRevLett.49.57>
- Blanco-Rey, M., Juaristi, J.I., Alducin, M., López, M.J., Alonso, J.A., 2016. Is Spillover Relevant for Hydrogen Adsorption and Storage in Porous Carbons Doped with Palladium Nanoparticles? *J. Phys. Chem. C* 120, 17357–17364. <https://doi.org/10.1021/acs.jpcc.6b04006>
- Boateng, E., Chen, A., 2020. Recent advances in nanomaterial-based solid-state hydrogen storage. *Materials Today Advances* 6, 100022. <https://doi.org/10.1016/j.mtadv.2019.100022>
- Borodin, V.A., Vehviläinen, T.T., Ganchenkova, M.G., Nieminen, R.M., 2011. Hydrogen transport on graphene: Competition of mobility and desorption. *Phys. Rev. B* 84, 075486. <https://doi.org/10.1103/PhysRevB.84.075486>

BP Statistical Review of World Energy, 2018. Statistical Review of World Energy June 2018, BP Statistical Review of World Energy.

Braga, S.F., Coluci, V.R., Baughman, R.H., Galvão, D.S., 2007. Hydrogen storage in carbon nanoscrolls: An atomistic molecular dynamics study. *Chemical Physics Letters* 441, 78–82. <https://doi.org/10.1016/j.cplett.2007.04.060>

Bu, H., Chen, Y., Zou, M., Yi, H., Bi, K., Ni, Z., 2009. Atomistic simulations of mechanical properties of graphene nanoribbons. *Physics Letters, Section A: General, Atomic and Solid State Physics* 373, 3359–3362. <https://doi.org/10.1016/j.physleta.2009.07.048>

Bu, S., Yao, N., Hunter, M.A., Searles, D.J., Yuan, Q., 2020. Design of two-dimensional carbon-nitride structures by tuning the nitrogen concentration. *npj Computational Materials* 6, 128. <https://doi.org/10.1038/s41524-020-00393-5>

Castro, E.V., Peres, N.M.R., Santos, J.M.B.L. dos, Guinea, F., Neto, A.H.C., 2008. Bilayer graphene: gap tunability and edge properties. *J. Phys.: Conf. Ser.* 129, 012002. <https://doi.org/10.1088/1742-6596/129/1/012002>

Castro Neto, A.H., Guinea, F., Peres, N.M.R., Novoselov, K.S., Geim, A.K., 2009. The electronic properties of graphene. *Rev. Mod. Phys.* 81, 109–162. <https://doi.org/10.1103/RevModPhys.81.109>

Chae, H.K., Siberio-Pérez, D.Y., Kim, J., Go, Y.B., Eddaoudi, M., Matzger, A.J., O’Keeffe, M., Yaghi, O.M., 2004. A route to high surface area, porosity and inclusion of large molecules in crystals. *Nature* 427, 523–527. <https://doi.org/10.1038/nature02311>

Chahine, R., Bénard, P., 1998. Adsorption Storage of Gaseous Hydrogen at Cryogenic Temperatures, in: *Advances in Cryogenic Engineering*. https://doi.org/10.1007/978-1-4757-9047-4_157

Chambers, A., Park, C., Baker, R.T.K., Rodriguez, N.M., 1998. Hydrogen storage in graphite nanofibers. *Journal of Physical Chemistry B*. <https://doi.org/10.1021/jp9801141>

Chan, K.S., Miller, M.A., Peng, X., 2017. First-principles computational study of hydrogen storage in silicon clathrates. <https://doi.org/10.1080/21663831.2017.1396261>

Chang, E.C., 2017. Robust and optimal technical method with application to hydrogen fuel cell systems. *International Journal of Hydrogen Energy* 42, 25326–25333. <https://doi.org/10.1016/j.ijhydene.2017.08.119>

Chen, M.Q., Quek, S.S., Sha, Z.D., Chiu, C.H., Pei, Q.X., Zhang, Y.W., 2015. Effects of grain size, temperature and strain rate on the mechanical properties of polycrystalline graphene - A molecular dynamics study. *Carbon* 85, 135–146. <https://doi.org/10.1016/j.carbon.2014.12.092>

Chen, Y.L., Liu, B., Wu, J., Huang, Y., Jiang, H., Hwang, K.C., 2008. Mechanics of hydrogen storage in carbon nanotubes. *Journal of the Mechanics and Physics of Solids* 56, 3224–3241. <https://doi.org/10.1016/j.jmps.2008.07.007>

Choi, W., Lahiri, I., Seelaboyina, R., Kang, Y.S., 2010. Synthesis of Graphene and Its Applications: A Review. *Critical Reviews in Solid State and Materials Sciences* 35, 52–71. <https://doi.org/10.1080/10408430903505036>

Chu, S., Hu, L., Hu, X., Yang, M., Deng, J., 2011. Titanium-embedded graphene as high-capacity hydrogen-storage media. *International Journal of Hydrogen Energy* 36, 12324–12328. <https://doi.org/10.1016/j.ijhydene.2011.07.015>

Churchill, S.W., 1997. The reduction of air pollution by improved combustion. *Energy Conversion and Management*. [https://doi.org/10.1016/s0196-8904\(96\)00163-x](https://doi.org/10.1016/s0196-8904(96)00163-x)

Ci, L., Zhu, H., Wei, B., Xu, C., Wu, D., 2002. Annealing amorphous carbon nanotubes for their application in hydrogen storage. *Applied Surface Science* 205, 39–43. [https://doi.org/10.1016/S0169-4332\(02\)00897-8](https://doi.org/10.1016/S0169-4332(02)00897-8)

Ciancia, A., Pede, G., Brighigna, M., Perrone, V., 1996. Compressed hydrogen fuelled vehicles: Reasons of a choice and developments in ENEA. *International Journal of Hydrogen Energy* 21, 397–406. [https://doi.org/10.1016/0360-3199\(95\)00093-3](https://doi.org/10.1016/0360-3199(95)00093-3)

Cohen, M.L., 2001. Nanotubes , Nanoscience , and Nanotechnology 1–11.

Cooper, V.R., Ihm, Y., Morris, J.R., 2012. Hydrogen Adsorption at the Graphene Surface: A vdW-DF Perspective. *Physics Procedia* 34, 34–38. <https://doi.org/10.1016/j.phpro.2012.05.005>

Costanzo, F., Silvestrelli, P.L., Ancilotto, F., 2012. Physisorption, diffusion, and chemisorption pathways of H₂ molecule on graphene and on (2,2) carbon nanotube by first principles calculations. *Journal of Chemical Theory and Computation* 8, 1288–1294. <https://doi.org/10.1021/ct300143a>

Crabtree, G.W., Dresselhaus, M.S., Buchanan, M.V., 2004. The hydrogen economy. *Physics Today* 57, 39–44. <https://doi.org/10.1063/1.1878333>

Cracknell, R.F., 2001. Molecular simulation of hydrogen adsorption in graphitic nanofibres. *Physical Chemistry Chemical Physics* 3, 2091–2097. <https://doi.org/10.1039/b100144m>

Cui, Y., Kundalwal, S.I., Kumar, S., 2016a. Gas barrier performance of graphene / polymer nanocomposites. *Carbon* 98, 313–333. <https://doi.org/10.1016/j.carbon.2015.11.018>

Cui, Y., Kundalwal, S.I., Kumar, S., 2016b. No Title. *Carbon* 98, 313–333.

Dante, R.C., Güereca, L.P., Neri, L., Escamilla, J.L., Aquino, L., Celis, J., 2002. Life cycle analysis of hydrogen fuel: A methodology for a strategic approach of decision making. *International Journal of Hydrogen Energy* 27, 131–133. [https://doi.org/10.1016/S0360-3199\(01\)00098-2](https://doi.org/10.1016/S0360-3199(01)00098-2)

Das, T.K., Banerjee, S., Sharma, P., Sudarsan, V., Sastry, P.U., 2018. Nitrogen doped porous carbon derived from EDTA: Effect of pores on hydrogen storage properties. *International Journal of Hydrogen Energy* 43, 8385–8394. <https://doi.org/10.1016/j.ijhydene.2018.03.081>

De Andres, P.L., Vergés, J.A., 2008. First-principles calculation of the effect of stress on the chemical activity of graphene. *Applied Physics Letters*. <https://doi.org/10.1063/1.3010740>

Deng, S., Sumant, A. V., Berry, V., 2018. Strain engineering in two-dimensional nanomaterials beyond graphene. *Nano Today* 22, 14–35. <https://doi.org/10.1016/j.nantod.2018.07.001>

Denis, Pablo A, Iribarne, F., 2013. A Comparative Study of Defect Reactivity in Graphene A Comparative Study of Defect Reactivity in Graphene. <https://doi.org/10.1021/jp4061945>

Denis, Pablo A., Iribarne, F., 2013. Comparative Study of Defect Reactivity in Graphene. *The Journal of Physical Chemistry C* 117, 19048–19055. <https://doi.org/10.1021/jp4061945>

Deretzis, I., Piccitto, G., La Magna, A., 2012. Electronic transport signatures of common defects in irradiated graphene-based systems, in: *Nuclear Instruments and Methods in Physics Research, Section B: Beam Interactions with Materials and Atoms*. <https://doi.org/10.1016/j.nimb.2011.08.052>

- Dimitrakakis, G.K., Tylianakis, E., Froudakis, G.E., 2008. Pillared graphene: a new 3-D network nanostructure for enhanced hydrogen storage. *Nano Letters* 8, 3166–3170. <https://doi.org/10.1021/nl801417w>
- Durgun, E., Ciraci, S., Yildirim, T., 2008. Functionalization of carbon-based nanostructures with light transition-metal atoms for hydrogen storage. *Physical Review B - Condensed Matter and Materials Physics* 77, 1–9. <https://doi.org/10.1103/PhysRevB.77.085405>
- Durgun, E., Ciraci, S., Zhou, W., Yildirim, T., 2006. Transition-metal-ethylene complexes as high-capacity hydrogen-storage media. *Physical Review Letters* 97, 1–4. <https://doi.org/10.1103/PhysRevLett.97.226102>
- F**aria, B., Guarda, C., Silvestre, N., Lopes, J.N.C., 2020. CNT-reinforced iron and titanium nanocomposites: Strength and deformation mechanisms. *Composites Part B: Engineering* 187, 107836. <https://doi.org/10.1016/j.compositesb.2020.107836>
- Feng, Y., Wang, J., Liu, Y., Zheng, Q., 2019. Adsorption equilibrium of hydrogen adsorption on activated carbon, multi-walled carbon nanotubes and graphene sheets. *Cryogenics* 101, 36–42. <https://doi.org/10.1016/j.cryogenics.2019.05.009>
- Freundlich, H., 1907. Über die Adsorption in Lösungen. *Zeitschrift für Physikalische Chemie* 57U, 385–470. <https://doi.org/10.1515/zpch-1907-5723>
- Fritz, W., Schluender, E.U., 1974. Simultaneous adsorption equilibria of organic solutes in dilute aqueous solutions on activated carbon. *Chemical Engineering Science* 29, 1279–1282. [https://doi.org/10.1016/0009-2509\(74\)80128-4](https://doi.org/10.1016/0009-2509(74)80128-4)
- G**ale, J.D., Geim, A.K., Novoselov, K.S., Castro Neto, A.H., Peres, N.M.R., Novoselov, K.S., Geim, A.K., Tuckerman, M.E., Tomadin, A., Loya, A., Stair, J.L., Ren, G., Geim, A.K., Novoselov, K.S., Geim A. K., Novoselov K. S., Dewapriya, M.A.N., Barker, J. a., Henderson, D., Anderson, T.L., Ariza, M.P., Ortiz, M., Wang, M.C., Yan, C., Ma, L., Hu, N., Chen, M.W., Carpio, A., Bonilla, L.L., De Juan, F., Vozmediano, M.A.H., 2012. The rise of graphene. *Reviews of Modern Physics*. <https://doi.org/10.1016/j.jmps.2010.02.008>
- Gangu, K.K., Maddila, S., Mukkamala, S.B., Jonnalagadda, S.B., 2019. Characteristics of MOF, MWCNT and graphene containing materials for hydrogen storage: A review. *Journal of Energy Chemistry* 30, 132–144. <https://doi.org/10.1016/j.jechem.2018.04.012>
- Georgakis, M., Stavropoulos, G., Sakellaropoulos, G.P., 2014. Alteration of graphene based slit pores and the effect on hydrogen molecular adsorption: A simulation study. *Microporous and Mesoporous Materials* 191, 67–73. <https://doi.org/10.1016/j.micromeso.2014.02.042>
- Goharibajestani, Z., Yürüm, A., Yürüm, Y., 2019. Effect of transition metal oxide nanoparticles on gas adsorption properties of graphene nanocomposites. *Applied Surface Science*. <https://doi.org/10.1016/j.apsusc.2019.01.052>
- Guo, G.F., Huang, H., Xue, F.H., Liu, C.J., Yu, H.T., Quan, X., Dong, X.L., 2013. Electrochemical hydrogen storage of the graphene sheets prepared by DC arc-discharge method. *Surface and Coatings Technology* 228, 120–125. <https://doi.org/10.1016/j.surfcoat.2012.07.016>
- Guo, Y., Seo, D.H., Hong, J., Su, D., Wang, H., Zheng, J., Li, X., Murphy, A.B., Ostrikov, K. (Ken), 2018. Controlling the adsorption behavior of hydrogen at the interface of polycrystalline CVD graphene. *International Journal of Hydrogen Energy* 43, 18735–18744.

Han, D.J., Kim, S., Cho, E.S., 2021. Revealing the role of defects in graphene oxide in the evolution of magnesium nanocrystals and the resulting effects on hydrogen storage. *Journal of Materials Chemistry A* 9, 9875–9881. <https://doi.org/10.1039/D0TA12556C>

Han, J., Sohn, D., Woo, W., Kim, D.K., 2017. Molecular dynamics study of fracture toughness and trans-intergranular transition in bi-crystalline graphene. *Computational Materials Science*. <https://doi.org/10.1016/j.commatsci.2016.12.023>

Heine, T., Zhechkov, L., Seifert, G., 2004. Hydrogen storage by physisorption on nanostructured graphite platelets. *Physical Chemistry Chemical Physics* 6, 980–984. <https://doi.org/10.1039/b316209e>

Hirscher, M., Panella, B., 2005. Nanostructures with high surface area for hydrogen storage. *Journal of Alloys and Compounds* 404–406, 399–401. <https://doi.org/10.1016/j.jallcom.2004.11.109>

Hoang, T.K.A., Antonelli, D.M., 2009. Exploiting the Kubas Interaction in the Design of Hydrogen Storage Materials. *Advanced Materials* 21, 1787–1800. <https://doi.org/10.1002/ADMA.200802832>

Houf, W.G., Evans, G.H., Ekoto, I.W., Merilo, E.G., Groethe, M.A., 2013. Hydrogen fuel-cell forklift vehicle releases in enclosed spaces. *International Journal of Hydrogen Energy* 38, 8179–8189. <https://doi.org/10.1016/j.ijhydene.2012.05.115>

Huang, C.C., Pu, N.W., Wang, C.A., Huang, J.C., Sung, Y., Ger, M.D., 2011. Hydrogen storage in graphene decorated with Pd and Pt nano-particles using an electroless deposition technique. *Separation and Purification Technology* 82, 210–215. <https://doi.org/10.1016/j.seppur.2011.09.020>

Huang, P.Y., Ruiz-Vargas, C.S., Van Der Zande, A.M., Whitney, W.S., Levendorf, M.P., Kevek, J.W., Garg, S., Alden, J.S., Hustedt, C.J., Zhu, Y., Park, J., McEuen, P.L., Muller, D.A., 2011. Grains and grain boundaries in single-layer graphene atomic patchwork quilts. *Nature* 469, 389–392. <https://doi.org/10.1038/nature09718>

Humphrey, W., Dalke, A., Schulten, K., 1996a. VMD: Visual molecular dynamics. *Journal of Molecular Graphics*. [https://doi.org/10.1016/0263-7855\(96\)00018-5](https://doi.org/10.1016/0263-7855(96)00018-5)

Humphrey, W., Dalke, A., Schulten, K., 1996b. VMD: Visual molecular dynamics. *Journal of Molecular Graphics* 14, 33–38. [https://doi.org/10.1016/0263-7855\(96\)00018-5](https://doi.org/10.1016/0263-7855(96)00018-5)

Hussain, T., De Sarkar, A., Ahuja, R., 2012. Strain induced lithium functionalized graphane as a high capacity hydrogen storage material. *Applied Physics Letters* 101. <https://doi.org/10.1063/1.4751249>

Hydrogen Storage | Department of Energy [WWW Document], 2020. URL <https://www.energy.gov/eere/fuelcells/hydrogen-storage> (accessed 1.21.20).

Iñiguez, J., 2008. Modelling of carbon-based materials for hydrogen storage. *Solid-State Hydrogen Storage: Materials and Chemistry* 205–220. <https://doi.org/10.1533/9781845694944.2.205>

Ismail, N., Madian, M., El-Shall, M.S., 2015. Reduced graphene oxide doped with Ni/Pd nanoparticles for hydrogen storage application. *Journal of Industrial and Engineering Chemistry* 30, 328–335. <https://doi.org/10.1016/j.jiec.2015.06.002>

Izadifar, M., Abadi, R., Namazian, A., Rabczuk, T., 2017. Investigation into the effect of doping of boron and nitrogen atoms in the mechanical properties of single-layer polycrystalline graphene. *Computational Materials Science* 138, 435–447. <https://doi.org/10.1016/j.commatsci.2017.06.038>

Izadifar, M., Abadi, R., Nezhad Shirazi, A.H., Alajlan, N., Rabczuk, T., 2018. Nanopores creation in boron and nitrogen doped polycrystalline graphene: A molecular dynamics study. *Physica E: Low-Dimensional Systems and Nanostructures* 99, 24–36. <https://doi.org/10.1016/j.physe.2017.12.036>

Jain, V., Kandasubramanian, B., 2020. Functionalized graphene materials for hydrogen storage. *Journal of Materials Science* 55, 1865–1903. <https://doi.org/10.1007/s10853-019-04150-y>

Javvaji, B., Budarapu, P.R., Sutrarakar, V.K., Mahapatra, D.R., Paggi, M., Zi, G., Rabczuk, T., 2016. Mechanical properties of Graphene: Molecular dynamics simulations correlated to continuum based scaling laws. *Computational Materials Science* 125, 319–327. <https://doi.org/10.1016/j.commatsci.2016.08.016>

Jhi, S.H., 2007. A theoretical study of activated nanostructured materials for hydrogen storage. *Catalysis Today* 120, 383–388. <https://doi.org/10.1016/j.cattod.2006.09.025>

Jin, C., Cheng, L., Feng, G., Ye, R., Lu, Z.-H., Zhang, R., Yu, X., 2022. Adsorption of Transition-Metal Clusters on Graphene and N-Doped Graphene: A DFT Study. *Langmuir* 38, 3694–3710. <https://doi.org/10.1021/acs.langmuir.1c03187>

Jin, H., Lee, Y.S., Hong, I., 2007. Hydrogen adsorption characteristics of activated carbon. *Catalysis Today* 120, 399–406. <https://doi.org/10.1016/j.cattod.2006.09.012>

Jorgensen, S.W., 2011. Hydrogen storage tanks for vehicles: Recent progress and current status. *Current Opinion in Solid State and Materials Science* 15, 39–43. <https://doi.org/10.1016/j.cossms.2010.09.004>

Kag, D., Luhadiya, N., Patil, N.D., Kundalwal, S.I., 2021. Strain and defect engineering of graphene for hydrogen storage via atomistic modelling. *International Journal of Hydrogen Energy*. <https://doi.org/10.1016/j.ijhydene.2021.04.098>

Kan, E., Li, Z., Yang, J., Kan, E., Li, Z., Yang, J., 2011. Graphene Nanoribbons: Geometric, Electronic, and Magnetic Properties, in: *Physics and Applications of Graphene - Theory*. IntechOpen. <https://doi.org/10.5772/14112>

Kim, D., Lee, S., Hwang, Y., Yun, K.H., Chung, Y.C., 2014. Hydrogen storage in Li dispersed graphene with Stone-Wales defects: A first-principles study. *International Journal of Hydrogen Energy* 39, 13189–13194. <https://doi.org/10.1016/j.ijhydene.2014.06.163>

Kim, J., Lee, N., Min, Y.H., Noh, S., Kim, N.-K., Jung, S., Joo, M., Yamada, Y., 2018. Distinguishing Zigzag and Armchair Edges on Graphene Nanoribbons by X-ray Photoelectron and Raman Spectroscopies. *ACS Omega* 3, 17789–17796. <https://doi.org/10.1021/acsomega.8b02744>

KInaI, A., Haskins, J.B., Sevik, C., ÇağIn, T., 2012. Thermal conductivity of BN-C nanostructures. *Physical Review B - Condensed Matter and Materials Physics* 86. <https://doi.org/10.1103/PhysRevB.86.115410>

Klechikov, A.G., Mercier, G., Merino, P., Blanco, S., Merino, C., Talyzin, A. V., 2015. Hydrogen storage in bulk graphene-related materials. *Microporous and Mesoporous Materials* 210, 46–51. <https://doi.org/10.1016/j.micromeso.2015.02.017>

Kotakoski, J., Krasheninnikov, A. V., Kaiser, U., Meyer, J.C., 2011. From point defects in graphene to two-dimensional amorphous carbon. *Physical Review Letters* 106, 105505. <https://doi.org/10.1103/PHYSREVLETT.106.105505/FIGURES/5/MEDIUM>

- Kothari, R., Kundalwal, S.I., Sahu, S.K., 2018. Transversely isotropic thermal properties of carbon nanotubes containing vacancies. *Acta Mechanica*. <https://doi.org/10.1007/s00707-018-2145-z>
- Kubas, G.J., 2001. Metal–dihydrogen and σ -bond coordination: the consummate extension of the Dewar–Chatt–Duncanson model for metal–olefin π bonding. *Journal of Organometallic Chemistry* 635, 37–68. [https://doi.org/10.1016/S0022-328X\(01\)01066-X](https://doi.org/10.1016/S0022-328X(01)01066-X)
- Kumar, A., Sharma, K., Dixit, A.R., 2020. A review on the mechanical properties of polymer composites reinforced by carbon nanotubes and graphene. *Carbon Letters*. <https://doi.org/10.1007/s42823-020-00161-x>
- Kumar, K.V., Salih, A., Lu, L., Müller, E.A., Rodríguez-Reinoso, F., 2012. Molecular Simulation of Hydrogen Physisorption and Chemisorption in Nanoporous Carbon Structures. *Adsorption Science & Technology* 29, 799–817. <https://doi.org/10.1260/0263-6174.29.8.799>
- Kumar, R., Rajasekaran, G., Parashar, A., 2016. Optimised cut-off function for Tersoff-like potentials for a BN nanosheet: A molecular dynamics study. *Nanotechnology*. <https://doi.org/10.1088/0957-4484/27/8/085706>
- Kundalwal, S.I., 2018. Review on micromechanics of nano- and micro-fiber reinforced composites. *Polymer Composites* 39, 4243–4274. <https://doi.org/10.1002/pc.24569>
- Kundalwal, S.I., Choyal, V., 2018a. Transversely isotropic elastic properties of carbon nanotubes containing vacancy defects using MD. *Acta Mechanica* 229, 2571–2584. <https://doi.org/10.1007/s00707-018-2123-5>
- Kundalwal, S.I., Choyal, V., 2018b. Transversely isotropic elastic properties of carbon nanotubes containing vacancy defects using MD. *Acta Mechanica*. <https://doi.org/10.1007/s00707-018-2123-5>
- Kundalwal, S.I., Choyal, V.K., Choyal, V., Nevhal, S.K., Luhadiya, N., 2021. Enhancement of piezoelectric and flexoelectric response of boron nitride sheet superlattices via interface and defect engineering. *Physica E: Low-dimensional Systems and Nanostructures* 127, 114563. <https://doi.org/10.1016/j.physe.2020.114563>
- Kundalwal, S.I., Choyal, V.K., Luhadiya, N., Choyal, V., 2020a. Effect of carbon doping on electromechanical response of boron nitride nanosheets. *Nanotechnology*. <https://doi.org/10.1088/1361-6528/ab9d43>
- Kundalwal, S.I., Choyal, V.K., Luhadiya, N., Choyal, V.K., 2020b. Effect of carbon doping on electromechanical response of boron nitride nanosheets. *Nanotechnology* 31, 405710. <https://doi.org/10.1088/1361-6528/ab9d43>
- Kundalwal, S I, Meguid, S.A., Weng, G.J., 2017. Strain gradient induced polarization in graphene. *Carbon* 1, 1–35. <https://doi.org/10.1016/j.carbon.2017.03.013>
- Kundalwal, S.I., Meguid, S.A., Weng, G.J., 2017. Strain gradient polarization in graphene. *Carbon* 117, 462–472. <https://doi.org/10.1016/j.carbon.2017.03.013>
- Kundalwal, S. I., Ray, M.C., 2014. Shear lag analysis of a novel short fuzzy fiber-reinforced composite. *Acta Mechanica* 225, 2621–2643. <https://doi.org/10.1007/s00707-014-1095-3>
- Kundalwal, Shailesh I., Ray, M.C., 2014. Improved thermoelastic coefficients of a novel short fuzzy fiber-reinforced composite with wavy carbon nanotubes. *Journal of Mechanics of Materials and Structures* 9, 1–25. <https://doi.org/10.2140/jomms.2014.9.1>

- Kundalwal, S.I., Ray, M.C., 2013. Thermoelastic Properties of a Novel Fuzzy Fiber-Reinforced Composite. *Journal of Applied Mechanics* 80, 061011. <https://doi.org/10.1115/1.4023691>
- Kundalwal, S.I., Ray, M.C., Meguid, S.A., 2014. Shear Lag Model for Regularly Staggered Short Fuzzy Fiber Reinforced Composite. *Journal of Applied Mechanics* 81, 091001. <https://doi.org/10.1115/1.4027801>
- Kundalwal, S.I., Suresh Kumar, R., Ray, M.C., 2015. Effective Thermal Conductivities of a Novel Fuzzy Fiber-Reinforced Composite Containing Wavy Carbon Nanotubes. *Journal of Heat Transfer* 137, 012401. <https://doi.org/10.1115/1.4028762>
- Lamari, F.D., Levesque, D., 2011. Hydrogen adsorption on functionalized graphene. *Carbon* 49, 5196–5200. <https://doi.org/10.1016/j.carbon.2011.07.036>
- Langmuir, I., 1918. The adsorption of gases on plane surfaces of glass, mica and platinum. *Journal of the American Chemical Society* 40, 1361–1403. <https://doi.org/10.1021/ja02242a004>
- Lebon, A., Carrete, J., Gallego, L.J., Vega, A., 2015a. Ti-decorated zigzag graphene nanoribbons for hydrogen storage. A van der Waals-corrected density-functional study, in: *International Journal of Hydrogen Energy*. Elsevier Ltd, pp. 4960–4968. <https://doi.org/10.1016/j.ijhydene.2014.12.134>
- Lebon, A., Carrete, J., Gallego, L.J., Vega, A., 2015b. Ti-decorated zigzag graphene nanoribbons for hydrogen storage. A van der Waals-corrected density-functional study. *International Journal of Hydrogen Energy* 40, 4960–4968. <https://doi.org/10.1016/j.ijhydene.2014.12.134>
- Lee, C., Wei, X., Kysar, J.W., Hone, J., 2008a. Measurement of the elastic properties and intrinsic strength of monolayer graphene. *Science* 321, 385–388. <https://doi.org/10.1126/science.1157996>
- Lee, C., Wei, X., Kysar, J.W., Hone, J., 2008b. Measurement of the elastic properties and intrinsic strength of monolayer graphene. *Science* 321, 385–388. <https://doi.org/10.1126/science.1157996>
- Lee, S., Lee, M., Choi, H., Yoo, D.S., Chung, Y.C., 2013. Effect of nitrogen induced defects in Li dispersed graphene on hydrogen storage. *International Journal of Hydrogen Energy* 38, 4611–4617. <https://doi.org/10.1016/j.ijhydene.2013.01.180>
- Léon, A., 2008. Introduction, in: *Hydrogen Technology*. Springer Berlin Heidelberg, pp. 11–13. https://doi.org/10.1007/978-3-540-69925-5_1
- Li, J., Furuta, T., Goto, H., Ohashi, T., Fujiwara, Y., Yip, S., 2003. Theoretical evaluation of hydrogen storage capacity in pure carbon nanostructures. *Journal of Chemical Physics* 119, 2376–2385. <https://doi.org/10.1063/1.1582831>
- Liao, J.H., Zhao, Y.J., Yang, X.B., 2015. Controllable hydrogen adsorption and desorption by strain modulation on Ti decorated defective graphene. *International Journal of Hydrogen Energy* 40, 12063–12071. <https://doi.org/10.1016/j.ijhydene.2015.07.083>
- Liu, F., Ming, P., Li, J., 2007. Ab initio calculation of ideal strength and phonon instability of graphene under tension. *Physical Review B - Condensed Matter and Materials Physics* 76, 1–7. <https://doi.org/10.1103/PhysRevB.76.064120>
- Liu, Y., Ren, L., He, Y., Cheng, H.-P., 2010. Titanium-decorated graphene for high-capacity hydrogen storage studied by density functional simulations. *Journal of Physics: Condensed Matter* 22, 445301. <https://doi.org/10.1088/0953-8984/22/44/445301>

López-Corral, I., Germán, E., Volpe, M.A., Brizuela, G.P., Juan, A., 2010a. Tight-binding study of hydrogen adsorption on palladium decorated graphene and carbon nanotubes. *International Journal of Hydrogen Energy* 35, 2377–2384. <https://doi.org/10.1016/j.ijhydene.2009.12.155>

López-Corral, I., Germán, E., Volpe, M.A., Brizuela, G.P., Juan, A., 2010b. Tight-binding study of hydrogen adsorption on palladium decorated graphene and carbon nanotubes. *International Journal of Hydrogen Energy* 35, 2377–2384. <https://doi.org/10.1016/j.ijhydene.2009.12.155>

Lotfi, E., Neek-Amal, M., Elahi, M., 2015. Molecular dynamics simulation of temperature profile in partially hydrogenated graphene and graphene with grain boundary. *Journal of Molecular Graphics and Modelling*. <https://doi.org/10.1016/j.jmgm.2015.08.007>

Luhadiya, N., Kundalwal, S.I., Sahu, S.K., 2021a. Investigation of hydrogen adsorption behavior of graphene under varied conditions using a novel energy-centered method. *Carbon Letters* 1–12. <https://doi.org/10.1007/s42823-021-00236-3>

Luhadiya, N., Kundalwal, S.I., Sahu, S.K., 2021b. Investigation of hydrogen adsorption behavior of graphene under varied conditions using a novel energy-centered method. *Carbon Letters* 31, 655–666. <https://doi.org/10.1007/s42823-021-00236-3>

Ma, L., Zhang, J.M., Xu, K.W., 2014. Hydrogen storage on nitrogen induced defects in palladium-decorated graphene: A first-principles study. *Applied Surface Science* 292, 921–927. <https://doi.org/10.1016/j.apsusc.2013.12.080>

Ma, L.P., Wu, Z.S., Li, J., Wu, E.D., Ren, W.C., Cheng, H.M., 2009a. Hydrogen adsorption behavior of graphene above critical temperature. *International Journal of Hydrogen Energy* 34, 2329–2332. <https://doi.org/10.1016/j.ijhydene.2008.12.079>

Ma, L.P., Wu, Z.S., Li, J., Wu, E.D., Ren, W.C., Cheng, H.M., 2009b. Hydrogen adsorption behavior of graphene above critical temperature. *International Journal of Hydrogen Energy* 34, 2329–2332. <https://doi.org/10.1016/j.ijhydene.2008.12.079>

Matsunaga, K., Fisher, C., Matsubara, H., 2000. Tersoff potential parameters for simulating cubic boron carbonitrides. *Japanese Journal of Applied Physics, Part 2: Letters* 39.

Mazloomi, K., Gomes, C., 2012. Hydrogen as an energy carrier: Prospects and challenges. *Renewable and Sustainable Energy Reviews* 16, 3024–3033. <https://doi.org/10.1016/j.rser.2012.02.028>

Meyer, J.C., Kisielowski, C., Erni, R., Rossell, M.D., Crommie, M.F., Zettl, A., 2008. Direct Imaging of Lattice Atoms and Topological Defects in Graphene Membranes. *Nano Letters* 8, 3582–3586. <https://doi.org/10.1021/nl801386m>

Mohan, M., Sharma, V.K., Kumar, E.A., Gayathri, V., 2019. Hydrogen storage in carbon materials—A review. *Energy Storage* 1, e35. <https://doi.org/10.1002/est2.35>

Momma, K., Izumi, F., 2011a. VESTA 3 for three-dimensional visualization of crystal, volumetric and morphology data. *Journal of Applied Crystallography* 44, 1272–1276. <https://doi.org/10.1107/S0021889811038970>

Momma, K., Izumi, F., 2011b. VESTA 3 for three-dimensional visualization of crystal, volumetric and morphology data. *Journal of Applied Crystallography*. <https://doi.org/10.1107/S0021889811038970>

Momma, K., Izumi, F., 2008. VESTA : a three-dimensional visualization system for electronic and structural analysis. *Journal of Applied Crystallography* 41, 653–658. <https://doi.org/10.1107/S0021889808012016>

Moradi, R., Groth, K.M., 2019. Hydrogen storage and delivery: Review of the state of the art technologies and risk and reliability analysis. *International Journal of Hydrogen Energy* 44, 12254–12269. <https://doi.org/10.1016/j.ijhydene.2019.03.041>

Mortazavi, B., Cuniberti, G., 2014. Mechanical properties of polycrystalline boron-nitride nanosheets. *RSC Advances* 4, 19137–19143. <https://doi.org/10.1039/c4ra01103a>

Nachimuthu, S., Lai, P.J., Jiang, J.C., 2014. Efficient hydrogen storage in boron doped graphene decorated by transition metals - A first-principles study. *Carbon* 73, 132–140. <https://doi.org/10.1016/j.carbon.2014.02.048>

Nagar, R., Vinayan, B.P., Samantaray, S.S., Ramaprabhu, S., 2017a. Recent advances in hydrogen storage using catalytically and chemically modified graphene nanocomposites. *Journal of Materials Chemistry A* 5, 22897–22912. <https://doi.org/10.1039/c7ta05068b>

Nagar, R., Vinayan, B.P., Samantaray, S.S., Ramaprabhu, S., 2017b. Recent advances in hydrogen storage using catalytically and chemically modified graphene nanocomposites. *Journal of Materials Chemistry A* 5, 22897–22912. <https://doi.org/10.1039/c7ta05068b>

Ng, T.Y., Yeo, J.J., Liu, Z.S., 2012. A molecular dynamics study of the thermal conductivity of graphene nanoribbons containing dispersed Stone-Thrower-Wales defects. *Carbon*. <https://doi.org/10.1016/j.carbon.2012.06.017>

Nilisk, A., Kozlova, J., Alles, H., Aarik, J., Sammelselg, V., 2016. Raman characterization of stacking in multi-layer graphene grown on Ni. *Carbon* 98, 658–665. <https://doi.org/10.1016/j.carbon.2015.11.050>

Novoselov, K.S., Geim, A.K., Morozov, S. V., Jiang, D., Zhang, Y., Dubonos, S. V., Grigorieva, I. V., Firsov, A.A., 2004. Electric field in atomically thin carbon films. *Science*. <https://doi.org/10.1126/science.1102896>

Nuhnen, A., Janiak, C., 2020. A practical guide to calculate the isosteric heat/enthalpy of adsorption via adsorption isotherms in metal–organic frameworks, MOFs. *Dalton Transactions* 49, 10295–10307. <https://doi.org/10.1039/D0DT01784A>

Okamoto, Y., Miyamoto, Y., 2001. Ab initio investigation of physisorption of molecular hydrogen on planar and curved graphenes. *Journal of Physical Chemistry B* 105, 3470–3474. <https://doi.org/10.1021/jp003435h>

P., D., Ramaprabhu, S., 2014. Hydrogen storage in platinum decorated hydrogen exfoliated graphene sheets by spillover mechanism. *Physical Chemistry Chemical Physics* 16, 26725–26729. <https://doi.org/10.1039/C4CP04214J>

Park, H.L., Yi, S.C., Chung, Y.C., 2010a. Hydrogen adsorption on Li metal in boron-substituted graphene: An ab initio approach. *International Journal of Hydrogen Energy* 35, 3583–3587. <https://doi.org/10.1016/j.ijhydene.2010.01.073>

Park, H.L., Yi, S.C., Chung, Y.C., 2010b. Hydrogen adsorption on Li metal in boron-substituted graphene: An ab initio approach. *International Journal of Hydrogen Energy* 35, 3583–3587. <https://doi.org/10.1016/j.ijhydene.2010.01.073>

Patchkovskii, S., Tse, J.S., Yurchenko, S.N., Zhechkov, L., Heine, T., Seifert, G., 2005. Graphene nanostructures as tunable storage media for molecular hydrogen. *Proceedings of the National Academy of Sciences of the United States of America* 102, 10439–10444. <https://doi.org/10.1073/pnas.0501030102>

Peigney, A., Laurent, C., Flahaut, E., Bacsa, R.R., Rousset, A., 2001. Specific surface area of carbon nanotubes and bundles of carbon nanotubes. *Carbon* 39, 507–514. [https://doi.org/10.1016/S0008-6223\(00\)00155-X](https://doi.org/10.1016/S0008-6223(00)00155-X)

Petrushenko, I.K., Petrushenko, K.B., 2018. Hydrogen adsorption on graphene, hexagonal boron nitride, and graphene-like boron nitride-carbon heterostructures: A comparative theoretical study. *International Journal of Hydrogen Energy* 43, 801–808. <https://doi.org/10.1016/j.ijhydene.2017.11.088>

Plimpton, Steve, 1995. Fast parallel algorithms for short-range molecular dynamics. *Journal of Computational Physics* 117, 1–19. <https://doi.org/10.1006/jcph.1995.1039>

Plimpton, S, 1995. Plimpton1995.Pdf. *Journal of Computational Physics* 117, 1–19. <https://doi.org/10.1006/jcph.1995.1039>

Plimpton, S.J., 1995. Computational Limits of Classical Molecular Dynamics Simulations 1 Introduction 2 Parallel MD. LAMMPS, Sandia National Laboratories 1–8.

Porter, J.F., McKay, G., Choy, K.H., 1999. The prediction of sorption from a binary mixture of acidic dyes using single- and mixed-isotherm variants of the ideal adsorbed solute theory. *Chemical Engineering Science* 54, 5863–5885. [https://doi.org/10.1016/S0009-2509\(99\)00178-5](https://doi.org/10.1016/S0009-2509(99)00178-5)

Prabhu, S.A., Kavithayeni, V., Suganthi, R., Geetha, K., 2020. Graphene quantum dots synthesis and energy application: a review. *Carbon Letters*. <https://doi.org/10.1007/s42823-020-00154-w>

Pregler, S.K., Hayakawa, T., Yasumatsu, H., Kondow, T., Sinnott, S.B., 2007. Combined computational and experimental study of Ar beam induced defect formation in graphite. *Nuclear Instruments and Methods in Physics Research, Section B: Beam Interactions with Materials and Atoms*. <https://doi.org/10.1016/j.nimb.2007.05.030>

Pyle, D.S., Gray, E.M.A., Webb, C.J., 2016. Hydrogen storage in carbon nanostructures via spillover. *International Journal of Hydrogen Energy* 41, 19098–19113. <https://doi.org/10.1016/j.ijhydene.2016.08.061>

Rafique, M., Uqaili, M.A., Mirjat, N.H., Tunio, M.A., Shuai, Y., 2019. Ab-initio investigations on titanium (Ti) atom-doped divacancy monolayer h-BN system for hydrogen storage systems. *Physica E: Low-Dimensional Systems and Nanostructures*. <https://doi.org/10.1016/j.physe.2019.01.015>

Rapaport, D.C., 1996. *The Art of Molecular Dynamics Simulation, The Art of Molecular Dynamics Simulation*, by D.~C.~Rapaport, pp.~564.~ISBN 0521825687.~Cambridge, UK: Cambridge University Press, April 2004.

Rivard, E., Trudeau, M., Zaghbi, K., 2019. Hydrogen storage for mobility: A review. *Materials* 12. <https://doi.org/10.3390/ma12121973>

- Roco, M.C., Williams, R.S., 1999. Nanotechnology Research Directions : IWGN Workshop Report Vision for Nanotechnology R & D in the Next Decade, Science And Technology.
- Roh, J.S., Jang, J.K., Kwon, N., Bok, S., Kim, Y.J., Jeon, C., Yoon, H.W., Kim, H.W., Lim, B., Park, H.B., 2021. Macroscopic properties of single-crystalline and polycrystalline graphene on soft substrate for transparent electrode applications. *Carbon* 178, 181–189. <https://doi.org/10.1016/J.CARBON.2021.02.097>
- Rozada, R., Paredes, J.I., López, M.J., Villar-Rodil, S., Cabria, I., Alonso, J.A., Martínez-Alonso, A., Tascón, J.M.D., 2015. From graphene oxide to pristine graphene: revealing the inner workings of the full structural restoration. *Nanoscale* 7, 2374–2390. <https://doi.org/10.1039/C4NR05816J>
- Rusman, N.A.A., Dahari, M., 2016. A review on the current progress of metal hydrides material for solid-state hydrogen storage applications. *International Journal of Hydrogen Energy* 41, 12108–12126. <https://doi.org/10.1016/j.ijhydene.2016.05.244>
- Schlapbach, L., 2009. Hydrogen-fuelled vehicles. *Nature* 460, 809–811. <https://doi.org/10.1038/460809a>
- Schlapbach, L., Züttel, A., 2001. Hydrogen-storage materials for mobile applications. *Nature* 414, 353–358. <https://doi.org/10.1038/35104634>
- Seenithurai, S., Pandyan, R.K., Kumar, S.V., Saranya, C., Mahendran, M., 2014a. Li-decorated double vacancy graphene for hydrogen storage application: A first principles study. *International Journal of Hydrogen Energy* 39, 11016–11026. <https://doi.org/10.1016/j.ijhydene.2014.05.068>
- Seenithurai, S., Pandyan, R.K., Kumar, S.V., Saranya, C., Mahendran, M., 2014b. Li-decorated double vacancy graphene for hydrogen storage application: A first principles study. *International Journal of Hydrogen Energy* 39, 11016–11026. <https://doi.org/10.1016/j.ijhydene.2014.05.068>
- Sen, D., Thapa, R., Chattopadhyay, K.K., 2013a. Small Pd cluster adsorbed double vacancy defect graphene sheet for hydrogen storage: A first-principles study. *International Journal of Hydrogen Energy* 38, 3041–3049. <https://doi.org/10.1016/j.ijhydene.2012.12.113>
- Sen, D., Thapa, R., Chattopadhyay, K.K., 2013b. Small Pd cluster adsorbed double vacancy defect graphene sheet for hydrogen storage: A first-principles study. *International Journal of Hydrogen Energy* 38, 3041–3049. <https://doi.org/10.1016/j.ijhydene.2012.12.113>
- Sharma, V., Kagdada, H.L., Wang, J., Jha, P.K., 2019. Hydrogen adsorption on pristine and platinum decorated graphene quantum dot: A first principle study. *International Journal of Hydrogen Energy*. <https://doi.org/10.1016/j.ijhydene.2019.09.021>
- Shevlin, S.A., Guo, Z.X., 2007. Hydrogen sorption in defective hexagonal BN sheets and BN nanotubes. *Physical Review B - Condensed Matter and Materials Physics* 76. <https://doi.org/10.1103/PhysRevB.76.024104>
- Shiraz, H.G., Tavakoli, O., 2017. Investigation of graphene-based systems for hydrogen storage. *Renewable and Sustainable Energy Reviews* 74, 104–109. <https://doi.org/10.1016/j.rser.2017.02.052>
- Simon, J.-M., Haas, O.-E., Kjelstrup, S., 2010. Adsorption and Desorption of H₂ on Graphite by Molecular Dynamics Simulations. *J. Phys. Chem. C* 114, 10212–10220. <https://doi.org/10.1021/jp1011022>

Sips, R., 1948. On the structure of a catalyst surface. *The Journal of Chemical Physics* 16, 490–495. <https://doi.org/10.1063/1.1746922>

Skipper, C.V.J., Hamaed, A., Antonelli, D.M., Kaltsoyannis, N., 2012. The Kubas interaction in M(ii) (M = Ti, V, Cr) hydrazine-based hydrogen storage materials: a DFT study. *Dalton Transactions* 41, 8515. <https://doi.org/10.1039/c2dt30383c>

Sofo, J.O., Chaudhari, A.S., Barber, G.D., 2007. Graphane: A two-dimensional hydrocarbon. *Physical Review B* 75, 153401. <https://doi.org/10.1103/PhysRevB.75.153401>

Srinivas, G., Zhu, Y., Piner, R., Skipper, N., Ellerby, M., Ruoff, R., 2010. Synthesis of graphene-like nanosheets and their hydrogen adsorption capacity. *Carbon* 48, 630–635. <https://doi.org/10.1016/j.carbon.2009.10.003>

Stalker, M.R., Grant, J., Yong, C.W., Ohene-Yeboah, L.A., Mays, T.J., Parker, S.C., 2019. Molecular simulation of hydrogen storage and transport in cellulose. *Molecular Simulation* 1–10. <https://doi.org/10.1080/08927022.2019.1593975>

Ströbel, R., Garche, J., Moseley, P.T., Jörissen, L., Wolf, G., 2006a. Hydrogen storage by carbon materials. *Journal of Power Sources* 159, 781–801. <https://doi.org/10.1016/j.jpowsour.2006.03.047>

Ströbel, R., Garche, J., Moseley, P.T., Jörissen, L., Wolf, G., 2006b. Hydrogen storage by carbon materials. *Journal of Power Sources* 159, 781–801. <https://doi.org/10.1016/j.jpowsour.2006.03.047>

Stuart, S.J., Tutein, A.B., Harrison, J.A., 2000. A reactive potential for hydrocarbons with intermolecular interactions. *Journal of Chemical Physics*. <https://doi.org/10.1063/1.481208>

Sun, H., 1998. The COMPASS force field: Parameterization and validation for phosphazenes. *Computational and Theoretical Polymer Science*. [https://doi.org/10.1016/S1089-3156\(98\)00042-7](https://doi.org/10.1016/S1089-3156(98)00042-7)

Sun, Q., Jena, P., Wang, Q., Marquez, M., 2006. First-principles study of hydrogen storage on Li₁₂C₆₀. *Journal of the American Chemical Society* 128, 9741–9745. <https://doi.org/10.1021/ja058330c>

Sunnardianto, G.K., Bokas, G., Hussein, A., Walters, C., Moulton, O.A., Dey, P., 2021. Efficient hydrogen storage in defective graphene and its mechanical stability: A combined density functional theory and molecular dynamics simulation study. *International Journal of Hydrogen Energy* 46, 5485–5494. <https://doi.org/10.1016/j.ijhydene.2020.11.068>

Surya, V.J., Iyakutti, K., Mizuseki, H., Kawazoe, Y., 2012. Modification of graphene as active hydrogen storage medium by strain engineering. *Computational Materials Science* 65, 144–148. <https://doi.org/10.1016/j.commatsci.2012.07.016>

Szczeńśniak, B., Choma, J., Jaroniec, M., 2017. Gas adsorption properties of graphene-based materials. *Advances in Colloid and Interface Science* 243, 46–59. <https://doi.org/10.1016/j.cis.2017.03.007>

Tersoff, J., 1989a. Modeling solid-state chemistry: Interatomic potentials for multicomponent systems. *Physical Review B* 39, 5566–5568. <https://doi.org/10.1103/PhysRevB.39.5566>

Tersoff, J., 1989b. Modeling solid-state chemistry: Interatomic potentials for multicomponent systems. *Physical Review B* 39, 5566–5568. <https://doi.org/10.1103/PhysRevB.39.5566>

Tersoff, J., 1988. New empirical approach for the structure and energy of covalent systems. *Physical Review B* 37, 6991–7000. <https://doi.org/10.1103/PhysRevB.37.6991>

Thomas, S., Ajith, K.M., 2014. Molecular Dynamics Simulation of the Thermo-mechanical Properties of Monolayer Graphene Sheet. *Procedia Materials Science* 5, 489–498. <https://doi.org/10.1016/j.mspro.2014.07.292>

Tien, C., 1994. *Adsorption Calculations and Modelling*, Butterworth-Heinemann, Boston. Elsevier, Boston. <https://doi.org/10.1016/c2009-0-26911-x>

Tóth, J., 2000. Calculation of the BET-compatible surface area from any Type I isotherms measured above the critical temperature. *Journal of Colloid and Interface Science* 225, 378–383. <https://doi.org/10.1006/jcis.2000.6723>

Tozzini, V., Pellegrini, V., 2011. Reversible hydrogen storage by controlled buckling of graphene layers. *Journal of Physical Chemistry C* 115, 25523–25528. <https://doi.org/10.1021/jp208262r>

Vinayan, B.P., Sethupathi, K., Ramaprabhu, S., 2012. Hydrogen Storage Studies of Palladium Decorated Nitrogen Doped Graphene Nanoplatelets. *Journal of Nanoscience and Nanotechnology* 12, 6608–6614. <https://doi.org/10.1166/jnn.2012.4539>

Volokh, K.Y., 2012. On the strength of graphene. *Journal of Applied Mechanics, Transactions ASME* 79. <https://doi.org/10.1115/1.4005582>

Wang, F., Zhang, T., Hou, X., Zhang, W., Tang, S., Sun, H., Zhang, J., 2017. Li-decorated porous graphene as a high-performance hydrogen storage material: A first-principles study. *International Journal of Hydrogen Energy* 42, 10099–10108. <https://doi.org/10.1016/j.ijhydene.2017.01.121>

Wang, F.D., Wang, F., Zhang, N.N., Li, Y.H., Tang, S.W., Sun, H., Chang, Y.F., Wang, R.S., 2013. High-capacity hydrogen storage of Na-decorated graphene with boron substitution: First-principles calculations. *Chemical Physics Letters*. <https://doi.org/10.1016/j.cplett.2012.11.015>

Wang, H., Maiyalagan, T., Wang, X., 2012. Review on Recent Progress in Nitrogen-Doped Graphene: Synthesis, Characterization, and Its Potential Applications. *ACS Catalysis* 2, 781–794. <https://doi.org/10.1021/cs200652y>

Wang, Q., Johnson, J.K., 1999. Computer simulations of hydrogen adsorption on graphite nanofibers. *Journal of Physical Chemistry B* 103, 279–281. <https://doi.org/10.1021/jp9839100>

Wang, Y., Liu, J., Wang, K., Chen, T., Tan, X., Li, C.M., 2011. Hydrogen storage in Ni-B nanoalloy-doped 2D graphene. *International Journal of Hydrogen Energy*. <https://doi.org/10.1016/j.ijhydene.2011.07.034>

Wei, Y., Jiang, C., Zhang, Y., Li, X., Zhang, L., Wang, P., Fang, Y., 2021. Investigation of photocatalysis reactions on the single-crystal and polycrystalline graphenes. *Spectrochimica Acta Part A: Molecular and Biomolecular Spectroscopy* 251, 119441. <https://doi.org/10.1016/J.SAA.2021.119441>

Weinberger, B., Lamari, F.D., 2009. High pressure cryo-storage of hydrogen by adsorption at 77 K and up to 50 MPa. *International Journal of Hydrogen Energy* 34, 3058–3064. <https://doi.org/10.1016/j.ijhydene.2009.01.093>

Xiao, P.-W., Guo, D., Zhao, L., Han, B.-H., 2016. Soft templating synthesis of nitrogen-doped porous hydrothermal carbons and their applications in carbon dioxide and hydrogen adsorption. *Microporous and Mesoporous Materials* 220, 129–135. <https://doi.org/10.1016/j.micromeso.2015.08.027>

Xue, K., Xu, Z., 2010. Strain effects on basal-plane hydrogenation of graphene: A first-principles study. *Applied Physics Letters* 96, 33–36. <https://doi.org/10.1063/1.3298552>

Yadav, S., Zhu, Z., Singh, C.V., 2014a. Defect engineering of graphene for effective hydrogen storage. *International Journal of Hydrogen Energy* 39, 4981–4995. <https://doi.org/10.1016/j.ijhydene.2014.01.051>

Yadav, S., Zhu, Z., Singh, C.V., 2014b. Defect engineering of graphene for effective hydrogen storage. *International Journal of Hydrogen Energy* 39, 4981–4995. <https://doi.org/10.1016/j.ijhydene.2014.01.051>

Yang, Z., Huang, Y., Ma, F., Sun, Y., Xu, K., Chu, P.K., 2015. Temperature and strain-rate effects on the deformation behaviors of nano-crystalline graphene sheets. *European Physical Journal B*. <https://doi.org/10.1140/epjb/e2015-50850-x>

Yazyev, O.V., Chen, Y.P., 2014. Polycrystalline graphene and other two-dimensional materials. *Nature Nanotechnology* 9, 755–767. <https://doi.org/10.1038/nnano.2014.166>

Yelgel, C., 2016. Electronic Structure of ABC-stacked Multilayer Graphene and Trigonal Warping: A First Principles Calculation. *J. Phys.: Conf. Ser.* 707, 012022. <https://doi.org/10.1088/1742-6596/707/1/012022>

Yuan, L., Kang, L., Chen, Y., Wang, D., Gong, J., Wang, C., Zhang, M., Wu, X., 2018. Hydrogen storage capacity on Ti-decorated porous graphene: First-principles investigation. *Applied Surface Science* 434, 843–849. <https://doi.org/10.1016/j.apsusc.2017.10.231>

Zhang, H.P., Luo, X.G., Lin, X.Y., Lu, X., Leng, Y., 2013. Density functional theory calculations of hydrogen adsorption on Ti-, Zn-, Zr-, Al-, and N-doped and intrinsic graphene sheets. *International Journal of Hydrogen Energy* 38, 14269–14275. <https://doi.org/10.1016/j.ijhydene.2013.07.098>

Zhang, L., Zhang, S., Wang, P., Liu, C., Huang, S., Tian, H., 2014. The effect of electric field on Ti-decorated graphyne for hydrogen storage. *Computational and Theoretical Chemistry*. <https://doi.org/10.1016/j.comptc.2014.02.032>

Zhen, S., Davies, G.J., 1983. Calculation of the Lennard-Jones n - m potential energy parameters for metals. *Physica Status Solidi (a)* 78, 595–605. <https://doi.org/10.1002/pssa.2210780226>

Zhou, M., Lu, Y., Zhang, C., Feng, Y.P., 2010. Strain effects on hydrogen storage capability of metal-decorated graphene: A first-principles study. *Applied Physics Letters* 97. <https://doi.org/10.1063/1.3486682>

Zhu, Y., Murali, S., Cai, W., Li, X., Suk, J.W., Potts, J.R., Ruoff, R.S., 2010. Graphene and graphene oxide: Synthesis, properties, and applications. *Advanced Materials* 22, 3906–3924. <https://doi.org/10.1002/adma.201001068>

Zyzlila Figueroa-Torres, M., Robau-Sánchez, A., De la Torre-Sáenz, L., Aguilar-Elguézabal, A., 2007. Hydrogen adsorption by nanostructured carbons synthesized by chemical activation. *Microporous and Mesoporous Materials* 98, 89–93. <https://doi.org/10.1016/j.micromeso.2006.08.022>

List of publications and patents

Journal Publications from the Thesis

- *N Luhadiya*, SI Kundalwal, SK Sahu. Investigation of hydrogen adsorption behaviour of graphene under varied conditions using a novel energy-centered method. *Carbon Letters*, 2021, 31, p.655–666.
- D Kag, *N Luhadiya*, SI Kundalwal. Strain and defect engineering of graphene for hydrogen storage via atomistic modelling. *International Journal of Hydrogen Energy*, 2021, 46(43), p.22599-22610.
- *N Luhadiya*, SI Kundalwal, SK Sahu. Adsorption and desorption behavior of titanium-decorated polycrystalline graphene towards hydrogen storage: A molecular dynamics study. *Applied Physics A*, 2022, 128(1), p.1-13.
- *N Luhadiya*, V Choyal, SI Kundalwal, SK Sahu. Investigation of unified impact of Ti adatom and N doping on hydrogen gas adsorption capabilities of defected graphene sheets. *Journal of Molecular Graphics and Modelling*, 2022, 119, p.108399.

Journal Publications apart from the Thesis.

- *N Luhadiya*, SI Kundalwal. Enhancing piezoelectric performance of CNTs through B and N substitution under combined mechanical loads: Insights from MD Simulations. *Nanotechnology*, 2024, *Accepted*.
- S Mishra, *N Luhadiya*, SI Kundalwal. Insights into the adsorption capacity of Li functionalized poly-crystalline carbon nanotubes using molecular dynamics approach. *Carbon*, 2023, 207, p.23-35.
- SI Kundalwal, VK Choyal, *N Luhadiya*, V Choyal. Effect of defects and doping on electromechanical response of boron nitride nanosheets. *Nanotechnology*, 2020, 31(40), p.405710.
- SI Kundalwal, VK Choyal, V Choyal, *N Luhadiya*. Enhancement of piezoelectric and flexoelectric response of boron nitride sheet superlattices via interface engineering. *Physica E: Low-dimensional Systems and Nanostructures*, 2021, 127, p.114563.

Conference proceedings

- VK Choyal, V Choyal, *N Luhadiya*, and SI Kundalwal. Electromechanical properties of carbon-doped Boron nitride nanosheets. International Conference on Precision, Meso, Micro and Nano Engineering, IIT Indore. December 12-14, 2019.

Patents Filed

- SI Kundalwal, *N Luhadiya*, SK Sahu. “A method for estimating the gas adsorption capacity of a solid adsorbent.” Indian Institute of Technology Indore (India, 202221024912), 2022, Indian Patent Office. Applied - 28/04/2022.
- SI Kundalwal, *N Luhadiya*, S Mishra, SK Sahu. “A modular reactor for manometric apparatus operable in a hydrogen environment at high pressures and capable of handling powdered/porous nanomaterials.” Indian Institute of Technology Indore (India, 202221069960), 2022, Indian Patent Office. Applied – 06/12/2022.
- *N Luhadiya*, SI Kundalwal, SK Sahu. “A novel synthesis approach for reduced graphene aerogels doped with titanium nanoparticles.” Indian Institute of Technology Indore, 2022, Indian Patent Office. On priority.

Nitin Luhadiya

(Ph.D. - Research Scientist)

Mechanical Engineering

Indian Institute of Technology (IIT) Indore, India 453552

+91-7000514883, +91-9425477114

nitin.6753@gmail.com, phd1901103004@iiti.ac.in

<https://www.linkedin.com/in/nitin-luhadiya>

Research Area

- Expertise in leveraging computational chemistry tool, classical Molecular Dynamics (MD) simulations to analyze the electromechanical, thermal, and mechanical properties of solid-state materials at the nanoscale.
- Specialization in the experimental synthesis and application of nanomaterials for enhanced hydrogen storage in hydrogen fuel cell (HFC) vehicles.
- Investigation of electromechanical coupling effects within nanomaterials for potential applications in nano-electromechanical systems (NEMS).
- Proficiency in the computational fluid dynamics (CFD) using state-of-the-art simulation techniques.

Academic Record

Passing Year	Examination	Branch / Institute	Board / University	Percentage
Feb 2024 (Expected)	Ph.D. (Fifth year)	Indian Institute of Technology Indore, M.P., India	Indian Institute of Technology Indore	9.08
June 2018	M.E. (Specialization in CAD/CAM/CAE)	Sri Govindram Seksaria Institute of Technology and Science, SGSITS, Indore, M.P., India	RGPV	8.38
June 2014	B.E. (Mechanical Engineering)	Swami Vivekanand College of Engineering, Indore, M.P., India	RGPV	65.56
June 2010	12 th Standard	Columbia Convent School, M.P., Indore	CBSE	74.00
June 2008	10 th Standard	Columbia Convent School, M.P., Indore	CBSE	74.00

Work Experience

- **ITL Industries Ltd.** (July 2015 – June 2016)
Graduate Engineering Trainee
Nature of Job: I lead a cost-optimization initiative targeting the manufacturing expenses associated with our main assembly-line machinery. This was achieved through strategic alterations in technical drawings and refinements in machining processes, ultimately enhancing the cost-efficiency of our production equipment.
- **IIT Indore** (July 2018 – May 2019)
Intern
Nature of Job: During my internship at the Atom Lab at IIT Indore, I engaged in advanced research and assisted in developing a computational model for evaluating piezoelectric effects. Utilizing MATLAB, I created an innovative charge-dipole method that interprets real-time data from LAMMPS, a classical molecular dynamics software. This work not only contributed to the understanding of piezoelectric phenomena but also culminated in the publication of two research articles in distinguished academic journals, reflecting a commitment to scholarly excellence and innovation in the field.
- **IIT Indore** (June 2019-)
Teaching Assistantship
Nature of Job: As a Teaching Assistant at IIT Indore, I facilitated the "Kinematics and Dynamics of Machines Lab" and the "Micro- & Nano-Mechanics of Solids: Fundamentals & Applications Lab." In these roles, I guided and mentored students through the practical applications of complex theoretical concepts, bridging the gap between classroom learning and real-world engineering challenges.

Technical Skills

- Coding Skills : Python, MATLAB
- Nanomaterial modeling and simulations : LAMMPS, Vesta, Nano-engineering, VMD, VASP, MLIP
- Modeling software : AutoCAD, Creo 3.0
- Design analysis : ANSYS, CFD
- Data analysis : MATLAB, Origin, NumPy

Projects undertaken/thesis

- Unraveling the potential of graphene quantum dots for hydrogen storage in fuel cells (Ph.D. Thesis)
- Characterizing the piezoelectric and flexoelectric phenomena in monolayer/layered hexagonal boron nitride nanosheets and development of their nanoelectromechanical systems. (Internship)
- An investigation of flow around a square cylinder with a separate splitter plate at low Reynolds number via Computational fluid dynamics (CFD) techniques. (M.E. Thesis)

Academic Activities

- **Organized:** Six Days' online QIP- STC program on "Micro- & Nano-Mechanics of Solids: Fundamentals & Applications" on 14th December 2020. (Avg. feedback 4.4/5, Participant-61).
- **Organized:** TEQIP course titled "Atomistic Modelling of Solids", Dec 21-25, 2020, at IIT Indore. (Avg. feedback 4.68/5, Participant-65).
- **Coordinator:** Coordinate "International Conference on Precision, Meso, Micro & Nano Engineering" held at IIT Indore from Dec 12-14, 2020. More than 300 national and international participants attended this conference.
- **Received:** Prestigious Prime Minister's Research Fellows (PMRF) scholarship, awarded in recognition of excellent proposal and research contributions in the field of Mechanical Engineering. First person in the department to receive this prestigious scholarship of Rs. 9,60,000 / month.

List of Journal publications

1. *N Luhadiya*, SI Kundalwal, SK Sahu. Investigation of hydrogen adsorption behaviour of graphene under varied conditions using a novel energy-centered method. *Carbon Letters*, 2021, 31, p.655–666.
2. D Kag, *N Luhadiya*, SI Kundalwal. Strain and defect engineering of graphene for hydrogen storage via atomistic modelling. *International Journal of Hydrogen Energy*, 2021, 46(43), p.22599-22610.
3. *N Luhadiya*, SI Kundalwal, SK Sahu. Adsorption and desorption behavior of titanium-decorated polycrystalline graphene towards hydrogen storage: A molecular dynamics study. *Applied Physics A*, 2022, 128(1), p.1-13.
4. *N Luhadiya*, V Choyal, SI Kundalwal, SK Sahu. Investigation of unified impact of Ti adatom and N doping on hydrogen gas adsorption capabilities of defected graphene sheets. *Journal of Molecular Graphics and Modelling*, 2022, 119, p.108399.
5. S Mishra, *N Luhadiya*, SI Kundalwal. Insights into the adsorption capacity of Li functionalized poly-crystalline carbon nanotubes using molecular dynamics approach. *Carbon*, 2023, 207, p.23-35.
6. Kundalwal SI, Choyal VK, *N Luhadiya*, V Choyal. Effect of defects and doping on electromechanical response of boron nitride nanosheets. *Nanotechnology*, 2020, 31(40), p.405710.
7. Kundalwal SI, Choyal VK, Vijay Choyal, *N Luhadiya*. Enhancement of piezoelectric and flexoelectric response of boron nitride sheet superlattices via interface engineering. *2021 Physica E: Low-dimensional Systems and Nanostructures*, 127, p.114563.

List of Conference papers

1. V. K. Choyal, Choyal Vijay, *N Luhadiya* and Kundalwal S. I. Electromechanical properties of carbon-doped Boron nitride nanosheets. International Conference on Precision, Meso, Micro and Nano Engineering (COPEN - 2019), IIT Indore, India, 12-14 Dec 2019.

List of Patents

1. SI Kundalwal, *N Luhadiya*, SK Sahu. "A method for estimating the gas adsorption capacity of a solid adsorbent." Indian Institute of Technology Indore (India, 202221024912), 2022, Indian Patent Office. Applied - 28/04/2022.
2. SI Kundalwal, *N Luhadiya*, Saurabh Mishra, SK Sahu. "A modular reactor for manometric apparatus operable in a hydrogen environment at high pressures and capable of handling powdered/porous nanomaterials." Indian Institute of Technology Indore (India, 202221069960), 2022, Indian Patent Office. Applied – 06/12/2022.
3. *N Luhadiya*, SI Kundalwal, SK Sahu. "A novel synthesis approach for reduced graphene aerogels doped with titanium nanoparticles." Indian Institute of Technology Indore, 2022, Indian Patent Office. On priority.

Extra-Curricular activities

- Participated in the QIP course titled "Micro- and Nano-Micromechanics of Solids" from Dec 14 to 19, 2020.
- Participated in TEQIP III short-term course titled "Atomistic Modeling of Solids: Theory and Application" from Dec 21-25, 2020.
- GATE 2015 Qualified With 50 Marks.

Declaration

I hereby declare that the above particulars are true and correct to the best of my knowledge and belief.

Nitin Luhadiya